Development of an Empirically-Based Numerical Model for the BTMS Design of an EV's Lithium-Ion Battery Pack

Master Thesis by L. Millet

Submitted to the International Center for Numerical Methods in Engineering
(CIMNE), Campus Nord, ETSECCPB
in partial fulfillment of the requirements for the degree of

MSc in Numerical Methods in Engineering
Universitat Politècnica de Catalunya, UPC
Barcelona, Catalunya

developed at

Fraunhofer-Institut für Solare Energiesysteme, ISE
Freiburg im Breisgau, Germany

June 2016

Plagiarism Declaration

I hereby certify that this master thesis was entirely written by me and in my own words, and is not copied from anybodys work. No other sources than those that are mentioned and cited along the work have been used, and the few literally quotations from published or unpublished sources that have been incorporated to the work are clearly indicated and acknowledged as such.

On date: ..... Signed: .....

Abstract

In this thesis, the electrochemical and thermal behavior of an LFP lithium-ion pouch battery is modeled, within a finite elements method framework, in order to study the fast charge procedure that is sought in most of the battery applications and to assess the design process of the BTMS.

The simulation approach couples a 2D empirical electrochemical cell model, based on a simple equivalent circuit model approach, with a 3D thermal model that solves for the thermal activity and temperature distribution among the battery volume.

The electrical performance of the battery under study is characterized experimentally at different ambient temperatures. The open-circuit voltage curve of the battery is approximated from both long relaxation time and continuous low current measurements, and the associated battery impedance is determined from the operating voltage measurements under different continuous current charge and discharge rates.

The thermal performance is experimentally measured by testing the battery within an isothermal calorimeter, and the obtained data is employed to corroborate the validity of the implemented model. The results from the developed electrochemical-thermal model present good agreement with the overall battery thermal measurements data.

The developed model is used, in the second part of the thesis, to study the behavior and the design of the battery thermal management system. On one hand, local battery cooling is analyzed, concluding that local cooling near the battery current tabs can enhance the battery life expectancy. On the other hand, a novel battery pack assembly design for automobile application is presented and modeled, including simple lumped models for heat pipe and thermoelectric elements, and an optimization methodology is set to find the optimal geometry for such design.

Acknowledgments

I feel really lucky for the possibility that I have had to be part of the Electrical Storage Systems (ELS) team during all these months. I have learned from all the team members through the very interesting and frequent discussions about the diverse science that is hidden beyond battery technologies, but also for the joyous and quality time that we have also shared after the workday and during the midday breaks. It has really been a pleasure to work by your side at the Auerstraβe.

More precisely, I want to acknowledge the orientation that I received from Naqqash, Peter, Michael, Julius and Arpit. I am thankful for the interesting discussions with my office mates: Phillip, Mohammad and Ali. I am grateful to Alex and Adrian for their help with the IT problems, and to Lukas, Miguel, Alberto, Katja, and Alexis for their support and because of the good times that we have shared.

I would like to express my gratitude to my supervisor, Max, for always having the necessary patience and time helping me to go across the numerous doubts and problems that arose during the development of the thesis. He has always provided the necessary orientation without ever compromising my own interests, potential and goals.

I am also thankful for all the people that have helped me during this time within the integration to this country, especially to those people who have shown interest in explaining the local culture and traditional peculiarities, and to those who have had the enough patience and dedication to help me learn their language.

Last but not least, I feel indebted to Carolin, who brought me where I am, and who encouraged me during the tough moments.

This work was supported by the Innovation and Networks Executive Agency (INEA), from the European Commission, through the project "Low energy passenger comfort systems based on the joule and peltier effects" (JOSPEL), under H2020-GV-2014 call and with grant agreement no. 653851.

To all, thanks again!

Contents

List of Figures

List of Tables

Nomenclature

Acronyms

ARC	Accelerated rate calorimetry
ASTM	American Society for Testing and Materials
BDF	Backward difference formulation
BEV	Battery electric vehicle
BMS	Battery management system
BTMS	Battery thermal management system
CC	Constant current
CCCV	Constant current constant voltage
COP	Coefficient of Performance
CPE	Constant phase element
CV	Constant voltage
DC	Direct current
DMC	Dymethil carbonate
DOD	Depth of discharge
DOF	Degrees of freedom
EC	Equivalent circuit
EC	Ethylene carbonate
EFC	Equivalent full cycles
EIS	Electrochemical impedance spectroscopy
EOL	Battery end of life
FSD	Full scale deflection
GUI	General User Interface
HEV	Hybrid electric vehicle
IHC	Isothermal heat conduction calorimetry
IR	Infrared thermography
ISO	International Organization for Standardization
LCO	Lithium-cobalt-oxide ($LiCoO_2$)
LFP	Lithium-iron-phosphate, $LiFePO_4$
LMO	Lithium-ion-manganese-oxide ($LiMn_2O_4$ or Li_2MnO_3)

NCA	Lithium-nickel-cobalt-aluminum-oxide ($LiNiCoAlO_2$)	
NMC	Lithium-nickel-mangan-cobalt-oxide ($LiNiMnCoO_2$)	
NMR	Nuclear magnetic resonance	
OCV	Open-circuit voltage	
ODE	Ordinary differential equation	
P2D	Pseudo-two-dimensional models	
PC	Propylene carbonate	
PCM	Phase-change material	
PDE	Partial differential equation	
PID	Proportional-integral-derivative controller	
SEI	Solid electrolyte interface	
SEM	Scanning electron microscope	
SEM	Scanning electron microscopy	
SoA	State-of-the-art	
SOC	State of charge	
SOH	State of health	
SPM	Single particle models	
TED	Thermoelectric device	
USB	Universal serial bus	
XRD	X-ray difraction	

Constants

F	Faraday's constant	96485,3365 $C.mol^{-1}$

Greek Symbols

Δ	Increment	
$\varnothing$	Diameter	mm
η_{bat}	Battery efficiency	
η_{bat}	Energy efficiency of the battery	
κ	Thermal conductivity	$W.m^{-1}.K^{-1}$
Ω	Domain or sub-domain	
ρ	Density	$kg.m^{-3}$
φ	Mapping function	

Latin Symbols

$\dot{q}$	Volumetric heat source	$W.m^{-3}$
$\dot{q}_{bat}$	Volumetric battery heat generation rate	$W.m^{-3}$
$\mathbf{n}$	Normal unit vector	
C_p	Specific heat capacity	$J.kg^{-1}.K^{-1}$
$C_{bat,N}$	Nominal battery capacity	$A.h$

C_{bat}	Battery capacity	$A.h$
$C_{p,bat}$	Lumped specific heat capacity of the battery	$J.kg^{-1}.K^{-1}$
f		
H_{bat}	Enthalpy of the battery	J
h_{bat}	Width of the battery sample	mm
I	Current	A
J	Surface current density	$A.mm^{-2}$
L	Length	mm
m	Weight	kg
m_{bat}	Battery weight	kg
N	Number of cells in a pouch battery	
R	Resistor	Ω
R_{ec}	Battery equivalent-circuit resistivity	$S.mm^{-2}$
T	Temperature	K
t	Time	s
U	Voltage	V
U_{max}	Maximum cut-off voltage	V
U_{min}	Minimum cut-off voltage	V
U_{oc}	Open-circuit voltage	V
V_{bat}	Battery volume	mm^{-3}
Y_{ec}	Battery equivalent-circuit electronic conductivity	$S.mm^{-2}$
Z	Impedance	

Subscripts

bat	Battery
cc	Current collector
eq	Equivalent
exp	Experimental
irrev	Irreversible
n	Negative
oc	Open-circuit
ohm	Ohmic
p	Positive
pouch	Pouch Film
rev	Reversible
s	Separator

Chapter 1

Introduction

According to the International Energy Agency (IEA), "new registrations of electric cars (including both battery electric and plug-in hybrids) increased by 70% between 2014 and 2015, with over 550.000 vehicles being sold worldwide in 2015", and China overtook in 2015 the largest market for pure electric cars from the hands of the United States, with over 200.000 new registrations [1].

The numerous government financial incentives, good examples of which can be found in the Netherlands or Norway, and the increasing availability of charging infrastructure are positively correlated factors to the growth of electric vehicle market shares [2].

Apart from the environmentally friendly position due to their zero greenhouse gas emissions, one of the main advantages of electric cars as compared to internal combustion engine vehicles is their much lower running costs, due to the huge price difference between electricity and oil. On the other side, important barriers to a greater and faster adoption of electric cars over the past recent years include range limitations and vehicle purchase costs, both of which can be mostly attributed to the high cost of the energy storage technologies.

With regard to the first big barrier, according to Energy Storage Updates Energy Storage Cost and Performance Report published in 2015, the technology acknowledgement, R&D, and mass production have led to rapid battery cost declines and performance improvements in the past decade and hold the promise of continuing to progressively reduce the battery technology costs up to 50% in the next five years [3].

Regarding the other main barrier, driving range parity does also not seem that far anymore. Few years ago, the Daihatsu Mira achieved a world record for an electric car running 1003 kilometres without a recharge [4], and on today's market different models can be found with a kilometer range over the 300-400km, including the Chinese manufacturers BYD and Zonda Bus, and Tesla.

Lithium-ion batteries appeared as the technology that has the highest growth among the battery market and that receives most of the industry investments, and their production in MWh has been doubled from 2010 to 2015 [5]. Due to their high energy density (up to $300\mathrm{Wh\,l^{-1}}$ [1]), low self-discharge rate, and good cycle-life, lithium-ion has emerged as the prime candidate as a power source for battery electric vehicles (BEVs) and hybrid electric vehicles (HEVs) for the short and mid term [6, 7].

Currently, most research into lithium-ion technology focus on the material aspect (essentially focused in the cathode material) to improve the energy, power, cost-weight ratio, and life-cycle performance, with relatively less attention paid to thermal issues [8]. However, the thermal issues related to the batteries are one of the main remaining barriers to the acceptation and mass deployment of lithium-ion as the energy storage of vehicles, since safety is a priority and technology uncertainty is a big barrier from the consumer perspective [9].

Recent related battery safety issues include the fire that was caught in a Chevy Volt in 2011, three weeks after a crash testing done by the National Highway Transportation Administration [10], or the BYD taxi accident in 2012, which burned after being hit by a speeding drunk driver [11]. To this list, the recent problems in the Galaxy Note 7, which forced Samsung to recall 2.5 million devices globally, has brought again to light the danger and importance of the thermal issues of the lithium-ion batteries.

For that reason, the number of publications that have appeared in the last decade with regard to this issue have increased greatly, and include the development and investigation of new experimental tools [12, 13] and the derivation of new numerical models for the investigation of battery failure modes [14, 15] and the investigation of new materials with better thermal properties [16]. Analogously, a daunting number of works have recently appeared with regard to new the development of new BTMS design concepts [17, 18, 19, 7, 20, 21, 22, 132, 24, 25, 26, 27].

In relation to this topic, the main objective of the present thesis is to characterize and develop a numerical model to serve as a tool within the design of the battery thermal management system for an electric vehicle. This work is contextualized within a research project from the European Commission, under Horizon2020 call, the purpose of which is to study novel acclimatisation systems for electric vehicles based on the combination of the thermoelectric and Joule effects.

To accomplish with this task, the sample of study is experimentally characterized and a suitable analytical method to study the thermal behavior of the battery is determined and implemented in this work. A finite elements approach is chosen be-

cause of two main reasons. First, because non negligible temperature homogeneities are known to develop in large size pouch batteries [28, 29, 30]; and second, because modelling in a spatially-distributed fashion allows for a more detailed study of the optimal design of the BTMS.

The thesis is organized as follows. In chapter 2, general background related to lithium-ion technology is presented, including basic knowledge and definitions, basic operation principles, and a detailed explanation on the thermal issues of lithium-ion batteries. Chapter 3 gathers a literature review on the state-of-the-art modelling strategies, with particular focus on the thermal aspects.

The conducted battery characterization procedures and results, including electrical and thermal tests, are presented and discussed in Chapter 4. In chapter 5, the details on the implementation of the numerical battery model are presented, while chapter 6 gathers the analysis of the results of such.

In chapter 7, the novel BTMS concept design is presented, after reviewing the most common thermal management systems that are presented in the literature and that can be found in the today's market. Afterwards, the implementation of the presented BTMS design, making use of the previously implemented battery model, is detailed in chapter 8, where some preliminary results are shown and analysed.

Finally, a summary of the present work is written in chapter 9, where the open problems, the suggestions for further research, and the conclusions are also included.

Chapter 2

Background

This chapter is devoted to provide the essential background information to the topic of the present thesis, and aims to facilitate the comprehension of the body of the work even for the reader who is not familiar with battery research and battery technology.

Trying to sort the information in ascending complexity (or concretion), in section 2.1 general battery definitions are presented, and the main battery types and the material components are described.

Section 2.2 focuses on the operation of a battery, including: first, some operational terminology and the standard dis/charging methods introduction; then, the electrochemical physics basics; and finally, the degradation mechanisms.

In the last section, 2.3, a detailed explanation on the main thermal influences and issues on the performance of lithium-ion batteries is included, and can be understood as an extended motivational chapter for the development of the thermal-electrochemical battery models of this thesis.

2.1 Introduction to Lithium-Ion Batteries

2.1.1 General Definitions

Electrochemical Cell and Battery

The characteristic feature of an *electrochemical cell*, also known as galvanic or voltaic cell, is that the energy of the reaction from the chemical process during its operation, that undergoes at least two reaction partners, is available externally as electric current at a defined voltage and time. Depending on the nature of the chemical reaction of the materials of the electrochemical cell, it can be distinguished between: an

irreversible or *primary* cell, which is a nonrechargeable single-use cell; or a reversible or *secondary* cell, which can be recharged several times after discharge [46].

The term *battery* usually refers to a system consistent of an array of a certain number of electrochemical cells, normally assembled in parallel to add up the energy handling capacity of each cell. Assemblies in series are limited because they lead to high and dangerous voltages between battery terminals.

Specific Energy and Specific Power Densities

The *specific energy density* defines the ratio between the battery capacity[1] and the weight (Wh/kg) (gravimetric energy density), or between battery capacity and its volume in liters (Wh/l) (volumetric energy density).

The *specific power density* indicates loading capability, hence it is related to the speed of energy or power delivery capabilities. It is usually expressed as a gravimetric magnitude (W/kg). The maximum power density of a battery is normally specified by the manufacturers with indications on the maximum time duration that this high power supply rate can be maintained without compromising the battery safety and degradation.

Capacity

The *capacity* of a battery is specified as the energy that the battery delivers at a specific discharge rate and temperature within the rated voltage range. It is measured in ampere-hours [A h], in SI units, and must not be confused with the capacitance, in Farads [F], of a capacitor.

The theoretical capacity of a cell can be calculated by Gibb's free energy relation as $C_{bat} = x(nF)$, where x is the number of moles of reaction associated with the complete discharge of the cell, n is the number of moles of electrons exchanged, and F is the Faradays constant. Note, thus, that the more the electrode material that a cell or battery contains, the greater its capacity is.

However, a direct characterisation of the cell capacity via direct measurement of the amount of active materials is hard to realize, since some of the active materials might be, in practice, unusable. Possible reasons might be degradation, electrical disconnection, or an excess of active materials. In fact, excess of active materials is usually sought by the manufacturers because of practical reasons. In addition, the cell fully discharged and fully charged states are usually defined based on the

[1] See the following definition of *Capacity*.

specified cut-off voltages, as explained above, which might differ from one application to another.

The charge and discharge capacities are usually slightly different, and most of the times depend on the discharging or charging rates and on the ambient conditions, because of their influence on electrode kinetics phenomena. In general, the higher the current rates the lower the capacity a battery is capable of handling or delivering and, similarly, the capacity decreases with decreasing temperatures.

2.1.2 Types of Batteries

Batteries come in many shapes and sizes. Mainly, three different kinds of physical battery arrangements or packaging styles exist in the market for power applications (see Figure 2.1). The difference relies on how the electrochemical cell structures are grouped and packed: there are cylindrical cells, prismatic cells, or pouch cells.

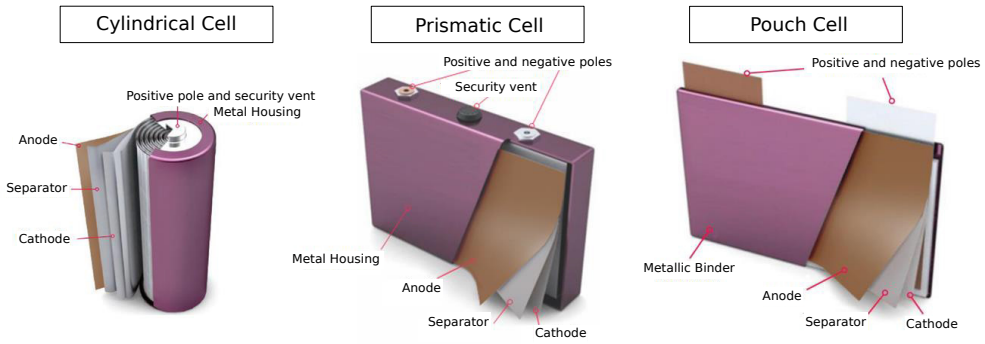

Figure 2.1: *Plot of the three main types of power batteries in the market. Image adapted from [55].*

Cylindrical cells are still very popular and have the advantages of a very good mechanical stability and ease of manufacture. Prismatic cells and pouch cells make a more optimized use of the space, by using a flat layered structure, and they are normally preferred for larger energy cells. The pouch is the lightest and the most efficient packaging style, because it gets rid of the metallic enclosure that is needed in the other packaging styles, and carries other advantages like the possibility of using a more effective thermal dissipation. On the other side, the main disadvantage is the swelling that this cells experience during cycling, which has to be taken into account when designing pouch battery packs.

2.1.3 Electrochemical Cell Components

An electrochemical or galvanic cell consist of an alternation of layers, including the active materials (such as the cathode, the anode, and the electrolyte), the separator, and the current collectors.

In this section, each of the cell materials are described: their main functions are outlined and the most common materials on today's technologies are presented.

Cathode

The *cathode*, or positive electrode, is the active material that accepts electrons from the external circuit during discharge processes, hence getting reduced.

It consists typically of a lithium transition metal compound, in whose crystalline structure lithium ions can be inserted. Mainly, three classes of cathode materials for lithium-ion cells exist in the market, which are classified according to their molecular structure: layered oxides, such as the well-known LCO, NCA, or NMC chemistries ($LiCoO_2$, $LiNiCoAlO_2$ and $LiNiMnCoO_2$, respectively); spinels, LMO being the main representative of this kind ($LiMn_2O_4$); and polyanions, such as the so-called LFP ($LiFePO_4$), which belongs to the family of the olivines or phosphates.

Anode

The *anode*, or negative electrode, is the active material that gives electrons to the external circuit and gets oxidized during the electrochemical reaction in discharge processes.

Metallic lithium was used in the beginning as an anode material because of its high specific charge density and its very low galvanic electrochemical potential. However, this material proved to be harmfully dangerous, due to its high reactivity with air and water and the common apparition of internal short-circuits. The modern lithium-ion batteries use insertion materials for the anode. Thereby, the lithium never exists as a metal inside the cell, but only in ionized form, while dissolved in the electrolyte or bound within the electrodes insertion materials.

Graphite is a popular material for state-of-the-art anodes, thanks to the good electrical conductivity and high specific charge density. Other appropriate properties are its good mechanical surface stability, and good lithium insertion properties with relatively low volume increase, which results in consistent safety properties throughout the battery lifetime. Other materials, such as soft carbon, siliceous alloys, or lithium titanate ($Li_4Ti_5O_{12}$) are under development for future anode materials [5].

Electrolyte

The *electrolyte*, or ionic conductor, acts at the same time as an electric isolating substance between the active materials and as a transporting media for the lithium ions traveling from anode to cathode, during discharge, or viceversa during charge.

The electrolyte is typically a liquid solution of lithium salts, such as Lithium hexafluorophosphate ($LiPF_6$), in an aprotic organic solvent [128], like propylene carbonate (PC), dymethil carbonate (DMC), or ethylene carbonate (EC).

The electrolyte components are usually not totally stable against the cell potential at the anode. For that reason, the electrolyte solvents tend to get reduced near the anode forming a thin Nernst layer, or diffusion layer: the so-called solid electrolyte interface (SEI). A controlled SEI layer of reduced electrolyte molecules is a necessary component in lithium-ion cells. It electrically isolates the anode due to its lower ionic conductivity, as compared to one of the electrolyte bulk solution, and prevents the liquid electrolyte to get further reduced with the anode [47].

In the electrolyte composition design, it is sought, by use of some additives, that the SEI is formed in a controlled and stable way: the ideal SEI would be formed during the first cycles, stay completely stable afterwards, and be totally non-conductive for electrons [34]. However, and as it will be covered more in detail in section 2.3, the real SEI properties are not perfect. In fact, electrolyte reduction near the anode cannot be avoided at all, which translates into a steady growth of the SEI during the battery life. The attributed and well-known consequences in the batteries are: first, the battery or cell capacity fades due to the consumption of active materials in the SEI growth and, second, the power capabilities fade due to the increase of the overall ionic resistivity.

Other Components

The *separator*, a thin layer of electrically isolating material but, at the same time, permeable to the transport of ions. The separator is needed to avoid direct flow of electrons between the electrodes, which would represent an internal short circuit.

The *current collectors*, in contact with the electrodes, gather and conduct the electrochemical generated electrical currents to the external circuit via the so-called *current terminals* or *current tabs*. Normally, the positive current collector is made of aluminum, whereas copper is employed for the negative current collector.

2.2 Operation of a Cell

2.2.1 Terminology

Open-Circuit Voltage

Under equilibrium conditions, and under no current flow, the potential difference of the terminals of a lithium-ion cell corresponds to the so-called open-circuit voltage (OCV). This equilibrium potential is also called metal-ion potential, since it exists due to the coexistence in balanced phases of a metal and its ions. It can either be measured or calculated as the difference between the oxidation potential of the anode and the reduction potential of the cathode, which are determined by the material they are made of, being the potential of half-cell determined by the Nernst equation[2].

C-rate

The name *C-rate* stands for a current rate which is adopted for determining the current in the field of batteries by most of the studies. This terminology is employed hence as a current rate unit, rather than expressing the current amplitudes in amperes, [A], in order to increase the comparability of different size or different capacity batteries. The C-rate is defined as the current to discharge the nominal capacity (see the definition below) in one hour. Thus, a C-rate of $\aleph$ implies that the nominal capacity of the cell, in Ah, is delivered in $(1/\aleph)$ hours, e.g. for a 2Ah cell, discharge at C/5-rate signifies a current of 0,4A, while 2C translates into 4A current rate.

Cut-off Voltages

The terminal voltages of a battery must be maintained at any time between the minimum and the maximum *cut-off voltages*, U_{min} and U_{max}, which are specified by the manufacturer.

The minimum cut-off voltage is the voltage at which a battery is considered fully discharged, beyond which further discharge could cause harm or irreversible degradation of the battery. The maximum cut-off voltage is the maximum electric potential at which the cell must be charged in order to avoid safety hazards. Thus, this voltage usually determines the fully charged state of a battery.

[2]In electrochemistry, the Nernst equation relates the reduction potential of an electrochemical reaction to the standard electrode potential, temperature, and activities or concentrations by: $U_{cell} = U^0_{cell} - \frac{RT}{zF} \ln \frac{[red]}{[ox]}$

In most of the applications, the batteries are not used at its low-end voltage spectrum. Hence, the power of the battery is cut at a higher voltage than the value of the minimum operating voltage, U_{min}. In this case, the specified power shut down voltage level is also denominated cut-off voltage.

State of Charge

The *state of charge* (SOC) is the equivalent to a fuel gauge for a battery or a battery pack. It is defined as

$$SOC(t) = SOC(t_0) - \frac{1}{C}\int_{t_0}^{t} I(\tau)d\tau \tag{2.1}$$

where C_{bat} is the capacity of the battery, and is an indicator of the current state of a battery and the remaining available energy or capacity. Usually expressed as a per one (0-1) or percent(0-100%) magnitude. The SOC takes value 1, or 100%, in a fully-charged state, and is 0, or 0%, when the battery is empty, or fully discharged.

The simplest methodology to determine the state of charge of a battery integrates the direct measurements of the charge that is flowing inside and/or outside the battery and assumes a constant battery capacity (Coloumb-counting). More complex methodologies, complement the direct current measurements with a set of indirect methods, such as, i.e., Kalman filtering, with the objective of accounting for the variations of the capacity of the battery (that depend highly and variably on the operating conditions).

Depth of Discharge

The *depth of discharge* (DOD) is an alternative indicator of the battery's state of charge (SOC). It is defined as the complement of the SOC indicator: takes value 1, or 100%, when the battery is fully discharged, and 0, or 0%, when the battery is full.

$$DOD(t) = 1 - SOC(t) \tag{2.2}$$

2.2.2 Battery Dis/Charging Procedures

The standard battery dis/charging methods include basically two different processes:

1. Galvanic or constant current (CC) dis/charge process, which is characterized by a constant (input or output) current rate. From an external circuit, the current which is supplied or extracted from the battery is maintained.

2. Constant-voltage (CV) process, that corresponds to those in which the input or output current is controlled in such a way that the battery terminal voltage is maintained at a constant level. Normally, the magnitude of the external current in CV phases decreases in an exponential fashion, due to the battery relaxation kinematics.

Fast charging procedures make use of a high current CC charge, which is followed by a CV charge when the upper cut-off voltage, U_{max}, is reached. Commonly, the CV charge at U_{max} is maintained until the current has decreased below some fixed limits, i.e., below C/10 or C/20 current rates.

Since this procedure is quite standard, it is normally called CCCV procedure. Analogously, the same terminologies (CC, CV, CCCV) are used for discharge processes among the battery community and the literature.

Charge and Discharge Curves

Charge and discharge curves show the voltage of a battery or cell during a deep charge or discharge, measured in the current tabs, usually under a galvanic regime (or constant current rate, CC). The current-voltage charge and discharge curves are one of the most important characteristics of batteries. Plots of cell voltage against the current are usually referred to as *polarization curves*, whereas graphs of cell voltage as a function of the capacity (or of the fraction of the completed dis/charge) are known as *discharge curves*.

2.2.3 Electrochemical Principles

Dis/Charge Processes

The decrease of Gibb's free energy[3] is the driving force of the oxidation-reduction (redox) reactions occurring during discharge in an electrochemical cell, whereas the charging process implies an increase of the free energy, which has to be supplied from an external DC source.

During discharge, lithium ions spontaneously deintercalate from the graphite layered structure because of the existing electrochemical potential between the electrodes, thus oxidizing the negative electrode. The lithium-ions that have abandoned

[3]The Gibb's free energy is normally expressed in thermodynamics as a function of the variations of enthalpy, H, and entropy, S, as $\Delta G = \Delta H - T\Delta S$. In electrochemical cells, the equation is usually rewritten as $\Delta G^0_{cell} = -nFE^0_{cell}$, where the decrease of the Gibb's energy is a function of the number of moles of reaction, n, the Faraday constant, F, and the theoretical potential of the cell, $E^0_{cell} = E^0_+ - E^0_-$, related to the potential of the electrode materials the cell is made of.

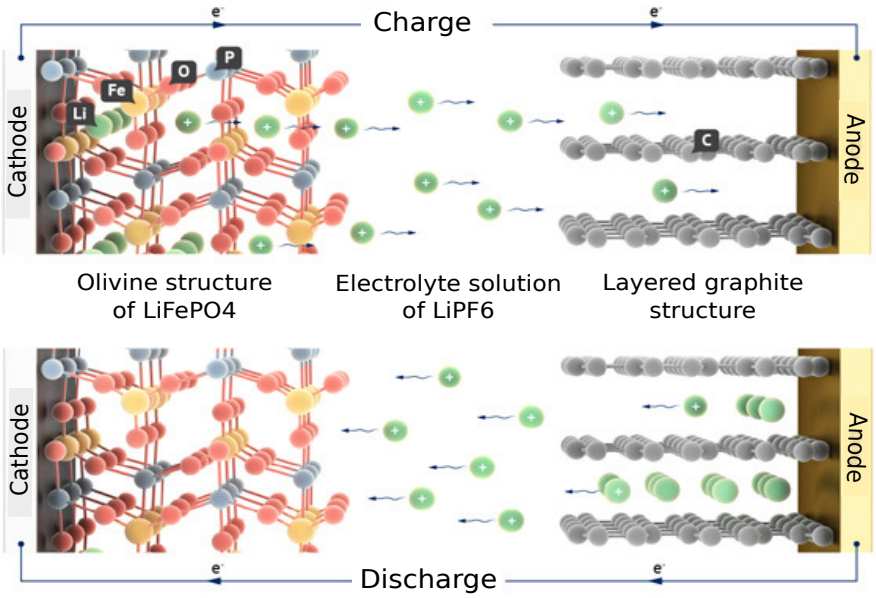

Figure 2.2: *Graphical schematic of the operating principle of a lithium-ion cell. Figure adapted from [56].*

the negative electrode, or anode, are conducted by the electrolyte solution and are eventually absorbed in the positive electrode, and get intercalated within the positive electrode material structure causing reduction of this electrode. As a consequence, electrons flow from the negative electrode to the positive electrode through the external circuit. The electric current can perform work at the external load, and the cell acts as a power source.

Since, as we can see in the Figure 2.2, the lithium ions are "rocked" between the two insertion electrode materials during cycling, these electrochemical cells are oftenly referred to as "rocking-chair" cells, or dual lithium-ion insertion cells [84].

The electrochemical reactions for the discharge of the LFP [4] lithium-ion battery are described by the following reactions [88]

$$LiC_6 \xrightarrow{discharge} xLi^+ + xe^- + Li_{1-x}C_6 \tag{2.3}$$

$$xLi^+ + xe^- + Li_{1-x}FePO_4 \xrightarrow{discharge} LiFePO_4 \tag{2.4}$$

being 2.3 the anodic reaction at the negative electrode, and 2.4 the chemical process occurring at the positive electrode or cathode, and being x the number of moles of lithium ions that are deintercalated from the anode and intercalated in the cathode.

[4] The electrochemical reaction is presented for the lithium iron phosphate cathode chemistry, since this is the chemistry of the battery that is analysed and modelled in this work.

During charge, the processes inside the cell (reactions 2.3 and 2.4) are reversed. In this case, the processes do not occur spontaneously and are not driven by the electrochemical potential anymore, but instead need to be stimulated from an external electrical power supply connected to the positive and negative current collectors. The external power supply, which must provide a higher voltage than that of the discharge processes, enforces the reactions in the reversed direction because of charge conservation.

Self-discharge must also be mentioned here. This phenomenon explains why batteries reduce the stored charge, or energy, without any connection between the electrodes due to internal chemical reactions. How fast self-discharge in a battery occurs is dependent on the type and components of a battery, its state of charge, and the ambient temperature inter alia.

Battery Overpotentials

When a current flows, either when charging or discharging the battery, a shift in the potential of the cell in comparison to the equilibrium open-circuit voltage (OCV) can be observed. This deviation is called overpotential, and is originated in general in electrochemical cells from different physical sources. Hence, the overpotential can be divided into many different subcategories, which are not all well defined and distinguished in the literature. The most common distinction is:

1. Ohmic overpotential: It refers to the sum of all the effects that lead to an instantaneous, and proportional to the current, drop in voltage when a current is applied. This effects, which are appreciable without almost any time delay after a current change, are contributed by the bulk ionic resistivity of the electrolyte and the separator and by the ohmic resistance of the current collectors. (ref? molaria)

2. Activation overpotential: This is the potential difference, above the equilibrium potential, which is required to produce a certain current. It is oftenly also called charge-transfer overpotential, and depends on the activation energy of the redox event within the cell. In general, a higher overpotential is generated with higher charge transfer speed, following the Butler-Volmer and the Tafel equations [43].

3. Concentration overpotential: Concentration overpotential spans a variety of phenomena that involve the depletion of charge-carriers at the electrode surface. The main contribution is the so-called diffusion overpotential: When high

current densities at the electrodes exist, depletion of the reacting substances at the electrode surface results in a concentration polarization. Therefore, in these conditions, the reaction kinetics are determined only by the diffusion processes within the electrode and the SEI.

Other physical sources of polarization, with much smaller contributions in the total overpotential in most of the operating conditions, are usually grouped or attributed to the three previous categories. For example, the so-called reaction overpotential can be considered within the activation overpotentials, and is only relevant when lithium adsorption and desorption in the electrode-electrolyte surface is the reaction-rate limitant. Another example would be the crystallization overpotential, which is only important during metal deposition occurs, normally during charging at low temperatures, and can by analogy be understood as a source of concentration overpotential.

Knowing and differentiating between the source of different electrochemical overpotentials, and with the idea in mind that some of the physical phenomena behind them act slower than others and, thus, different overpotentials can be detected at different time scales, note that the dynamic response of the voltage of the battery when applying a current pulse can give a deep insight into the internal electrochemical processes of a battery.

2.2.4 Battery Ageing

The properties of batteries are known to change during storage (calendar or calendric ageing) and operation (cycle ageing).

The degradation of a lithium-ion battery has been intensively studied during the last few years, and several studies have been published to investigate the influence of different battery operating or storage conditions ([31], [32]). The most pronounced ageing effects are capacity fade and impedance rise [33], and the most important attributed ageing mechanisms are the formation and growth of the solid electrolyte interface (SEI), the consumption of electrolyte, and/or the mechanical degradation of the electrodes or the current collectors [34].

The main factors that influence the battery cyclic ageing are the operating current, the temperature, and the SOC interval within which the batteries cycle, while in calendric ageing the biggest factors are the temperature and the SOC at which the batteries are stored [35].

As explained in [36], the physico-chemical understanding for much of the ageing phenomena is still incomplete. Due to the lack of necessity for the understanding

the present work, and for concision, a deep revision of such mechanisms is kept outside of the scope of this thesis. However, the effects of temperature on battery degradation are explained in depth in the following chapter (2.3). For completion, if the reader is interested in a deeper and more complete understanding of the degradation mechanisms in lithium-ion batteries, the work of Vetter et al. [35] and the complete reviews on the topic by Barre et al. [37] and Jalkanen et al. [32] are recommended lectures.

State of Health

The *state of health* (from now on, SOH) is a figure of merit of the condition of an electrochemical cell, battery, or battery pack. The SOH is the ratio between the capacity of a battery at a given time, $C_{bat}(t)$, and the nominal capacity, $C_{bat,N}$. It is defined as

$$SOH(t) = \frac{C(t)}{C_N} \tag{2.5}$$

and is usually expressed as a percent magnitude. Typically, the battery manufacturers provide the products at 100% SOH or higher, and this will decrease over time due to storage time (calendric ageing), and/or use of the batteries (cyclic ageing).

End of Life

The *end of life* (commonly shortened and written as EOL) of a battery is commonly taken at about 80% SOH, since most of the commercially available batteries show a very fast degradation behaviour after this point, approximately. Therefore, at this stage the battery is considered not to be useful anymore for most of the applications.

2.3 Thermal Issues on Lithium-Ion Batteries

Despite the existence of numerous lithium-ion batteries types and formats, it has been shown that, in general, temperature has a significant impact on duration or life, on performance, and on safety and cost [38]. This is not only true for lithium-ion technology but also for the vast majority among the rest of existing battery technologies, like lead-acid or nickel-metal hybrid batteries [39].

In this sense, most of the batteries are like humans, since they last longer and perform better in a reasonable and moderate ambient temperature. The ideal working temperature range to achieve a good balance between performance and life is shown to be, by most of the existing studies within the interval of 20 to 40°C.

In this section most of the effects of temperature on lithium-ion cells performance and degradation are explained by reviewing several experimental studies on this topic, in order to understand and motivate why thermal issues play a key role for the deployment of this energy storage technology on the BEVs and HEVs market. For a further insight, the critical review on thermal issues of lithium-ion batteries presented by Bandhauer et al. [27] can be addressed.

2.3.1 Cold Temperature Effects

Improvement of low temperature performance is a priority for the development of BEVs and HEVs batteries, since temperatures below 0°C have many negative consequences on lithium-ion battery performance. Electric cars, however, must be able to operate at cold temperatures, which might occasionally or frequently (depending on the climate) be requested. In some extreme climates, even temperatures down to -40°C must be tolerated.

The exact mechanisms leading to a poor performance of the cells are complex and are still under debate, due to the overwhelming number of commercially available and tested electrode and electrolyte materials [40]. Nonetheless, it is clear that the performance of lithium-ion batteries is reduced at low temperatures for all cell materials [36]. For example, Nagasubramanian reported that a commercial 18650 lithium-ion battery delivered, at -40°C, only a 5% of the energy density and a 1,25% of its power density as compared to the values at 25°C [41].

The most important and reported causes of the deteriorated cold temperature performance of batteries are presented in the following paragraphs.

Analysing electrochemical impedance spectroscopy (EIS) experimental data, Andre et al. related the observed strong mid frequency impedance changes at low temperatures to the recession of chemical processes celerity. Particularly, to the strong dependency on temperature of the diffusion and charge-transfer processes [42]. Moreover, Zhang et al. concluded from EIS observations taken at sub-zero temperatures that the performance of lithium-ion at low temperatures is mainly affected by the charge-transfer resistance of the battery, accounting for the Faradic reactions taking place on the electrode-electrolyte interfaces. They showed that the charge-transfer resistance, and its relative double layer capacitance (related to SEI growth), increased exponentially at temperatures below 0°C [40]. Reduced ionic conductivity is attributed to SEI growth by other authors, in [44] and [45], since the ionic conductivity of the SEI is much lower than that of the bulk electrolyte [47].

Besides, when the transport rate of lithium ions exceeds the rate on which they can be inserted or diffused on the anode, the deposition of metallic lithium on the

surface of the SEI is promoted. Lithium deposition breaks and pierces the SEI, which causes a re-building and further increase of the SEI. Huang et al. [48] argued, in this direction, that the SEI layer growth and the poor charge-transfer related to it cannot explain the big difference between the discharge and charge capacities at low temperatures. Therefore, the limiting factor at low temperatures must be the low diffusivity of the electrode. Lithium deposition, or lithium plating, is mentioned as one of the most degrading effects in cells with graphite anode [31], and occurs mostly during charging processes. It implies an irreversible loss of active material and an irreversible energy capacity loss. Pesaran, et al. also substantiate the increase of plating at low temperatures by the changes of the viscosity on the bulk electrolyte [38], which is also consistent with the sluggish ion transport attributed to the charge-transfer resistance increase. The increase of electrolyte viscosity and its declining ionic conductivity with decreasing temperature can be a source of severe mechanical degradation in the negative electrode material: the insertion of lithium ions that are still being surrounded by their shell of solvent molecules could cause exfoliation of the graphite layers on the anode [49]. In any case, poor electrode kinetics, high SOC, and high charging rates are known to be the main factors that promote lithium plating [40]. For that reason, Fan and Tan, which studied the effect of different charging procedures at -20°C, recommend avoiding high charge rates, even in short pulses, to limit the irreversible capacity fade [50].

Furthermore, the deposition of solid lithium can lead, depending on the negative electrode material, to dendrite formation, although, as explained by Waldmann et al. [51], lithium dendrites have never been created or observed on lithium-ion cells with graphite anodes, even if the models suggest that this may happen. Dendrite formation would undoubtedly compromise the safety, since it may lead to an internal short-circuit that can evolve to thermal runaway.

On the other hand, the heat generation rate at low temperatures of the batteries is raised as a result of the internal resistance increase. It has been seen that self-heating improves substantially the battery performance (i.e., in [52], the discharge capacity increases from $100mAh$, in isothermal conditions at -20°C to $2200mAh$, if the battery operates under adiabatic conditions). Although, sufficient warm up for normal operation at cold conditions must be aided by some external or internal heating system [53].

Summarizing, power capabilities are reduced under cold temperatures due to the increase of the cell internal impedance due to SEI growth, whereas energy capacity is irreversibly lost, mostly because of accelerated lithium plating (especially during charging) and loss of active material related to the growth or repair of the SEI.

Impedance increase raises internal heat generation, but self heating does not usually sufficiently warm up the batteries for normal operation.

2.3.2 Hot Temperature Effects

Capacity and Power Fade

The charge and discharge capacities of a lithium-ion battery raise with increasing temperature, as well as the operating voltage (related to the power capabilities), due to the decrease of diffusion and charge-transfer resistances. However, capacity and power irreversible degradation is proved by many studies to be accelerated if the battery temperature increases beyond 40°C or 50°C, regardless of discharge rate and/or cell chemistry [27].

For example, studies [54] and [57] from Ramadass et al., for repeated cycles of a 18650 prismatic LCO cell between 0% and 100% SOC, showed that the capacity faded 70.6% when maintaining the battery temperature at 50°C, while for the same number of cycles and an operating temperature of 25°C, the capacity fade was only 22,5%. They argue that the main factor explaining the huge capacity fade at high temperatures is the degradation of the negative electrode. With similar experimental cycling settings, Ehrlich [58] obtained a 44% and a 82% higher capacity fade, for LCO and LMO chemistries, respectively, at 45°C, as compared to the values obtained at 21°C. Still, full charge and discharge cycles, like the ones tested in the above mentioned studies, are not commonly performed in BEVs and HEVs. Instead, the batteries in such applications tend to operate in a narrower SOC range as near the fully charged and fully discharge states the power capabilities of any battery are limited. However, Choi and Lim [59], which cycled at 1C current rate LCO cells at 25°C, concluded that there is no appreciable difference in capacity fade due to changes in SOC cycle ranges. Belt et al. [60] prove again that the capacity fade is not a strong function of DOD, but conversely conclude that power fade is a function of DOD and attribute this to positive electrode breakage [27].

Using X-ray diffraction (XRD), nuclear magnetic resonance (NMR), scanning electron microscopy (SEM), and X-ray photo-electron spectroscopy, Bodenes et al. [61] attemped to give more information on the insights of the effects of high temperature degradation mechanisms. They indicated that the formation of a binder layer, similar to the anodic SEI, at the surface of the positive electrode led to poor lithium re-intercalation, and they also showed that several changes in the composition of the SEI occur at high temperatures. Similarly, the study from Leng et al. [62], analysing an LCO cell from 25°C to 55°C, concludes that the increase of

degradation rate of irreversible capacity loss with temperature is due mainly to the formation and modification of the surface films on both electrodes, but they also argue that structural and phase changes of the LCO cathode have a great influence on ageing. Amine et al. [63] presented similar conclusions for their studies of LFP cells, observing deterioration of the cathode (more precisely, observing dissolution of iron ions in the electrolyte) and also the effects of SEI repair and growth.

Thermal Runaway

Apart from capacity and power fade effects, the most dreaded and hazardous effect in lithium-ion batteries is the so-called thermal runaway, which can occasionally lead to fire or even an explosion of the batteries. Logically, this is one of the primary reasons that delay the broad introduction in the BEVs and HEVs mass market, since thermal runaway compromises the safety of the system, which mustn't be endangered at any point.

As stated in [64], thermal runaway might appear in batteries as a result of abusive conditions, namely: overheating from maintained high current rates or from excessive high ambient temperatures, or battery overcharging. Once the thermal runaway starts, very exothermic chain side reactions may be triggered, building up uncontrollably the temperature and the internal pressure due to gas outcasting, and promoting even faster and more hazardous chemical reactions. More precisely, the process starts when the SEI film that normally protects the lithiated carbonaceous electrode from reaction with the electrolyte and contains both stable and metastable components, starts decomposing, which occurs when the temperature reaches the threshold between 90°C and 120°C. In consequence, the electrolyte and the electrode begin to react exothermically (although the reaction might be limited due to the soluted salts, as $LiPF_6$) with a peaking temperature at around 200°C. As explained by Yang et al. [12], after the SEI being decomposed, the electrolyte evaporates at around 140°C and the separator is melted between 130°C and 190°C. This phenomena causes further problems, such as the possible combustion of the vaporized electrolyte (which might be triggered when the positive electrode –i.e., a layered oxide– casts oxygen and other gases). In addition, a melted separator can cause an internal short-circuit which generates even more heat. All these chain reactions lead eventually to fire or even a catastrophic explosion at around 400°C to 600°C.

For that reason, a great number of researchers have focused on the study of these events, to achieve deeper knowledge on the vulnerability of the cells to the main causes of this phenomenon. Recently, Finegan et al. [13] proposed a combined *in-operando* and multi-scale X-ray computed tomography as a comprehensive ap-

proach to understanding battery failure, and observed that with increasing SOC, the chemical energy release of thermal runaway increased, too, posing the overcharge as the most catastrophic and dangerous conditions for lithium-ion cells. Similarly, Al Hallaj et al., who slowly heated up an LCO cell in 5°C increments to identify the temperature onset of thermal runaway, found that the onset happened at lower temperatures for higher battery voltages [14]. Spotnitz and Franklin [65] investigated the external short-circuit event using a 1D simplified model and observed that, in this case, the ohmic loss heat raised the temperature so fast that the positive electrode and electrolyte reaction started before the other reactions could progress significantly. Kim et al. presented both lumped and three dimensional thermal models that simulated various side reactions inside the battery under abusive conditions [15], and extracted conclusions on the effect that the battery aspect ratio ($Area/Volume$) has in relation to the thermal runaway onset.

Most of the current research on improving safety and prevention of this kind of hazardous events in lithium-ion batteries is focused on current-limiting or pressure releasing devices, safer positive electrodes and electrolytes investigation, special electrolyte coatings and additives [16], and optimization of heat dissipation and temperature control systems.

Knowing that the reaction between positive electrode and electrolyte is the most dangerous of all, it is worth mentioning that the $LiFePO_4$ cathode material has been shown to possess the best thermal stability and release the lowest amount of heat when reacting with the common electrolytes as compared to the other available cathode materials, since they contain quite unstable elements such as manganese, cobalt, or nickel. For its inherent better thermal stability, the projection of this cathode material for BEVs application has high expectations, even if its energy density is considerably lower than other chemistries.

2.3.3 Storage Temperature Influence

The degradation of lithium-ion batteries in time, without any use of them, is denominated calendar ageing, and is mainly related to the self-discharge of the cells due to the non-ideal ionic isolation of the electrolyte, and to the steady SEI growth, although the calendric steady SEI growth celerity is often negligible as compared to the cycling one [34].

In general, the calendric capacity fade is described as a function of the time, the temperature and the SOC at which the cell is stored:

$$\Delta C_{bat} = f(t, T, SOC_{storage}) \tag{2.6}$$

At higher temperatures, faster ageing is expected due to accelerated surface species (SEI) dissolution, increased electronic conductivity, and increased rate of self-discharge. Thomas et al. announced that calendric power fade is primarily dependent on temperature, especially in the first 4 weeks of life [66].

In most of the cases, the effects of T and $SOC_{storage}$ are reflected in the function $f(t, T, SOC_{storage})$ as a coefficient α_{cal} that multiplies a polynomial function of time. This coefficient is often empirically related to an Arrhenius-like law as

$$\alpha_{cal}(T) = k_0 \cdot e^{\frac{E_a}{RT}} \tag{2.7}$$

since this law can be related to the rate at which the side reactions take place. R is the gas constant, E_a is the activation energy, T the absolute temperature, and k_0 is an empirical constant. The effect of the $SOC_{storage}$, which is much smaller than the effect of the temperature [67], is normally related to the activation energy, E_a[34].

2.3.4 Other Effects of Temperature in Lithium-Ion Batteries

Electrical Imbalance

As can be deduced from the explanations above, battery capacity can be a strong function of temperature, due to the strong influence that the temperature has on the most important degradation mechanisms of the lithium-ion cells. Hence, cells operating at different temperatures inside a battery pack may lead to electrical imbalance of them.

When batteries with mismatched capacities are connected in series, the weakest cell normally limits the performance of the serial battery pack. As shown by Kuhn et al. in [68], charge equalization extends usable life, and because of that, thermal gradients may affect considerably the degradation of battery packs.

Besides, charging a battery pack with imbalanced capacity cells connected in series may cause the weaker cells to be overcharged (that is, over the maximum cut-off voltage). As explained in the previous section 2.3.2, overcharging is not tolerable in many of the existing lithium-ion chemistry technologies, as it may carry side reactions that can lead to thermal runaway.

Effects on OCV

Both Thomas et al. [69] and Reynier et al. [70] established the existence of a linear dependence of battery open circuit potential with battery temperatures between 20°C and 29°C.

Thus, the effects of temperature on the OCV, U_{oc} are usually approximated by a first order Taylor series expansion as

$$U_{oc}(T) = U_{oc}(T_{ref}) + (T - T_{ref})\frac{\partial U_{oc}}{\partial T} \tag{2.8}$$

where the term $\frac{\partial U_{oc}}{\partial T}$ is the so-called entropic coefficient, which has a relevant importance in the batteries heat generation, as it will be covered in the following section 3.2.1, and T_{ref} is a reference temperature.

Other studies have concluded, too, that the entropic coefficient for LFP cells is constant among the majority of the SOC range, having only slight variations (nonlinearities in temperature dependency) near fully charged and fully discharged states [71].

Chapter 3

Modeling Strategies for Lithium-Ion Batteries

In most applications, a battery system consists of the battery, or battery pack, an electronic battery management system (BMS), and a battery thermal management system (BTMS).

The technologies related to electrified vehicles have a promising near future, since, to this day, they are the best and most competitive alternative to replace fuel vehicles. The projected mid and long term growth of the BEVs and HEVs market will have a tremendous impact not only on the reduction of greenhouse gases but also on the electricity distribution systems [72].

The deployment of BEVs and HEVs is closely related to the battery technology development. In such applications, the battery system size must scale up to around 15kWh or more in order to offer driving ranges similar to those of gasoline cars (400-600km) [64]. The design of such large battery packs presents a daunting number of technical challenges for meeting the high reliability, durability, and safety standards in the automotive sector.

Numerical simulation has contributed for decades in the automotive sector development. However, batteries are very different from the products that automotive manufacturers are used to work with, and deep and precise knowledge of its operation is required since slight deviations from the proper working margins can lead to dramatically shortened battery life and even to serious safety hazards. Furthermore, the design and selection of an adequate simulation framework for lithium-ion batteries is challenging, because a wide variety of models can be used to describe different phenomena or physics.

Generally, the different simulation approaches can be classified by their objec-

tives, which are usually related to the physics scale that is modeled. Hence:

i. Detailed models and submodels are necessary to simulate the electrochemical and physical phenomena inside the cells to improve cell and battery design, to give understanding on battery degradation phenomena, and to predict hazardous effects.

ii. Precise system level models of battery modules or packs (which can comprise hundreds of cells) are needed, i.e. for the design of battery thermal management systems (BTMS).

iii. Finally, lumped or simplified system-level models need to be integrated within the system model of the entire powertrain and vehicle to control and monitor the battery state at real-time during operation.

Hence, in the simulation of batteries, it is very important to have a clear idea of the objectives pursued, because "the best possible physics-based model can depend on the type of issue being addressed, the systems engineering objective, and on the available computational resources"[36].

Apart from the required complex modeling tools, and as a validation tool for the assumptions and the derivation of such, reliable experimental measurement tools are necessary for testing and evaluating battery performance, degradation, and thermal characteristics.

This chapter includes a wide overview on the state of the art of lithium-ion battery modeling and experimental characterization strategies, covering the most important fields related to the development of the BTMS.

First, a necessary overview on the state of the art of the modeling strategies of electrical –or electrochemical– modeling of batteries (section 3.1) is included. The next section is related to the theoretical and experimental characterization of the battery heat generation rates, which are fundamental for the development of proper thermal management systems for batteries (section 3.2.1).

3.1 Electrochemical Modeling of Lithium-Ion Batteries

Accurate modeling of the electrical behavior of a lithium-ion battery is important for a proper integration and operation of the battery system within the external electrical and electronic systems or networks.

The main objectives of electrical modeling are: first, to predict the terminal voltage of a battery under any input conditions, which is needed to prototype,

design and test complex electric and electronic systems; and second, to predict battery lifetime, or degradation, needed for precise system costs estimation [73]. Thus, in practice, the main challenges are to estimate accurately the so-called state of charge (SOC) and state of health (SOH) of the battery [74].

Many different mathematical models with those purposes exist, varying widely in terms of abstraction, complexity, computational requirements, and reliability of their predictions, although finding efficient ways of simulating battery systems is still an active area of research [36].

The simplest approaches are ideal models or simple phenomenological mathematical models (such as the Shepherd, Nernst, or Peukert models). Apart from these, the applicability of which is infeasible in practice, since they are limited to special operating conditions, mainly two SoA strategies for modeling the complex electrochemical behavior of lithium-ion batteries do exist:

- Equivalent circuit (EC) models: An empirical approach that attributes the different electrochemical overpotentials, caused by different physico-chemical processes inside the cell, to different circuit elements in an equivalent circuit topology.

- Physics-based electrochemical models: They intend to detail the basic, spatially distributed electrochemical processes, which include mass transfer, fluid mechanics, reaction kinetics, and thermodynamics physics

In the following sections 3.1.1 and 3.1.2, a brief overview on both alternatives is depicted, trying to spotlight some of the major drawbacks and advantages of each.

3.1.1 Equivalent Circuit

The idea behind equivalent circuit (EC) models is to model and reproduce the battery behavior by an analogous electrical equivalent circuit. Considering the battery as a black box, and through analysing the voltage response of the battery at its terminals under different conditions, the internal processes of the battery can be related to a fictitious electrical network. Analogously to *Thévenin's equivalent* ideas, the EC battery models consist mainly of a voltage source, which corresponds to the open-circuit voltage (OCV), and an impedance in series which determines the overpotential of the battery under charge or discharge processes.

The spatial distribution of the real physical system is neglected and only the battery overall voltage response is modelled (in a zero-dimensional space, thus), by the use of finite differences numerical schemes for the time integration. This

simplification reduces the computational effort immensely, as compared to physical models with spatial resolution. It is due to its speed and versatility that EC models are the prevalence choice for the BMS design for portable electronics, and are also extended to the development of BMS systems for lithium-ion batteries in automotive or energy storage applications, as we can see in recent publications [75, 76, 77, 78].

Equivalent circuits have a corresponding U-I characteristic only from the point of view of the load, and Thévenin's theorem is only valid for linear circuits. Hence, in practice, the EC for modelling the behavior of lithium-ion batteries need to be defined within small parameter intervals, as in linearization techniques [79], since the battery behavior can only be considered as a linear circuit if small SOC (or current rate, or ambient temperature) ranges are considered.

EC Impedance

The model impedance can vary from very simple schemes to very complex networks, such as the extended Randles model shown in Figure 3.1, and a simple ohmic resistor being the simplest model. In complex EC circuits, the different physical sources of cell overpotentials (recall section 2.2) are attributed to different impedance elements.

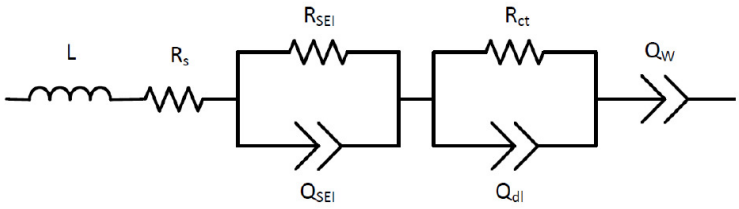

Figure 3.1: *Equivalent-circuit topology of the extended Randles model. Figure reprinted from [34].*

The ohmic overpotential, or ohmic polarization, that causes a sudden voltage drop proportional to the current, is represented by an ohmic resistor, R_s. Activation, and concentration overpotentials, which result from more complex and transient physical processes within the cell, are usually treated as a combination of resistive and capacitive elements, since they are a combination of energy dissipative and energy storage phenomena. Thus, they are modeled by a parallel combination of a resistor and a capacitor: the so-called RC-circuit, the impedance of which is determined by the Fourier's transfer

$$Z_{RC}(w) = \frac{R}{1 + jwRC} \tag{3.1}$$

where w is the angular frequency, j is the imaginary vector unit, and R and C are the parallel resistivity and capacitance that conform the RC impedance.

As suggested in [34] and [80], substituting the capacitor of such an impedance (RC-circuit) by a constant phase element (CPE), which is a theoretical impedance element with a more versatile transfer function, the impedance that can be observed in batteries can be fitted or approximated more accurately. In this case, the parallel circuit of a resistor and a constant phase element is oftenly called ZARC.

A characteristic parameter of such impedances (RC and ZARC elements), is their time constant τ, which determines the time (or velocity) in which this impedances reaches steady values. The time constant of such elements is therefore an indicator of the time scale, or the celerity, of the time that the different impedance overpotentials take to get established. For that reason, and knowing that the different electrochemical overpotentials are manifested, or set at different velocities, each of these complex impedances can be attributed to different physical processes, giving some phenomelogical sense to each of the EC parameters. Usually, a first (and faster) RC or ZARC impedance represents the surface diffusion layers on the anode (the so-called SEI), and a second one (slower) represents the charge transfer and the double layer resistances. Finally, the diffusion limitations can also be taken into account by Warburg elements.

Parametrization of EC

For obtaining the impedance parameters for the EC mainly two different characterization techniques are reported:

1. Current pulse measurements: The battery or cell is subjected to current pulses at different SOC, after each of which a sufficient relaxation time is set to lead the battery to a relaxed state. The typical dynamic evolution of the voltage, in time, due to the current pulses is shown in Figure 3.2. Different methods (such as the *current switch* or the *current-off* methods [81]) can be used to fit every EC impedance parameter in order to minimize the error of the EC model voltage response to the obtained experimental data.

2. Electrochemical Impedance Spectroscopy (EIS): The electrochemical impedance is obtained by applying different high frequency AC sinusoidal currents to the battery and measuring the voltage between the terminals. Here, the complex impedance spectrum is usually represented, by convenience, in a Nyquist plot[1],

[1] In a Nyquist plot, the Fourier transform of the transfer function of the impedance is represented as a complex number by $Z(w) = Z_0 \exp j\phi = Z_0(\cos\phi + j\sin\phi)$

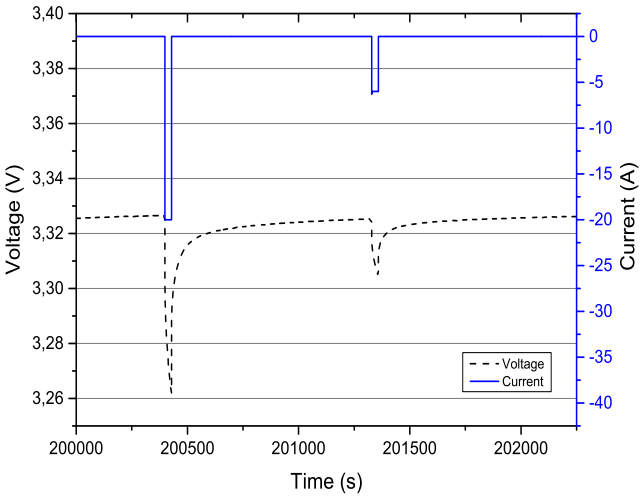

Figure 3.2: *Voltage response of the battery of study under different magnitude current pulses.*

an example of which is shown in Figure 3.3.

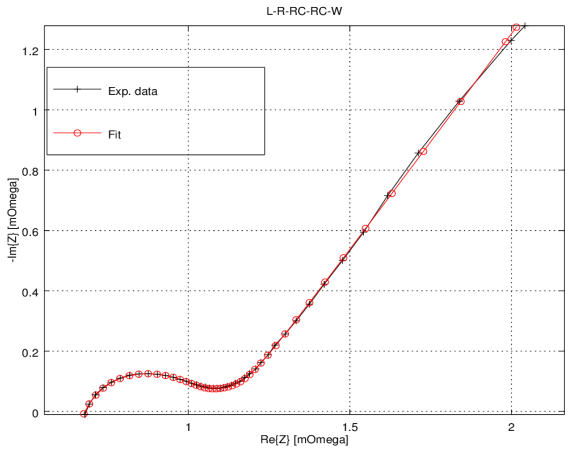

Figure 3.3: *In black, Nyquist plot of the empirical impedance spectrum of a fresh battery sample at 50% SOC, obtained by EIS measurements with a frequency range of* 2kHz-0.01Hz. *In red, plot of the impedance of the extended Randles EC model with fitted parameters.*

Shortcomings of EC Models

In EC modelling, the degradation effects are often considered empirically as well, using a similar strategy than the one which is used to fit the EC parameters, based on extensive databases that are obtained from battery testing under various operating conditions and loads. However, the relationship between failure modes during the test conditions and those during actual operating scenarios has not been clearly established [36], and often the testing conditions cannot reproduce or cover the overall real application conditions.

Regarding the degradation, many attempts have been made to relate the EC parameters evolution to extract conclusions on the phenomenological aging phenomena inside the battery cells. The degradation is generally attributed to the loss of active materials and growth of SEI layer [82].

Linked to the previous point, however, one of the main drawbacks of EC models is that the usage of complex equivalent circuits, which normally fit the battery's dynamical response better, translates into replacing a complex electrochemical model into a complex empirical model with a large number of parameters to fit. Hence, the physical intuition behind the meaning of the impedance parameters is usually lost, and the parameters turn into mere *fitting parameters* [79].

Another major shortcoming of this strategy is that, since the battery impedance is a complex, nonlinear, and time dependent variable, it has been seen that the measurement frequency and current amplitude affect the impedance estimations. Therefore, the outcome of the internal impedances are also dependent of the data gathering processes [83] and, for that reason, the applicability of the EC models is limited to the current amplitude range that has been employed within the empirical obtaining of the model parameters and to the time scales, or frequencies, at which the pulses have been applied.

3.1.2 Physics-Based Models

Physics-based electrochemical engineering models for lithium-ion batteries, which incorporate transport phenomena and chemical and electrochemical kinetics, were pioneered from the University of Berkeley by Doyle [84], Rao and Newmann [85], and Bernardi et al. [86], and have existed for more than twenty-five years now.

Normally, the physics-based models are solved in a finite elements formulation within a one-dimensional domain (e.g., the models presented in [87, 88, 52, 89, 90]), and the focus is usually the cell level. In most of the literature publications, the aim of such models is to give a better understanding on the micro-scale knowledge

of the battery processes.

Thanks to this modeling strategies, the knowledge on the sources of the battery shortcomings that are observed and reported from the battery system perspective (namely the SEI formation and growth, the loss of active lithium, the undesired side-reactions, and the mechanical degradation of the electrodes) has recently been extended considerably thanks to the inclusion of some stress-strain models, molecular dynamics, and different stochastic approaches to the basic electrochemical balances (presented in the next section, *State-of-the-Art Electrochemical Physics*).

Besides, two and three-dimensional spatial resolutions have also been presented recently [91, 92], and are expected to be a powerful tool for the improvement in the design and energy density of the cells by the optimization of the electrode materials composition, the active particle's size, or the thickness of the cell components [7]. Another main application of the models with spatial resolution is the improvement of the energy density of the batteries, i.e., to improve the battery design by the optimization of the electrode materials composition, the active particles size, or the thickness of the cell components ([92], [87]).

Last but not least, multi-scale multi-domain strategies are arising lately, such as the models presented by Kim et al., in [93] and [94], and Kostetzer [95] and attempt to couple the micro and macro-scales. These approaches seem promising since the good resolution of the electrochemical physics models can be taken into account in the battery stack level simulations.

State-of-the-Art Electrochemical Physics

Hereafter, and referring to the governing equations that dictate the electrochemical processes inside a cell, the main State-of-the-Art (SoA) physics-based models are presented. Sorted according to increasing complexity and predictability:

i. Single-particle models (SPM). The transport phenomena is taken into account in a simplified form, considering a single reference particle of each electrode, neglecting the concentration and potential effects in the solution phase between the particles [96]. This is only valid for low current rates and thin electrodes [97, 79].

ii. Ohmic porous electrode models. The porous electrode that is included accounts for the solid and electrolyte potentials and current, and incorporates additional phenomena such as the dependency of ionic conductivities as a function of porosity. Usually linearizing or approximating the electrochemical kinetics equations, this model has been employed to design separator and electrode thicknesses [98].

iii. Pseudo-two-dimensional models. The derivation of the so-called pseudo-two-dimensional (P2D) lithium-ion transport model was led by the research group of Newmann et al., and implemented originally in FORTRAN by Doyle [84]. These models take account of the phenomena that occur inside lithium-ion cells under discharge and charge conditions, as well as during relaxation periods, expanding the porous electrode theory to treat the composite insertion electrodes as a surface charge transfer (governed by the Butler-Volmer kinetics) and a diffusion phase. Besides, concentrated solution theory accounts for the transport processes in the electrolyte liquid phase. Its general character and versatility made further battery understanding possible, and many similar models have been derived [99]. The inclusion of many internal variables that allow for improved predictive capability, despite of its greater computational cost, makes this model the one that is used the most by battery researchers. Moreover, it is adopted and implemented by most of the simulation software companies, such as Ansys [64], Comsol [100] or CD-Adapco [101].

Shortcomings

Physics-based modeling is a very active area of research and many methods and approaches are reported. However, there exist three major drawbacks that have limited its usage from a wide range of applications.

First, the intrinsic physical complexity of the model describing the different physics occurring within the electrodes and electrolyte, commonly lead to a big number of nonlinear partial differential equations (PDEs), whose effective solution requires advanced numerical techniques, even for the more simple models available in the literature such as the SPM model or the porous electrode P2D model. Hence, efficient ways of simulating battery models is an active area of research, and many investigators have tried to reformulate the models using different mathematical techniques and methods in order to speed up the physics-based models [102, 103].

Second, the model parameters correspond typically to microscopic material parameters, and are usually not directly observable or measurable during operation of the battery. Its observation is expensive and requires expensive and complex measurement tools and appropriate testing setups. Spectroscopic X-ray difraction (XRD), nuclear magnetic resonance (NMR), or scanning electron microscope (SEM) are common techniques [13], but require disassembling the battery sample components, which is expensive in terms of money and time. In consequence, the model parameters and the model assumptions have to be validated commonly by the comparison of operation experimental data and model predictions. Within this task, a

trial-and-error determination of battery design parameters and operating conditions is inadequate and has motivated the use of optimization techniques. Accordingly, the model simplification cited in the previous paragraph are also necessary for these tasks, and reformulated reduced models have lately enabled a greater use of common optimization techniques for models validation [104].

Yet, the third major shortcoming is that, although much literature related to capacity fade, SEI-layer formation, and other degrading processes exist, the physico-chemical understanding is still incomplete for many of the phenomena that occur inside a battery, and no existing model simulates all of the mechanisms for capacity fade or battery failure.

3.2 Thermal Lithium-Ion Models

Since the temperature is one of the most influencing factors on the electrochemical processes within a lithium-ion cell (recall section 2.3), accurate understanding of the characteristics of the battery heat generation is essential both for the reliability and predictability of the electrochemical models.

In the following sections, the theoretical principles and the derivation of the basic formulations that are reported in the literature for characterizing the heat generation in lithium-ion batteries are described, at first. Then, different SoA coupled electrochemical-thermal lithium-ion models will be reviewed to spotlight what are the tendencies and the selected engineering strategies that are currently in use in the field of the BTMS design.

3.2.1 Electrochemical Heat Generation

Heat production in electrochemical cells is related to each of the internal overpotentials described in section 2.2, the fundamental of which are the following three: activation or polarization –related to the interfacial kinetics, reaction and concentration –related to the concentration and diffusion of species within the active materials, and ohmic overpotential –caused by ohmic losses due to the movement of charged particles [86, 85, 27].

In the mid 1980s Bernardi et al. derived a general energy balance for a battery system by utilizing the first law of thermodynamics over the battery control volume [86]. The enthalpy changes of the active species within the cell were written as

$$\frac{dH_{bat}}{dt} = \dot{q}_{bat} - IU \tag{3.2}$$

where dH_{bat}/dt is the sum of the enthalpies of the different phases the term q represents the rate of heat transfer with the surroundings, and IU the electrical work.

Discrete phases interact with each other inside the battery. They assumed an average composition for each of these phases, and applied Gibbs-Helmholtz relation for each of the general species reactions, to obtain the rate of enthalpy change associated with the electrode reactions, mixing effects, and phase change processes. As a result, the previous equation 3.2 can be rewritten as

$$\begin{aligned}
\dot{q}_{bat} - IU = & \sum_{l} \left(I_l T^2 \frac{d\frac{U_{l,avg}}{T}}{dT} \right) \\
& - \sum_{j} \frac{d}{dt} \left(\int_{v_j} \sum_{i} c_{i,j} R T^2 \frac{\partial}{\partial T} \ln \left(\frac{\lambda_{i,j}}{\lambda_{i,j}^{avg}} \right) dv_j \right) \\
& - \sum_{j,j \neq m} \sum_{i} \left(\Delta H^0_{i_j \rightarrow m} - R T^2 \frac{d}{dT} \ln \left(\frac{\lambda_{i,m}^{avg}}{\lambda_{i,j}^{avg}} \right) \frac{dn_{i,j}}{dt} \right) \\
& + \frac{dT}{dt} \left(\sum_{j} \sum_{i} n^0_{i,j} \bar{C}^{avg}_{p_{i,j}} + \sum_{l} \frac{\int_0^t I_l dt}{n_l F} \Delta C_{p_l} \right) \\
& + \frac{dT}{dt} \left(\sum_{j,j \neq m} \sum_{i} \left(\bar{C}^{avg}_{p_{i,j}} - \bar{C}^{avg}_{p_{i,m}} \right) \left(n_{i,j} - n^0_{i,j} \right) \right)
\end{aligned} \tag{3.3}$$

where, regarding the terms on the r.h.s., the first term represents the *enthalpy of reaction* (or, what is the same, the sum of producible reversible work) and is derived from Gibbs-Helmholtz relation (assuming that there are several simultaneous electrode reactions) and the theoretical open-circuit potential to a reference electrode with average composition. The second and third terms account for the *heat of mixing*, which is produced when concentration variations across the battery are developed as a result of non-uniform reaction rates. When the current is interrupted, the concentration gradients relax causing heat to be absorbed or released. The two last terms reflect the heat energy that is related to the active material phase changes [85] [27].

The previous energy balance, however, is mostly employed in the literature (e.g., used in [105, 87, 88, 90, 6, 106]) in a simplified form which assumes an average heat capacity and isothermal operation conditions, and neglects the effects of enthalpy of species mixing, the ohmic heat in the current collectors and phase change terms. Due to this simplifications, the electrochemical heat generation rate can be rewritten

as a simple function of the operating current, voltage and temperature, (I, U and T), the open-circuit voltage (U_{oc}), and the entropic factor ($\partial U_{oc}/\partial T$) as

$$\dot{q} = \frac{1}{V_{bat}} \left(I(U - U_{oc}) + IT \frac{\partial U_{oc}}{\partial T} \right) \tag{3.4}$$

where U_{bat} is the volume of the active materials in the battery.

Some key features for the previous equation (eq. 3.4) are:

1. The first term is interpreted as the irreversible or polarization heat, and is indicative of all the irreversibile electrochemical processes, such as inner ohmic losses, charge-transfer phenomena, and diffusion of mass transfer limitations [7]. Note that this contribution is always positive since, for a positive current, $I > 0$, the working potential of the battery is higher than its open-circuit voltage (thus, $(U - U_{oc}) > 0$); for a negative current, $I < 0$, the overpotential is negative, $(U - U_{oc}) < 0$, since the operating voltage under discharge regimes is lower than the OCV, $U < U_{oc}$.

2. The second term is acknowledged as the reversible or entropic heat effect, and is related to the reversible electrochemical processes. Taking into account the sign of the current, this term takes positive sign during charge, and negative sign during discharge. However, the sign of the overall reversible heat generation is always conditioned by the sign of the entropic factor, $\partial U_{oc}/\partial T$, which in a lithium-ion battery has typically negative values at low SOC, and positive values at high SOC.

Regarding the assumptions or simplifications for the previous equation 3.4, it is here worth to mention that all the cited assumptions have been empirically demonstrated to lead to very small heat generation prediction differences in the case of small batteries. On the other side, the ohmic heat in the current collectors and the enthalpy of mixing terms can be considerable in big size prismatic or pouch batteries and, as recommended by Taheri et al. [30] and Lai et al. [89], should be taken into account for precise heat and temperature estimations.

3.2.2 Coupling electrochemical and thermal models

Reliable electrochemical-thermal models for battery systems are a must for the appropriate development and success of the imperatively needed battery thermal management systems (BTMS) [107], in order to enhance the security and the battery life of the battery packs. Besides, as stated by Latz and Zausch [108], multi-scale

coupled electrochemical-thermal models play a key role in the success of the acknowledgement of the battery degradation phenomena, since most of the battery processes are highly dependent on the temperature.

In most of the cases, and as we can see in Figure 3.4, a 0D or 1D electrochemical model is coupled with a 2D or 3D thermal model, and the interplay pf the two models is resolved in a dual-directional way: the average temperature of the thermal model is used in the electrochemical model, and the heat generation from the electrochemical model is applied to the thermal model in order to compute the next time-step temperature distribution. This is true regardless of the electrochemical model strategy that is selected, and recent publications show that thermal battery models are being developed to this end by the coupling of both empirical equivalent-circuit (EC) based ([95, 28, 109, 105]), and physics-based electrochemical models ([110, 108, 89, 88, 111]).

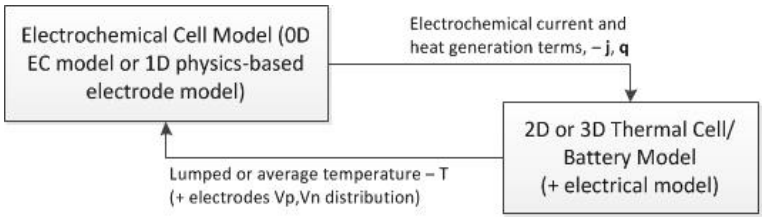

Figure 3.4: *Conceptual diagram of the most common modelling strategy and coupling approach for electrochemical-thermal battery models.*

Chapter 4

Battery Characterization

In this chapter, the experimental tools and procedures that have been used to characterize the electrical and thermal performance of the battery under study are presented, as well as the relevant results and their analysis and discussion.

Within the context of this thesis, the main objective of the electrical characterization of the battery sample is to found an electrochemical-thermal model for an acceptable prediction of the battery heat generation and temperature distribution. On the other hand, the thermal behavior of the battery sample is also experimentally studied in this chapter by calorimetric measurements and, in this case, the experimental data will serve as a validation tool for the developed numerical model of the battery.

In section 4.1, the battery which is studied in this thesis is presented, as well as its main characteristics, including some of the relevant data sheets and some weight and geometry measurements.

Section 4.2 presents the tests that were conducted for the characterization of the electrical magnitudes of the sample, including the OCV and the overpotential characterization, that are needed for the development of the empirically-based electrochemical-thermal battery simulation model.

In the last section, 4.3, the procedures for the conducted calorimetric tests are described and the obtained results are presented and discussed.

4.1 The Battery of Study

The battery of study is a pouch battery (or pouch cell) of A123 Systems, with a nominal capacity of 20Ah, and a lithium iron phosphate (LFP) based cathode material (Nanophosphate®). More precisely, the so-called AMP20*m1*HD-A, which

is designed for application in BEVs, HEVs, or long duration grid energy storage systems.

Figure 4.1: *Picture of the lithium-ion pouch cell studied in this work.*

The selection of this concrete cell for the development of this project has to be attributed to the market research work previously done by Ritter in [112].

4.1.1 Data Sheet Characteristics

The nominal capacity is 20Ah, and the nominal voltage is $3,3$A. The allowed current operation range from the provided data sheet, which is the range comprised in between the maximum and minimum recommended current rates, is shown in Figure 4.2. We can see that this battery has a high power density, since it admits discharge pulses up to 30 C-rate for periods of 10 seconds, which is unimaginable in lithium-ion cells of other chemistries.

Some of the specified influences of the temperature provided by the battery manufacturer are shown in Figure 4.3. In this figure, it can be observed that the optimal ambient temperature for the battery operation is around 20°C, especially regarding its cycling life: the red line plot shows that the total number of equivalent full cycles (EFC) that the battery can perform before loosing 25% of the initial nominal capacity (or, what is usually the same, reaching its end of life (EOL)), decreases linearly with increasing temperature, from around 6000 EFC at 20°C to only 1100 EFC at 55°C. Note that this can be translated into a decrease of 140 EFC for every degree Celsius of an temperature increase above 20°C. In BEVs or HEVs applications, normally no more than one or two EFC per day are expected, so the increase of degree Celsius of operating temperature above 20°C is translated into a depreciation of more than two months of the battery life.

In Figure 4.4, the influence of the storage temperature is shown, with data

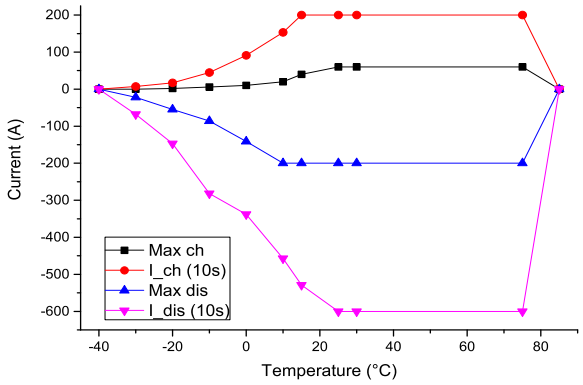

Figure 4.2: *Graphical representation of the battery current operation limits. "Max ch" and "Max dis" represent the limits for continuous full charge and discharge procedures, and "I_ch (10s)" and "I_dis (10s)" are the maximum allowed current of pulses for a duration of 10 seconds. Graph data from A123 systems data sheet.*

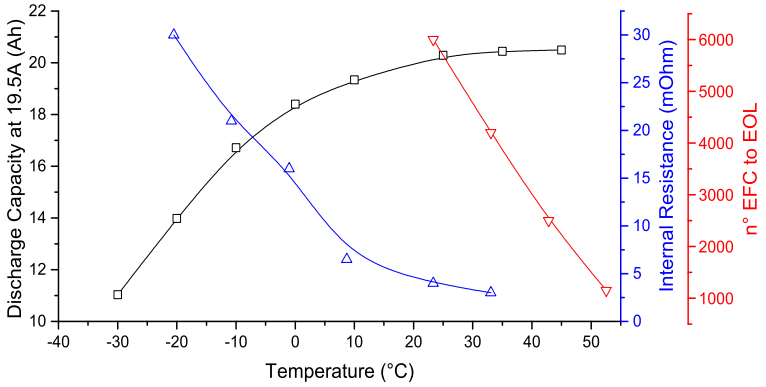

Figure 4.3: *Effects of the ambient temperature on: battery discharge capacity at a constant current of 19,5A (black); battery associated internal resistance (blue); and equivalent number of EFC to EOL (red). Graph data from A123 Systems data sheet.*

covering almost three years. It can be observed that temperature is a significant factor in calendar aging of the battery. Storage of the battery at high temperatures produces a very high capacity loss, which might be taken into account in the BTMS design.

4.1.2 Weight and Size

A total of 30 battery samples have been measured and weighted, and the average values of the weight and the geometrical measures are gathered in Table 4.1. The

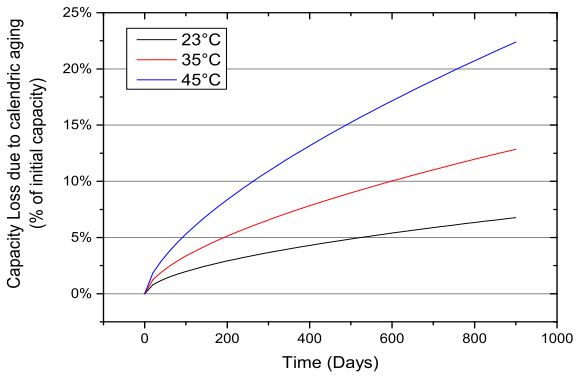

Figure 4.4: *Battery capacity loss as a function of storage time (calendar aging) at different temperatures. Graph data from A123 Systems data sheet.*

mass of the battery is m_{bat}. The total height, width, and thickness of the pouch battery are, respectively, h_{bat}, w_{bat} and z_{bat}. The thickness of the enveloping pouch material is z_{pouch}, and the current tabs thicknesses are $z_{tab,p}$ for the positive aluminum tab and $z_{tab,n}$ for the copper negative tab. Both current tabs measure w_{tab} width, and h_{tab} height from the active materials surface to its free-end.

Table 4.1: *Weight and geometry measurements of the battery of study.*

m_{bat}	493 g
h_{bat}	155,6 mm
w_{bat}	205,5 mm
z_{bat}	7,1 mm
z_{pouch}	0,3 mm

w_{tab}	45 mm
h_{tab}	50 mm
$z_{tab,p}$	0,3 mm
$z_{tab,n}$	0,25 mm

4.2 Electrical Characterization

In this section, the test procedures that have been used to obtain the electrical operating magnitudes that characterize the electrochemical battery model are presented. Basically, and as we can see from equation 3.4, the objectives are to characterize the battery open-circuit voltage (section 4.2.2) and the battery operating potential (section 4.2.3).

For completeness, and since in all the following sections almost all of the figures are plotted against SOC, it is here necessary to detail that the SOC the plots are based on is obtained from the capacity measurements that are performed before

every test[1].

4.2.1 Experimental Setup

Battery Tester

The battery tester that has been employed in this work for the electrical characterization of the cell is the ACT0550 from PEC. All the channels within this battery tester have a sampling frequency of 1ms and an operating range for the voltage of 0 to 5V, and for the current of -50A to 50A. The high accuracy of $\pm 0,05\%$ of Full Scale Deflection (FSD) for the voltage control, and of $\pm 0,03\%$ of FSD for the current control, is thus translated into a maximum fluctuation, or error, of the voltage and current control of $2,5$mV and 15mA. The measurement accuracy is $\pm 0,005\%$ of FSD for voltage; the maximum resolution for the current depends on the current range (see Table 4.2).

Table 4.2: *Current measurements resolution of the battery testing equipment.*

Current Range	50mA	500mA	5A	50A
Resolution	1μA	10μA	100μA	1mA

Cell Setup

Every PEC battery tester channel consists of four cables: two cables for the power supply, and two sensor cables for the temperature and the voltage sensors. Every sensor cable is composed of four cables. In the case of the temperature sensors, the four sens cables are welded to the four terminals of the sensor. In the case of the voltage sensor, only two cables are used, and are connected to the positive and the negative current tabs of the battery.

In order to connect the power cables to the batteries, and for ease of reuse, the batteries are placed onto a flat surface which incorporates two copper clamps that are fixed by screws to the battery terminals, ensuring a proper electrical connection between the power supply and the battery tabs. The copper clamps are prepared by the incorporation of a plug connector, which is also prepared in the power cables of the battery tester. This facilitates the connection with the battery tester for both the power and the voltage sensor cables (see Figure 4.5).

Three different test channels have been used for testing at different climate chambers, whose temperature is set to the values that are defined in *Experimental*

[1] In this work, the dis/charge capacity is always measured by standard CCCV procedures at 1C.

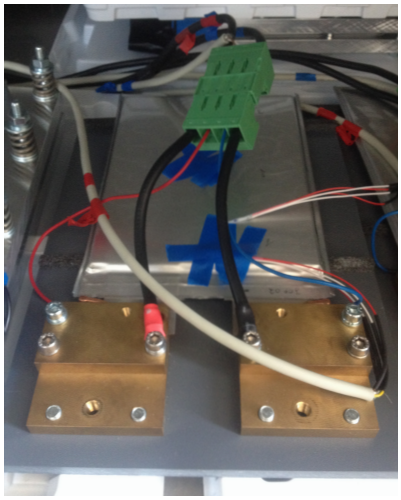

Figure 4.5: *Picture of the battery setup for the characterization tests in the climate chambers.*

Matrix in section 4.2.3.

4.2.2 Open-Circuit Voltage Characterization

As explained in section 2.2, the OCV is usually dependent on the SOC, the temperature, and the pressure. Normally, the effects of the pressure and the temperature are neglected in the OCV characterization, because their influence in OCV variations is some orders of magnitude lower as compared to the influence of the SOC. Besides, OCV measurements are usually performed at a controlled temperature, inside a climate chamber, and at a constant pressure.

Characterization Methods

In the literature are mainly two methodologies for characterizing the OCV as a function of the SOC:

1. One method consists of measuring the operating voltage at a very low current rate, assuming hence that the conditions during charge and discharge at a very low current are very similar to the equilibrium conditions. Thus, the measured terminal voltage is assumed to be close to the OCV. In this procedure, the battery is at first fully charged using a CCCV charging procedure and, then, discharged at low current (usually lower than C/10-rate) until the minimum cut-off voltage is reached. Subsequently, it is charged at the same rate until

fully charged. The measured voltage is plotted against SOC using the measured values of energy supply or extraction to the battery sample, by Coulomb counting –measurements of input or output ampere-hours [Ah]. The OCV is plotted as a function of SOC taking 100% SOC at the initial full charge state and 0% SOC at the lower cut-off voltage.

2. The other common method consists of setting the cell or battery to different SOC states, by controlled CC charge or discharge processes, and letting the voltage relax (for about 4 hours) at every desired SOC and at open-circuit conditions. The values of the voltage at the terminals after the voltage relaxation time period are taken as the OCV points at the given SOC. The voltage measurements obtained with this method are undoubtely closer to the real OCV as compared to the first method, since the values are taken after a long relaxation time. However, this method is very expensive in time, and provides only a discrete distribution of OCV values –normally, the relaxation is performed with 5 or 10% SOC intervals. Fitting the obtained relaxed OCV points with some analytical function can lead to inaccuracies in the OCV, since the multitude of physical processes which contribute to the shape of the OCV curve are not necessarily represented by the fitting functions.

Besides, and as many authors have pointed out before, Barai et al. showed in [73] that in the batteries with LFP cathode a clear path dependency of the OCV can be observed, meaning that there exist two equilibrium voltage points at every SOC: one is reached after a charge process, and the other after a discharge.

In this study, both methodologies were applied to several battery samples, and after observing that the OCV variations between different battery samples was almost zero, the results of a single cell are taken as representative for all the batteries of the same lot.

OCV Results

The OCV obtained values of the representative cell are shown in Figure 4.6.

It can be observed that the OCV curves of the battery of study are very flat among practically the whole SOC range, as it is expected in LFP-cathode cells.

Results Analysis

Analyzing the scatter OCV points obtained by the relaxation procedure (see the scatter points *OCV(6h)*, in Figure 4.6), it can be observed that, in the charge OCV,

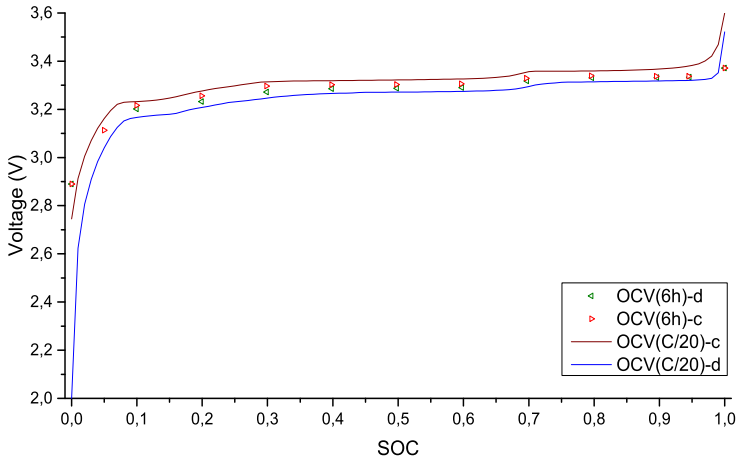

Figure 4.6: *Experimental OCV curves. The continuous lines show the pseudo-OCV curves (OCV methodology 1.) obtained at C/20-rate. The scatter points are voltage values taken after 6 hours of relaxation in open circuit conditions at different SOC (OCVmethodology 2.).*

a local minimum exists in the OCV at around 90% SOC, this meaning that the open-circuit voltage at 90% SOC is lower than the values at 80% and 100% SOC. This fact is interesting and counter-intuitive, since a higher voltage is always expected at higher SOC. For a further understanding of this behavior, the voltage relaxation phase at the different SOC stages is examined (see Figure 4.7), and the following observations are noted:

- The derivative of the voltage in time is practically zero at all the SOC after 6 hours of open circuit conditions, and no appreciable differences are found in the derivative values at different SOC.
- The magnitude of the total relaxation voltage within the 6 hours relaxation time, which is taken as the difference between the last (relaxed) voltage value and the voltage at the terminals at the instant in which the current source is shut down, is observed to be dependent on the SOC. It can be seen that:
  - In the case of the voltage relaxation after discharge processes (red curve in the right figure of Fig. 4.7), the voltage drop is approximately constant for the interval 100%-20%, but grows within the interval 0%-20%. This growth on the voltage drop can be attributed to the diffusion limitations, and the attributed charge-transfer resistance increase that is expected

when discharging at low SOC for almost all kinds of lithium-ion batteries.

– The magnitude of the open-circuit voltage relaxation after charging (black curve in the right figure of Fig. 4.7) is approximately constant for the interval 0%-80% SOC, but drops non-monotonically at around 90% SOC. This non-monotonical change in the voltage drop (linked to the flatness of the OCV curve) is pointed out as the reason for the local OCV minimum at 90% SOC to appear; it might be explained by some phase change or transition in the LFP positive electrode.

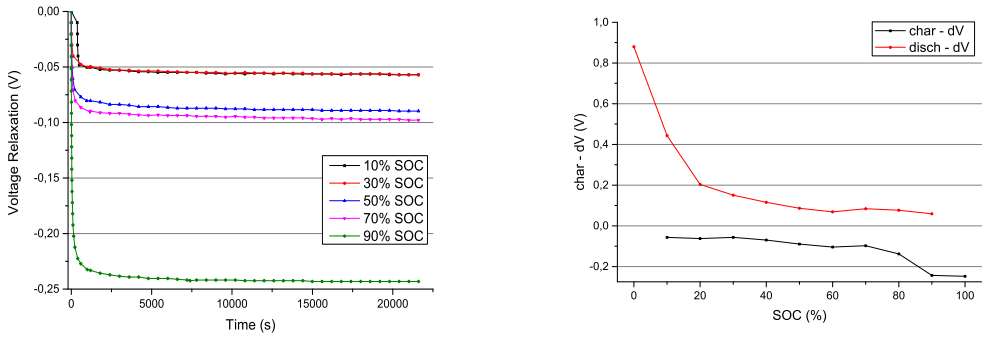

Figure 4.7: *On the left, the recorded voltage relaxation within the relaxation time at different SOC stages is shown. At the right, the total voltage relaxation is plotted at every stationary SOC point in which OCV values are taken.*

Apart from the counter-intuitive local minimum of the charge OCV at 90% SOC, the obtained OCV shows a quite big hysteresis which observable even to the naked eye in the case of the C/20-rate measurements (continuous lines in Figure 4.6). This OCV path dependency means that for a given SOC, temperature, and pressure, many equilibrium potentials may exist, and it is well known to be present in LFP-anode batteries, as well as for batteries with a nickel hydroxide cathode ([113, 114]). Barai et al. showed in [73] that the OCV is (current) rate independent, and proposed a methodology for characterizing the hysteresis.

A further investigation on the battery hysteresis is kept out of the scope of the work, but since noticeable differences are observed between the pseudo-OCV curves and the relaxation method voltage points, and since the accuracy of the OCV curve is important in the battery model implementation, it has been decided to use the best characteristics of both characterization techniques.

Therefore, a fitting method is implemented in Octave to interpolate the C/20-rate pseudo-OCV curve to fit the stationary points after voltage relaxation. The

result (shown, for charge processes, in Figure 4.8) is a curve that matches all the stationary scatter points, which are more reliable and accurate OCV points, and maintains the shape of the continuous pseudo-OCV curve. Thus, the accused local voltage gradients ($\partial U_{oc}/\partial SOC$), which are known to be related to material phase transitions, as explained in [115], are maintained within the final OCV fit.

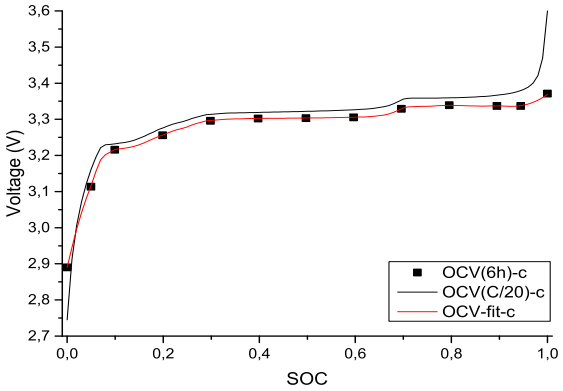

Figure 4.8: *Obtained charge OCV curve with the mixed-fitting technique that matches the experimental voltage relaxed values maintaining the pseudo-OCV curve shape.*

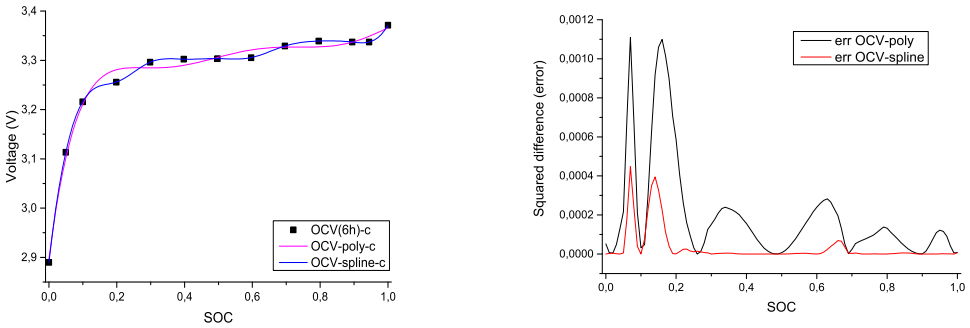

Figure 4.9: *Left, charge OCV obtained by using different polynomial fitting techniques to the points of the voltage relaxation method. Right, square difference of the polynomial fitting techniques compared to the applied mixed-fitting technique shown in Figure 4.8.*

In order to compare the selected OCV fitting technique to the common polynomial fitting functions that are used in other studies, I have compared our result with other function fitting techniques. A 6th order polynomial fit (labelled *OCV-poly* in

Figure 4.9) and a piecewise cubic spline fit (labelled *OCV-spline in Figure 4.9*) have been fitted to the stationary OCV points.

It is clear that the shape of the fitted curves is completely different than the one obtained with the selected fitting technique, and it is concluded that conventional polynomial fitting of the scattered OCV points can lead to appreciable OCV mismatches.

4.2.3 Overpotential Characterization

Once the equilibrium voltage (OCV, or U_{oc}) of the cell has been characterized, the overpotential of the battery can be studied through the observation of the operating voltage, U_{exp}, under different operating conditions.

In the present work, and as detailed and justified in the following section 5.1, the load case that is aimed to be modelled and studied is restricted to the fast charging processes. With this in mind, and owing to the fact that the transient battery behavior does not have a big impact or influence in the overall galvanostatic process during a full fast charge, the experimental characterization of the battery overpotential has been conducted, in accordance, for continuous charging and discharging processes.

Other common characterization techniques, which give a deeper insight on the transient behavior of the lithium-ion battery, such as pulse tests and EIS measurements (recall section 3.1.1), have also been conducted. Nonetheless, the results and the analysis of such are not included in this thesis.

Experimental Matrix

The operating battery voltage, $U = U_p - U_n$, depends strongly on the SOC, the ambient temperature, and the galvanostatic regime (applied current rate), at any time. For that reason, full charge processes are experimentally tested at different temperatures and different current rates. The matrix of the experimental characterization is set to the discrete study of full battery cycles[2] under the following parameter values:

- Galvanostatic currents: C/3, C/2, 1C, 1.5C, and 2C
- Operating temperatures: 0°C, 20°C, and 40°C

[2]Full cycles refer to cycles between the minimum and maximum cut-off voltages.

Test Procedure

The experimental test consists of a preliminary CCCV charge at 0,3C-rate. Once the CV charge is stopped, the current battery state is taken as fully-charged or, in other words, the capacity of the battery at this stage is associated to 100% SOC.

After this preconditioning step, necessary for the repeatability and validity of the following test procedures, a set of CC discharge and, subsequently, CCCV charge processes are performed. The number of cycles corresponds to the number of current magnitudes that are characterized, and a single cycle is performed for every current magnitude value (from lower to higher C-rates).

In discharge processes, the limit voltage is set to the minimum cut-off voltage, in this case 2V, while in the charge process, the CC phase is limited to the maximum cut-off voltage, $3,6$V. CV phase is only performed at the maximum cut-off voltage during charge, and is stopped when the current has dropped below 10% of the charging current during the CC process.

Obtained Voltage Curves

Since the experimental test matrix is quite wide, only some relevant results are considered to be graphically appended.

In Figure 4.10, the experimental operating battery voltage curves at different current rates for an ambient (climate chamber) temperature of 20°C are shown. It can be observed that increasing current rate translates into higher values of overpotential (that is, higher operating potential in charge processes, and lower operating potential in discharge regimes).

In Figure 4.11 the charge voltage curves, at 1C-rate and different temperatures are shown. Note that, as expected, the lower the operating temperature is, the higher the operating battery voltage. As a consequence of the higher operation voltages, the upper cut-off voltage ($3,6$V) is achieved at a lower SOC level, which is translated into a longer CV charging phase.

Regarding the operating battery temperature, which is tracked by the temperature sensor that is attached to the surface of the battery under characterization (as explained in the previous section 4.2.1), we can see in Figure 4.12 that the battery temperature increase, during the galvanostatic full cycles, becomes higher as the current rate increases.

These temperatures shown are hardly useful, in a quantitative way, for studying or determining the heat generation rates of the battery with precision, since the cooling power which is supplied by air convection inside the testing climate chamber

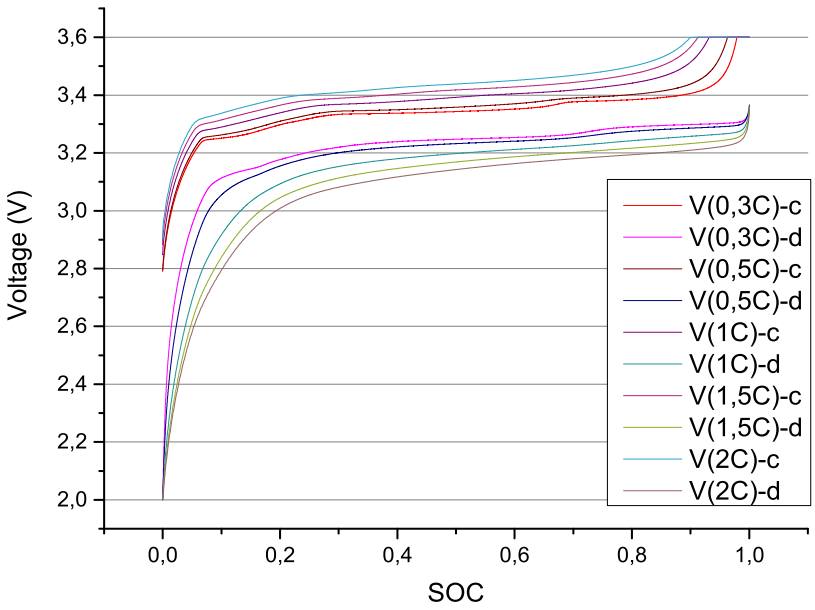

Figure 4.10: *Experimental voltage curves obtained at 20° C and different current rates.*

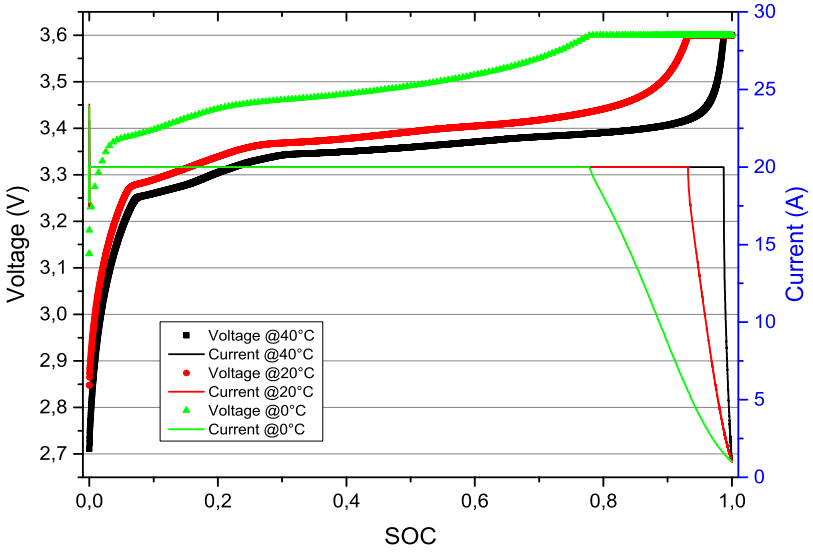

Figure 4.11: *Experimental voltage and current curves plotted against the battery SOC undergoing 1C full charge at different ambient temperatures.*

is unknown, and not constant. Nevertheless, the measured temperatures can give a qualitative insight on the thermal performance of the batteries.

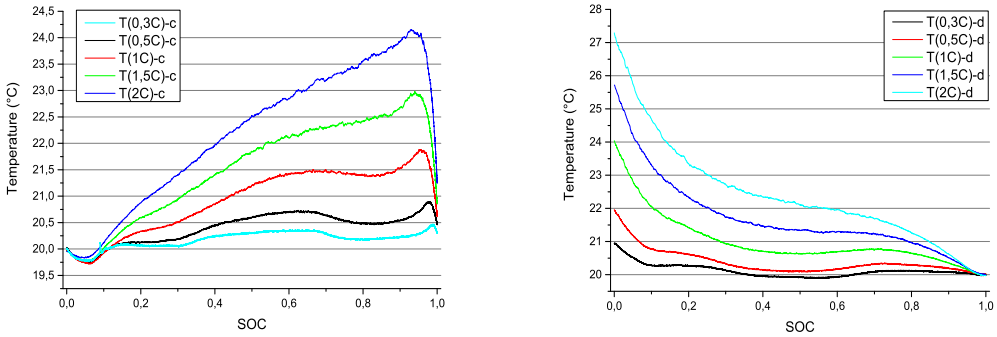

Figure 4.12: *Temperature sensor measurements during cycling at a 20° C climate chamber. Left, during CCCV charge processes. Right, for CC discharge phases.*

In the left part in Figure 4.12, we can see that all charge processes are endothermic at SOC lower than 10%, which has to be necessarily explained by the reversible or entropic effects. Besides, it is observable that at low currents, the temperature evolution resembles the shape of the entropic coefficient, $\partial U_{oc}/\partial T$ (shown in the next Figure 4.26), whereas at higher currents the temperature increase is more linear, due to the increase of the influence of the irreversible heat sources, that grow faster than the reversible contributions when the current increases (recall equation 3.4).

Analysis of the Results

By completing a further analysis of the obtained data, it can be observed that during continuous charge or discharge processes, the dependency of the operating battery voltage on the current rate is approximately linear at any SOC, as shown in Figure 4.13. At increased DOD –this meaning high SOC during charge, and low SOC states during discharge–, the linear fit of the voltage against current experimental points, shown in Figure 4.13, seems to be less accurate. Nonetheless, an analysis of the performed fitting, performed in origin, shows that the coefficient of determination, R^2 of the linear fitting is higher than $0,95$ for the whole SOC range.

The relationship between the operating voltage and the decreasing temperature shows a non-linear correspondence, which causes the voltage to grow faster as the temperature keeps decreasing. In this figure, this trend is shown at 10%SOC and under currents, however, the trend is observed to be similar for all other SOC during

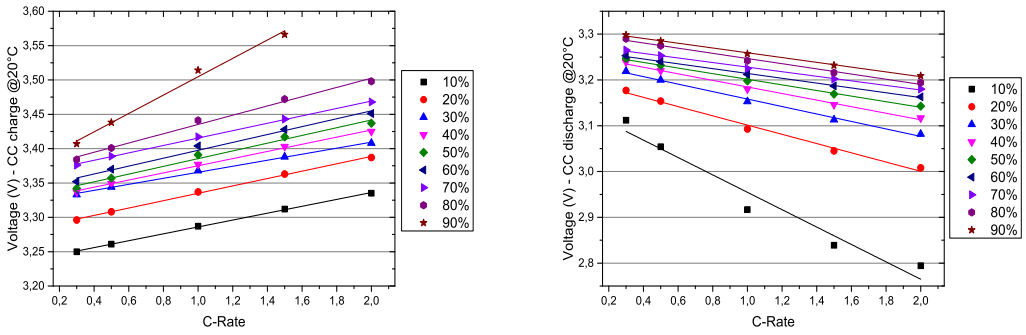

Figure 4.13: *Linear fitting of the battery polarization (voltage versus current) curves, during CC charge (left) and discharge (right) processes, at different SOC stages. All the results pertain to tests at 20° C.*

charge and also during discharge processes.

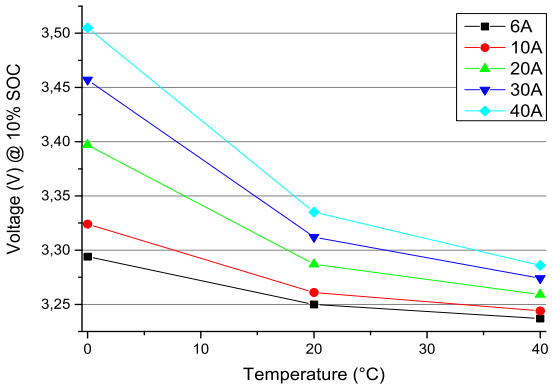

Figure 4.14: *Experimental charge capacities using the same standard CCCV charge procedure at different operating temperatures.*

At last, a similar analysis is adopted to observe how the battery temperature increase evolves. As shown in Figure 4.15, the total temperature increase of the cells (after the tested deep CCCV charge, or CC discharge) grows linearly with increasing currents. Besides, it can be observed for the present battery that full discharge processes conduct to approximately two times greater temperature increase as compared to the temperature increase of deep charging processes.

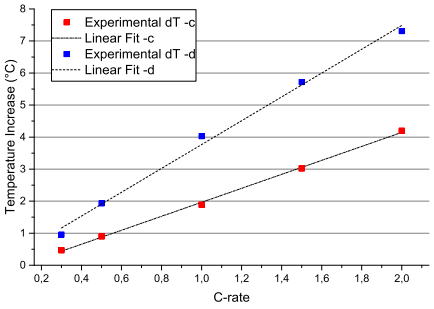

Figure 4.15: *Values of the obtained maximum temperature increase during CCCV charge and CC discharge at 20° C.*

Effects on the battery capacity

As mentioned in section 2.1.1, the charge and the discharge capacity of a battery is subject to the operating conditions.

From the present characterization test results, the influence of the temperature and the current rates in the charged and discharged battery capacity can be observed. In agreement with the manufacturer specifications and as shown in Figure 4.16, the lower temperature the lower the charge capacity of the battery (an analogous figure for the discharge capacities has not been included here because the behavior was exactly identical as in the charging processes.

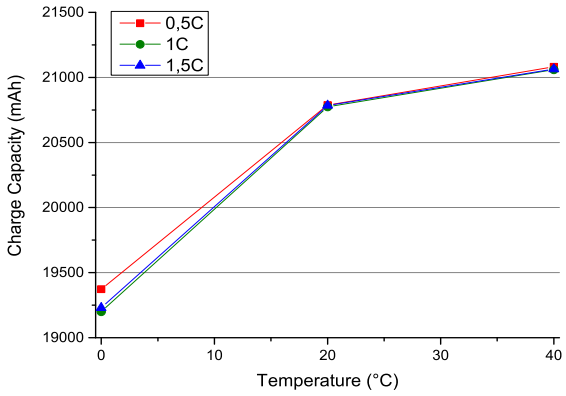

Figure 4.16: *Experimental charge capacities using the same standard CCCV charge procedure at different operating temperatures.*

It can also be observed that at moderate or hot temperatures (20-40°C) the current rate has no appreciable influence on the charge capacity, whereas at low

temperatures, the charging capacity is clearly higher when low current rates are applied. However, and conversely to what is argued in the literature (detailed in section 2.3.1), the charge and discharge capacities do not show a significant difference in our experiments. This points out that lithium plating does not have a severe influence in the tested battery at 0°C, at least not in the fresh state in which the battery was characterized.

4.3 Thermal characterization

There exist mainly two families of instruments that are actually employed for the characterization of the thermal behavior of batteries: accelerated rate calorimeters (ARC) and isothermal heat conduction calorimeters (IHC) [27].

ARC instruments attempt to provide adiabatic conditions to the battery under testing, by the use of some heating and cooling elements that ensure that the temperature of the sample envelope is very similar to that of the test sample at any time. The battery heat generation is estimated then, indirectly, through the recorded temperature evolution, since in adiabatic conditions the thermal energy balance reads:

$$\dot{q} = mC_p \frac{dT}{dt} \tag{4.1}$$

On the other hand, in IHC tests the battery is placed inside a chamber which is submerged and in direct contact with a huge amount of a surrounding thermal bath. The temperature of the thermal bath is maintained constant by the use of any heating and cooling elements, and normally stirring motors are included for improving temperature homogeneity by the bath liquid convection. When the battery is therein operated, a heat flux is established from the inside of the chamber to the isothermal bath, and high precision thermoelectric heat flux gauges, embedded in the chamber walls, measure directly the heat flux magnitude.

Note that IHC is a much better choice if the effects of the temperature on the heat generation rate want to be precisely determined, since, while in ARC measurements the temperature increases considerably during experimentation (to ensure adiabatic conditions), in IHC the test chamber temperature is almost maintained constant during all the test procedure. Another advantage of IHC is that the heat capacity of the battery does not need to be estimated. Conversely, the heat flux is measured explicitly.

For that reason, an IHC instrument that was recently installed in the laboratory

facilities of FhG-ISE[3] is employed in this work to characterize the battery thermal behavior. Besides, in the context of this work, in which an electrochemical-thermal model is developed for the battery under study, the results of the calorimetric measurements will be used, as well, as a model validation tool (in chapter 6).

4.3.1 Experimental Setup

Calorimeter Specifications

The IHC calorimeter that is employed is the Netzsch IBC284, was developed in collaboration with the National Renewable Energy Laboratory (NREL). It consists of a large volume analysis chamber submerged in an isothermal bath of a 50/50 mixture of glycol and deionized water that permits the reach of lower temperatures without freezing.

The instrument offers the possibility to characterize the efficiency of batteries over different temperature ranges and states of charge with a high accuracy, thanks to a very stable bath temperature control of $\pm 0,01°C$, and with a high heat flux sensitivity detection of 30mW.

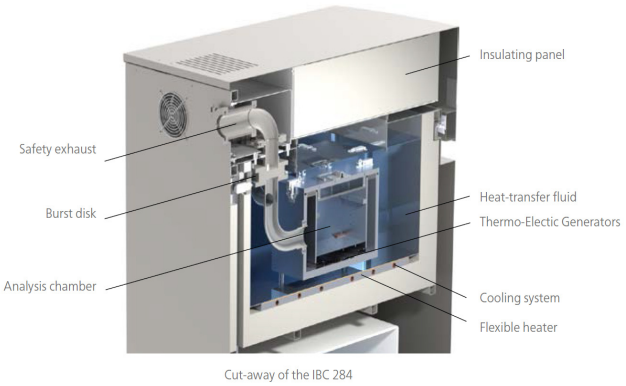

Figure 4.17: *Cut-away of the isothermal calorimeter. Image from Netzsch User's manual.*

The temperature control of the thermal bath consists of a cooling plate, placed underneath the thermal fluid bath, and a silicone/rubber heating element, the power delivery of which is controlled by an internal PID controller. The temperature of the bath is homogenized by convection with the use of some stirring motors that constantly mix the thermal bath.

The calorimeter has four different measurement modules:

[3]Fraunhofer-Institut für Solare Energiesysteme (ISE)

1. First, and most important, a measurement module for the heat flux, consisting of 60 high sensitive heat flux gauges that measure the heat flow from the inner box to the bath. The heat flux gauges are type K thermocouples. They can measure from 100mW to 50W of heat, and the final enthalpy measurements (or dissipated heat energy in a period of time), are ensured to have an accuracy of $\pm 2\%$.

2. Voltage and temperature measurement sensors are incorporated inside the experimental chamber to track the voltage of different batteries (a total of four sensors, in case of testing more than one battery at a time), and/or to track the temperature at different spots within the chamber. The accuracy of the data acquisition is of 1mV for the voltage, and of $0,1$K for the temperature measurements. Furthermore, an additional voltage sensor tracks the voltage at the busbar. This serves to distinguish the electrical power that enters the chamber (or system), and the power that is introduced on the samples, which eventually differ due to the contact resistance of the electrical power connections from the busbar to the battery.

3. The external input or output current is measured through the potential drop in a shunt resistor. The maximum allowed current is 300A and the sensor resolution is of 5mA.

4. At last, a temperature measurement module, consisting of two separate probes with a readability of $0,01$K and reproducibility of $0,1$K, is used to track and control the bath temperature.

Calorimeter and Battery Tester Setup

The main external connections to the calorimeter are:

1. A computer system is connected by two USB ports, for data acquisition and for regulation of the temperature control.

2. Two gas network connections are needed: inert gas (Nitrogen or Argon) for the calorimeter chamber, and compressed air for level management of the liquid within the calorimeter bath.

3. A commercial battery tester to be employed to control the charge and discharge of the battery or pack is connected by an Anderson SB175 port.

4. The exhaust of the IBC must be connected to an evacuation vent duct. The gases of the calorimeter inner chamber will be evacuated when the pressure exceeds 5psi.

The battery cycler that is employed for the tests is the Digatron MCT 300-05-3 ME, with a maximum current of 300A and a voltage range of 0 to 5V. It is connected to the power input plug connection of the IHC calorimeter to conduct the experimental procedures within the calorimeter chamber. A scheme of the setting of the instruments is shown in Figure 4.18.

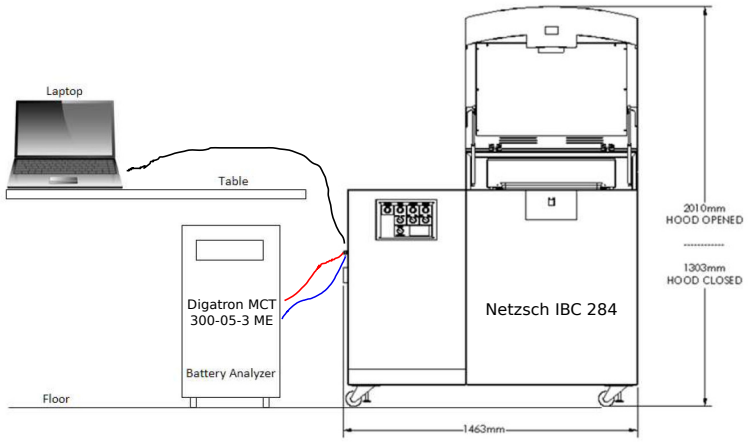

Figure 4.18: *Scheme of the experimental setting for the isothermal calorimetry measurements. Adapted image from the IBC284 user's manual.*

As usual, the Digatron cycler control precision is given in the data sheet as a function of the working point. If the set-point is comprised within 0-10% of the maximum voltage/current, the precision is of $\pm 0,5\%$ of the working point, whereas for higher power working states, the precision is given as $\pm 0,05\%$.

Cell Setup

The cell is located on the surface of the analysis chamber of the IBC284, as we can see in Figure 4.19. The connection of the battery to the copper busbaris set with thick cables of $\varnothing = 8mm$ and some copper clamps to ensure a good electrical conductivity (thus, lowering ohmic losses) between the battery current collectors and the electrical power input busbar.

A voltage sensor is placed on the current collectors, and four temperature sensors are placed at different locations on the upper battery surface, to gather possible information on battery surface temperature gradients.

Figure 4.19: *Picture of the cell setup inside the IBC analysis chamber.*

Test Matrix

The objective of the IHC measurements is to give the maximum information on the thermal characteristics of the battery. This includes the thermal properties of the battery (the heat capacity, C_p, and the thermal conductivity, κ), but, most importantly, the battery heat generation rate, $\dot{q}$, under different operating conditions.

In isothermal calorimetry measurements, the heat flux measurements at a fixed time are not quantitatively relevant, but only the integration of the total measured heat flux in a period of time (corresponding to the total released thermal energy), that starts and ends up in equilibrium conditions, should be taken into account as a quantitative value.

Equilibrium conditions are defined for such an instrument as a constant bath temperature and a stable heat flux with an approximately zero baseline. These conditions ensure that the complete system, (both inside the experimental chamber and within the surroundings) is in isothermal conditions.

Before starting any experimentation, isothermal equilibrium is a required condition, and after any test measurement, equilibrium has to be reached again in order to neglect the temporal derivatives in the thermal energy balance:

$$\rho C_p \frac{\partial T}{\partial t} + \nabla \cdot q = \dot{q} \tag{4.2}$$

This implies that the battery heat generation can not be characterized at concrete SOC levels. Conversely, the released thermal energy during a current pulse test has to be attributed to the average SOC of such period.

Moreover, and for the previous reason, IHC calorimetric measurements require long periods of relaxation time. Based on previous experiences, the relaxation time

to reach equilibrium after a heat generation pulse (of course depending on the magnitude of the generated heat) is foreseen to last for about 6 hours. Logically, this constrains the amount of test measurements that can be conducted.

The matrix of experimental measurements to characterize the relevant thermal aspects of the sample under study is, therefore, decided to consist of:

- A heat capacity measurement (repeated three times) is going to be conducted to estimate the heat capacity of the battery sample.
- Battery heat generation rates, with a resolution of 10% SOC current pulse intervals, under different temperatures and current rates. Precisely, the thermal investigation under a 1C current rate will be conducted at 0°C, 20°C, and 40°C; and 2C will be conducted at 20°C.

The heat conductivity of the cell is kept out of the measurements matrix, since the experimental setup for such measurements (which ought to be based on some standard procedures for heat conductivity measurements, such as the ASTM-C177 or ISO8302[4]) cannot be easily set with this kind of instrument.

4.3.2 Battery Heat Generation Rate

Theoretical Basics

The temporal integration of the thermal energy balance (equation 4.2), taking an interval of time in which both the initial and the final time, t_1 and t_2, are in equilibrium conditions, allows to rewrite

$$\int_{t_1}^{t_2} \rho C_p \frac{\partial T}{\partial t} dt = 0 \quad \rightarrow \quad \int_{t_1}^{t_2} \nabla \cdot q dt = \int_{t_1}^{t_2} \dot{q} dt \tag{4.3}$$

since, by the definition of the equilibrium isothermal conditions, $T(t_1) = T(t_2)$.

Hence, the temporal integration of the directly measured heat flux, corresponding to the term $\nabla \cdot q$, provides the desired information: the energy (in J) that the battery has dissipated in the period (t_1, t_2).

Just as an illustrative example, the typical output that is measured in the calorimeter when current pulses are applied to a battery sample is shown in Figure 4.20.

[4]ASTM-C177 (american standard) and ISO8302 (European standard) establish very similar procedures for heat conductivity measurements.

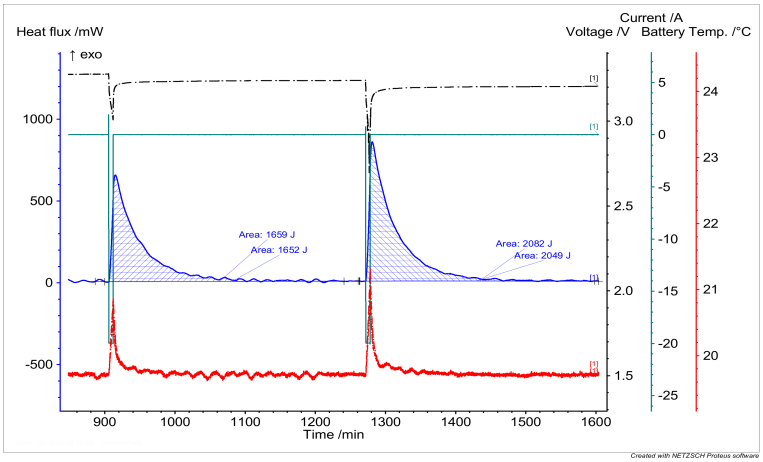

Figure 4.20: *Plot of the obtained voltage, current, temperature, and heat flux when testing a battery under 10% SOC discharge current pulses. Image obtained from Proteus.*

Test Procedure

By experience, it has been observed that after a heat generation pulse, and of course depending on the magnitude of the heat generation within the calorimeter chamber, the gauges that measure the heat flux require approximately four to six hours to reach equilibrium again. Therefore, after any current is applied to the battery from the battery tester, a pause of six hours is scheduled.

The test procedure, that is programmed for the Digatron battery cycler, comprises:

1. First, a preconditioning CCCV discharge to achieve 0%SOC. This step is needed for the repeatability and consistency of the test, since the SOC of the battery is not necessarily known before starting the test.

2. Subsequently, a full CCCV charge is performed, with a cut-off maximum voltage of $3,6$V, and the capacity value is set to 100%SOC.

3. Afterwards, a set of 10% SOC CC discharge pulses at 1C (and/or 2C), are scheduled. For the last pulse, and in order to reach the fully-charged state, a CV phase is performed too.

4. Similarly, ten 10% SOC CC charge pulses follow the test.

5. Finally, a full CCCV discharge is performed, from 100 to 0% SOC, with a minimum cut-off voltage of 2V.

Results

The obtained results were initially analysed with the data analysis software *Proteus*, which includes a set of tools for a functional evaluation of the recorded data.

However, for convenience and with the aim of saving time, a Python script has been developed for the automatic evaluation of the measurement data. Apart from being more time efficient, the automated data evaluation is more consistent, since it averages the heat energy values for every current pulse phase, by recursively iterating within the heat power energy of every pulse by using different (random dependent) time intervals. This way, the errors that could arise by the improper selection of the time integration interval, which was done manually in *Proteus* software, are minimized.

The results for the battery heat dissipation power in all the conducted experiments are shown in the following Figures 4.21 and 4.22.

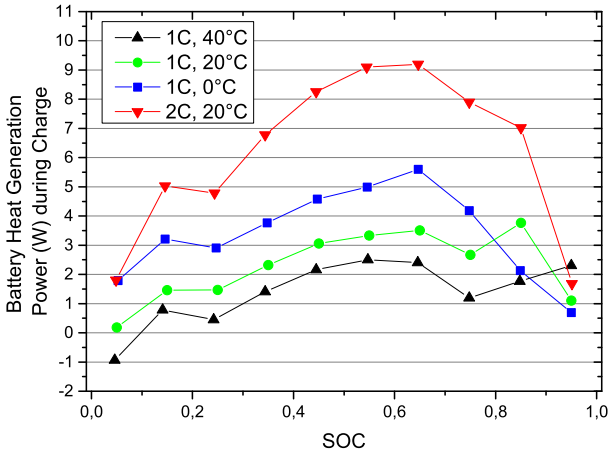

Figure 4.21: *Average heat dissipation power rate obtained by the calorimeter using 10% SOC charging current pulses.*

Note that the heat generation rates are clearly path dependent: under all the tested conditions, the maximum discharging heating power is higher than the charging one.

Besides, we can observe that, as expected, the battery heat generation rate increases as the temperature gets reduced and as the current magnitude grows.

From the obtained data, the energy efficiency of the battery is computed as

$$\eta_{bat} = \left(1 - \frac{P_h}{P_e}\right).100 \tag{4.4}$$

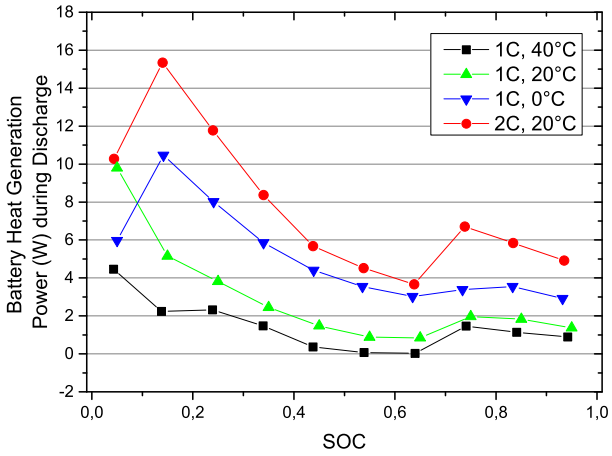

Figure 4.22: *Average heat dissipation power rate obtained by the calorimeter using 10% DOD discharging current pulses.*

where P_e is the electrical power going in or out the battery, and P_h is the heating power that the battery dissipates; the obtained results are shown in Table 4.3.

Table 4.3: *Average of the battery energy efficiency under the different tested conditions.*

Test	1C, 0C	1C, 20C	1C, 40C	2C, 20C
Efficiency	91,52%	93,55%	97,59%	95,42%

4.3.3 Battery Heat Capacity

Theoretical Basis

When integrating within a temporal interval (t'_1, t'_2) and assuming that the battery temperature at t'_1 is different than the one at t'_2, the first term of the energy balance (equation 4.2) can be approximated as:

$$\int_{t'_1}^{t'_2} mC_p \frac{\partial T}{\partial t} dt = mC_p. \left(T(t'_2) - T(t'_1)\right) \tag{4.5}$$

Thus, the heat flux gauges from the calorimeter can be used (which explicitly measure the heat flux conducted from the analysis chamber to the surrounding thermal bath, $\nabla \cdot q$) to estimate the heat capacity of the battery.

To do so, the sample needs to be introduce at a higher temperature than the

one of the isothermal bath and ensure that $\dot{q} = 0$ is zero within the interval (t'_1, t'_2).

Experimental procedure

The calorimeter bath level is set to a lower level, so that the analysis chamber can be opened without necessarily draining any liquid.

The battery is heated up to $40°C$, in an external climate chamber, while the isothermal bath setpoint is fixed to $20°C$. Once the calorimeter reaches isothermal equilibrium conditions, the chamber is rapidly opened and closed again, placing quickly, in between, the hot battery inside the calorimeter analysis chamber.

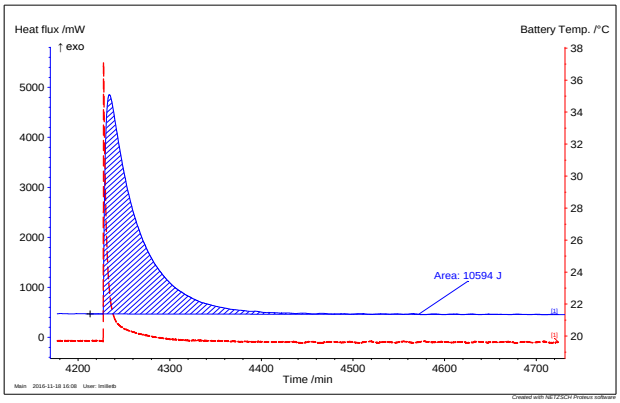

Figure 4.23: *Plot of the registered heat flux and battery temperature sensors in the heat capacity calorimetric measurements.*

The output obtained for one of the conducted measurements, from *Proteus* software, is included in Figure 4.23.

Results

The experimental procedure has been checked by measuring the heat capacity of known substances: a cup of water and paper, and the procedure has shown, after 3 repetitions, an accuracy of $\pm 5\%$.

The estimated battery heat capacity is, obtained as the average heat capacity of three measurements using the exact same procedure described above:

$$C_{p,bat} = 1230 \mathrm{J\,kg^{-1}\,K^{-1}} \tag{4.6}$$

The results are reasonable as compared to those that were recently reported by Lai et al. [89], and by Vertiz et al. [83].

4.3.4 Entropic Coefficient Estimation

Analysing the empirical data from the battery heat generation rates, and by the use of the heat generation equation derived by Bernardi et al. (equation 3.4), the reversible and the irreversible heat contributions can be distinguished, or approximated, from the total measured heat.

With this in mind, and by the post-process analysis of the obtained dissipated heat areas and the voltage and current curves, the entropic coefficient value can be estimated for every test pulse as:

$$\frac{\partial U_{oc}}{\partial T} = \frac{\int_{t_1}^{t_2} \dot{q}_{bat} dt - \int_{t_1}^{t_2} I_{exp}.(U_{exp} - U_{oc})}{I_{exp}.T} \tag{4.7}$$

In Figure 4.24, the obtained irreversible and reversible heat contributions are shown for the 1C experiment at 20°C, the estimation of the battery entropic coefficient by the use of this method is shown in Figure 4.25.

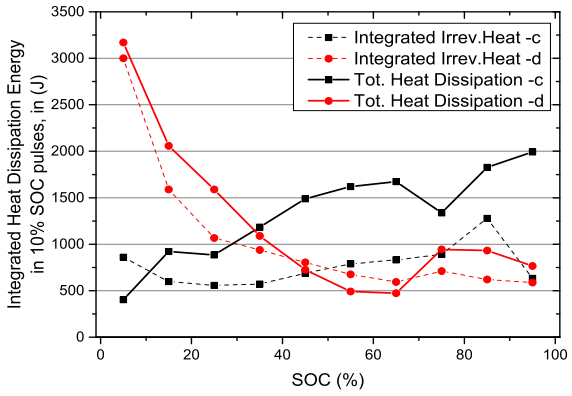

Figure 4.24: *Plot of the reversible and irreversible heat contribution estimations, that are obtained by the processment of the obtained calorimetric data for the 1C, 20° C test.*

The most common and precise method to obtain the entropic coefficient factor, $\partial U_{oc}/\partial T$, is the so-called potentiometric method, which consists in the direct measurement of the battery OCV under different temperatures, at a fixed SOC ([116, 117]).

Taking advantage of the fact that a high-precision hardware setup was designed and built at our institute by Hukan in [118], the entropic coefficient estimations obtained in this work have been compared with the ones that the high fidelity setup can provide. Hukan characterized the entropic coefficient for the same cell that is

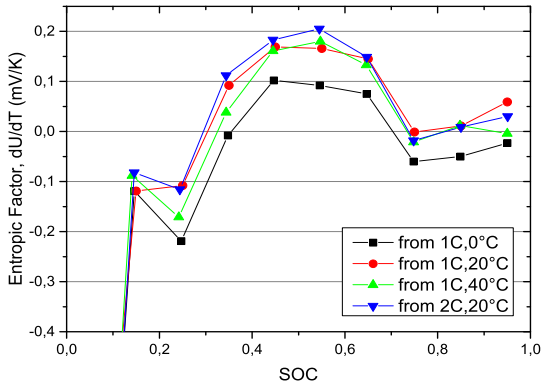

Figure 4.25: *Plot of the estimated entropic coefficient, $\partial U_{oc}/\partial T$, by the data processment of the calorimetry heat rate measurements.*

studied in the present work, and his results are shown in Figure 4.26).

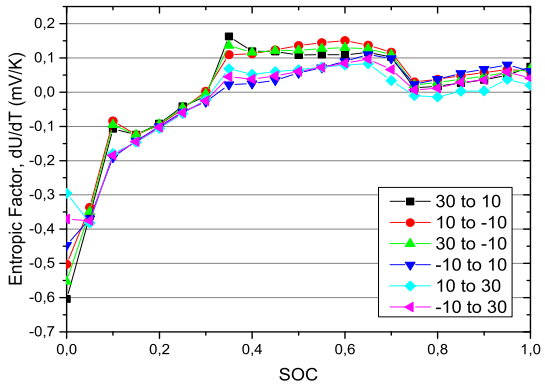

Figure 4.26: *Plot of the measured entropic coefficient, $\partial U_{oc}/\partial T$, by the so-called potentiometric method. Results from [118].*

A deep analysis on the comparison of both methodologies is not included here. It was concluded that, althought the method based on calorimetric measurements shows a good estimation of the entropic coefficient and can obtain the entropic coefficient estimations in much less time than the potentiometric-based method, the results obtained by Hukan are more consistent and precise.

Chapter 5

Battery Model Implementation

In this chapter, the implementation of the simulation model for the electrochemical and thermal behavior of the pouch battery of study is explained.

In section 5.1, the modeling strategy or formulation framework is determined. Choosing from the different SoA simulation approaches reviewed and presented in chapter 3, the decision of the simulation strategy is based on the precise objectives of the simulation and the limitations that exist for the development of this work.

Section 5.2 gathers the model implementation, including the dimensions and domains definitions, the material properties, and the formulation of the governing equations.

5.1 Modeling Strategy

5.1.1 Objectives

The development of the present work is contextualized within the JOSPEL project, a European Union (EU) research project under Horizon 2020 call, the main aim of which is the development of novel energy efficient climate systems for the optimization of interior temperature control management in electrical vehicles.

More concretely, and as stated in the definition of the project objectives, the application and combination of Joule and thermoelectric elements is sought to be studied in order to design and improve the existing thermal conditioning systems, both for passenger comfort and for the battery pack thermal conditioning. In this context, the present model implementation arises to serve as a development tool for the design and optimization of the BTMS system, with the objective to enhance the battery life as a side effect of an optimized thermal management.

In order to study and optimize the thermal performance of the battery pack,

a wide variety of load cases and ambient conditions can be analysed or studied. However, one of the major thermal demands in the EVs battery packs is a load case that can be simply described: the fast charging process. Since the heat generation rate grows with increasing current in an approximately exponential fashion, it can be deducted that fast charging can be one of the most demanding conditions regarding the thermal performance of the battery pack.

In the present project context, a fast charge current of 1C is sought (that is, charging the complete car battery in one hour). Therefore, and after analysing a real driving profile obtained in a previous project with the Stromos EV (see Figures 5.1 and 5.2), fast charging is set in this work as the priority load case.

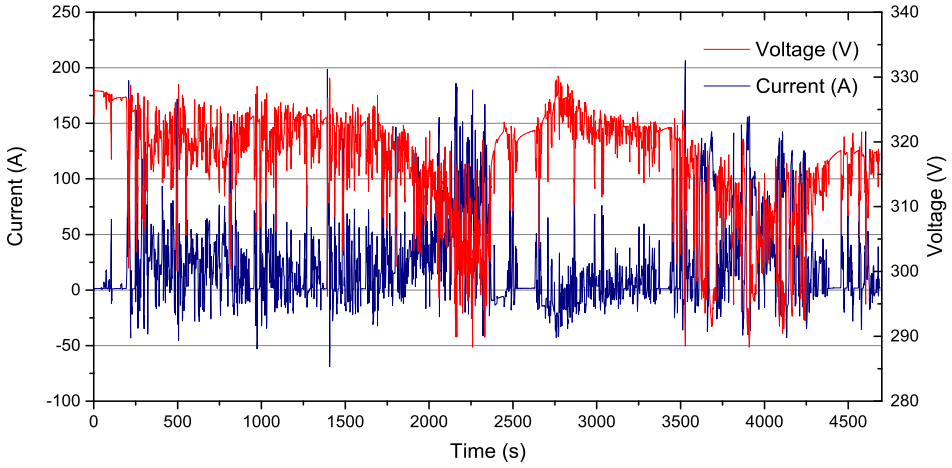

Figure 5.1: *Battery voltage and current driving profile, recorded during a mixed trail with the Stromos EV.*

The driving profile was recorded in a mixed trail (city, mountain, and highway drive) from Mannheim to Heidelberg, and after analysing the data, it was observed that high magnitude current rate demands appeared in a very low frequency, and lasted for very short time-periods (see Figure 5.2) [112].

5.1.2 Limitations

The selection of the modeling strategy for the electrochemical and thermal performance of the battery has to be consequent both with the testing tools that are available for the execution of the present work and with the modeling objectives described above.

On one hand, the experimental testing tools that are available are limited. For

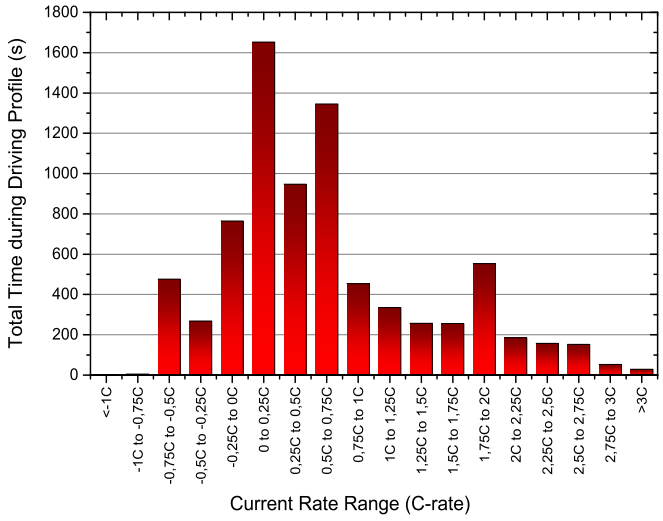

Figure 5.2: *Duration of the total sum of battery current rates recorded from a driving profile with the Stromos EV. The battery charging process is not included, and negative C-rates appear because of regenerative breaking.*

example, an internal inspection of the inner battery active materials is not feasible, and as shown in the previous section 4.2, the characterization is restricted to electrical battery cycling and calorimetry tests.

On the other hand, the objective of the simulation of the BTMS poses a considerable limitation in terms of the model computational cost, since many batteries have to be solved at a time within a thermal model and the geometrical configuration has to be optimized (which involves irredeemably the recursive computation of the simulation model several times). Besides, and due to the software license limitations, the computational power in this work is limited and restricted to a single CPU.

5.1.3 Modeling Strategy Determination

With both the modeling objectives and the technical limitations in mind, and recalling the overview given in the previous section 3.2.2 (in which different electrochemical-thermal simulation strategies for lithium-ion batteries were reviewed) the final modeling strategy is selected. Following the conclusions suggested by Allu et al. in [119], who compared the two major electrochemical modelling approaches (empirical and physics-based) for the thermal modeling of lithium-ion battery packs, an equivalent-

circuit based model has been chosen to account for the electrochemical phenomena.

The adopted modeling strategy is based on some recent publications. More precisely, on the works of Gu and Wang [120], Kim et al. [29, 121], Kwon et al. [109], Taheri [30], and Yazdanpour [28], and the strongest point of such an approach is that it combines the simplicity and speed of the EC representation of the electrochemical processes with the main complexities and spatial singularities of the large size pouch cells phenomena.

5.2 Cell Model Implementation

5.2.1 Outline

Cell Domain

The A123 AMP20*m1*HD-A battery, as any other pouch battery, is conformed by a certain number of electrochemical cells connected in parallel. Although the exact internal structure has not been observed, neither any battery sample has been internally examined in this work, the internal disposition of the elements conforming each electrochemical cell is composed in most of the pouch batteries as shown in Figure 5.3.

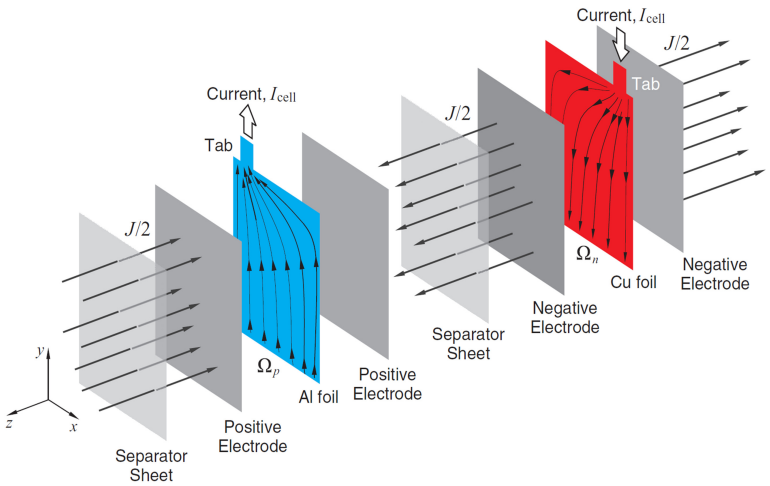

Figure 5.3: *Scheme of the internal assembly of the electrochemical cells, the stack of which conforms the core of a lithium-ion pouch battery. The arrows from negative to positive electrodes represent the lithium ionic transport, and the arrows within the x-y plane (in each current collector) represent the electrical current streamlines during a discharge process. Figure reprinted from [30].*

As it can be observed in the previous figure, and by the internal symmetrical

structure of the battery, the domain of the simulation can be restricted to a single electrochemical cell, including a single pair of electrodes, one electrolyte and separator layer, and considering half of the thickness of each current collector (as they are double-sided).

Since no battery has been internally examined in this thesis, the thickness of each cell material layer is taken from the measurements performed in [83] by Vertiz et al., in which a 14Ah $LiFePO_4$/graphite pouch battery was studied and characterized using different existing electrical and thermal analysis procedures. The adopted thicknesses of each material layer are specified in the following Table 5.1.

Table 5.1: *Thickness of the LFP cell active materials that are adopted within the model implementation. The presented values were measured in [83].*

positive electrode	z_p	$98\mu m$
pos. current collector	$z_{cc,p}$	$20\mu m$
electrolyte/separator	z_s	$25\mu m$
negative electrode	z_n	$67\mu m$
neg. current collector	$z_{cc,n}$	$13\mu m$

Note that adopting the cell material thicknesses depicted above, and recalling that the battery and pouch film thicknesses was measured (Table 4.1), it is possible to estimate the number of electrochemical cells that are packed within a A123 AMP20*m1*HD-A pouch battery, N, by

$$N = \frac{z_{bat} - 2z_{pouch}}{z_p + z_{cc,p}/2 + z_s + z_n + z_{cc,n}/2} = 31,48 \tag{5.1}$$

Model Couplings

The model, implemented in finite elements in Comsol Multiphysics (version 5.0), couples and solves for three different governing conservation equations:

i. A first order ODE governs the state of charge (SOC) as a local quantity among the electrochemical cell surface. The local current density (from the electrical charge conservation model) influences every region SOC locally.

ii. Electrical charge conservation is employed for modeling the electrical current, potential distribution and ohmic heating source within the positive and the negative current collector domains. The electrochemical activity is accounted in this model as an electrical current generation source, applied in the whole cell domain and governed by a simple EC model.

iii. Thermal energy conservation governs the heat distribution in the whole battery domain, given different magnitude heat sources among the surface of the cell and given some lumped thermal properties of the aggregate cell material properties.

On top, an empirically-based electrochemical model interacts with all the above mentioned conservation equations through some boundary conditions (explained in detail in the next section 5.2.2).

Dimensional Simplifications

Due to the high conductivity of the aluminium and copper current collectors in comparison to the electrode materials, it can be considered that the surface distribution of the electrochemical reactions is driven solely by the current collectors voltage differences (in the x-y plane), and therefore, the Li^+ transport is considered to be held only in the z-axis direction during charge and discharge processes, as it has been presented in the literature [30]. Observe that this assumption was also intrinsically adopted in Figure 5.3.

Adding up to this ionic transport simplification, there are three other main reasons that make the dimensional simplification to a 2D representation for the cell model reasonable, namely:

- First, the aspect ratio of the electrochemical cell is considerably big, since the surface of the cell is several orders of magnitude bigger than its thickness.
- In the case of the thermal aspects, the cell thermal conductivity is anisotropic, and several orders of magnitude bigger in the x and y directions in comparison to the z-axis conductivity.
- Last, and most important, the electrochemical processes are modelled within an EC model, which conversely to the physics-based models, does not capture the z-axis electrochemical differences.

On the other side, it is desired to obtain a 3D thermal model of the whole battery (including N cells and the pouch binder), since this is the model that can be used for the spatial optimization of the BTMS.

For all the reasons explained above, the final model couples both a 2D and a 3D domain, thus providing a 2D resolution of the cell performance (SOC, current density, voltage distribution, and other cell variables), and a 3D resolution of the battery temperature distribution.

5.2.2 Formulation

Electrochemical EC Model

The local electrochemical activity, or lithium transport, which is interrelated with all the above mentioned governing equations, is governed by the so-called NTG expression (derived by Newmann, Tiedemann [122] and Gu [123]), which is vastly employed in the literature to reflect the distribution of the electrochemical current and heat generation in large size lithium-ion cells, both for physics-based and empirically resolved electrochemical models [119]. The NTG linear polarization expression is written as

$$J = Y_{ec}\left((U_p - U_n) - U_{oc}\right) \tag{5.2}$$

where Y_{ec} and U_{oc} are respectively the battery electronic conductivity, in [S mm^{-2}], and the battery OCV, in [V]. U_p and U_n are the electrical potential values governed by the current collectors charge conservation model, in [V]. J is the total electrical current generation due to electrochemical reaction and ionic transport within the active materials, in [A mm^{-2}].

Observe that the use of this expression corresponds to the adoption of a very simple EC model consisting of a voltage source, U_{oc}, and a single serial resistor, R_{ec}, which represents the so-called battery internal resistor.

$$R_{ec} = \frac{U_{exp} - U_{oc}}{I_{exp}} \text{ in } [\Omega] \tag{5.3}$$

A simple EC model is adopted because the simulation objective concentrates in galvanostatic processes, in which the transient battery performance does not have a relevant influence. Besides, the conducted experimental observations (recall Figure 4.14, from the battery characterization section) corroborate that, at a fixed SOC, the charge and the discharge battery voltages, $(U_p - U_n)$, reflect approximately linear dependency on current. Nonetheless, observe that this simple EC model is adopted in a surface distributed fashion, since Y_{ec} is expressed in [S mm^{-2}], thus incorporating complex electrochemical phenomena that can occur in large surface cells, like concentration gradients and mixing effects. For that reason, this EC approach can be categorized as a pseudo-2D empirically-based electrochemical model.

To account for the electrochemical EC model, which governs in the coupled model framework the boundary conditions for the local electrochemical current generation (equation 5.5) and the reaction heat rates at every time step (equations 5.14 and 5.15), three look-up tables are built for the OCV, the entropic factor, and for the

associated battery electrical conductivity, U_{oc}, $\partial U_{oc}/\partial T$, and Y_{ec}, in order to replace the run-time computation of such EC.

The voltage source of the EC model is governed by the look-up tables $U_{oc} = U_{oc}(SOC)$ (from the fitted OCV measurements in section 4.2.2), with units of [V], and $\partial U_{oc}/\partial T = \partial U_{oc}/\partial T(SOC)$ (measured by Hukan, and shown in section 4.3.4), in $[\mathrm{V\,K^{-1}}]$. Considering the SOC influence within both empirical data sets, the effect of the temperature in the battery OCV for the EC model is taken into account by the first order Taylor series expansion of the U_{oc} in temperature (equation 2.8).

In the case of the electronic conductivity, $Y_{ec} = (1/R_{ec}).(1/(w_{bat}.h_{bat}))$, expressed in $[\mathrm{S\,m^{-2}}]$, the look-up table consists of three variable columns, namely the temperature, T, the operating current, I, and the SOC. A graphical representation of the Y_{ec} look-up table, including the whole set of battery cycling experimental data, presented in section 4.2.3, is shown in Figure 5.4.

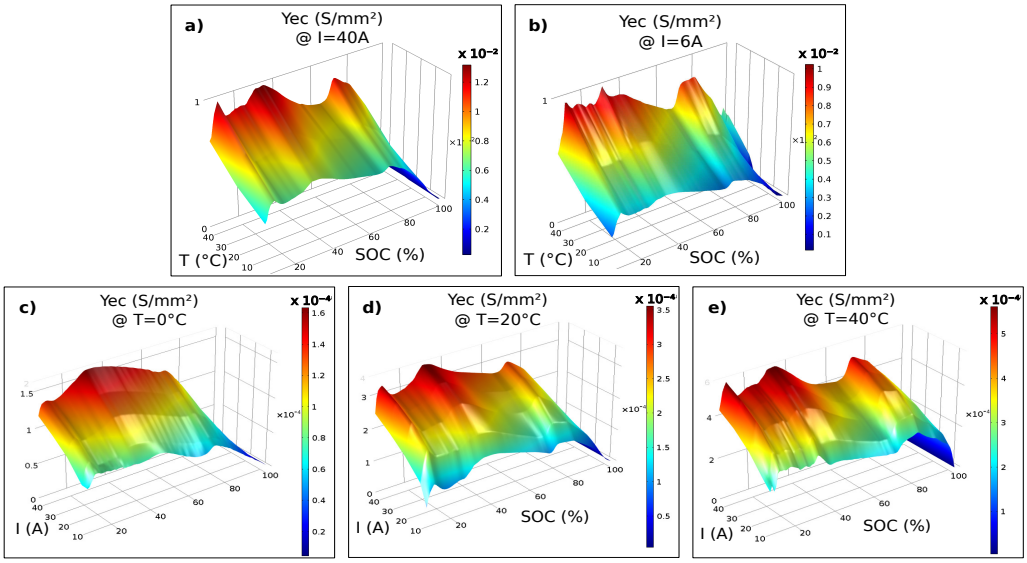

Figure 5.4: *Surface plots of the battery conductivity, expressed in* $[\mathrm{S\,mm^{-2}}]$*, and obtained by the experimental polarization characterization. In figures a) and b), the effect of the temperature can be observed at the maximum and minimum tested currents. In Figures c), d), e), the effect of the current rate can be observed at different temperatures.*

As a general tendency, observable in all the plots (a-e) gathered in the previous Figure 5.4, the SOC dependency of the conductivity is highly non-linear, showing three local maxima, at approximately 10, 30 and 70% SOC. The shape of the conductivity against SOC is approximately constant under all the tested conditions, and the global maxima can be related to the material phase changes, according to

the literature and to the experimental measurements, as it was observed that local peaks in $\partial U_{oc}/\partial SOC$ appear in the same SOC levels.

Besides, and conversely to what was concluded by Culcu et al. in [124], who observed a battery resistivity growth whenever the current rate was changed, it can be seen that in general the associated conductivity becomes higher at higher current rates, even though the experimental characterization started with the lowest currents and ended with the highest operating current values.

Current Collectors Electrical Model

As it can be observed in Figure 5.3, the electrochemical Li^+ transport generates, by charge conservation, electrical current density in the aluminium and copper current collectors when the battery is operated. Therefore, an electrical model is implemented to solve for the current collectors current, voltage distribution, and ohmic losses.

The IR imaging in [125, 29] have shown that significant temperature inhomogeneities can develop among the surface of large size pouch batteries during its operation, especially at high currents. The main source of those temperature inhomogeneities has been concluded to be the ohmic dissipation that is produced within the current collectors [30, 29]. Therefore, the electrical model of the current collectors is important for a good thermal approximation of the real operation of the battery, since it permits to capture these phenomena without adding much to the model complexity.

As depicted in Figure 5.5, two 2D domains are drawn in Comsol (see Figure 5.5), with height and width according to the battery measurements, gathered in Table 4.1, corresponding to the positive and the negative current collectors of a cell unit Ω_p and Ω_n.

Two different domains are needed because the material properties and the thickness of each current collector are different, as well as their boundary conditions. Of course, the potential distribution is, hence, different in each current collector, and two different conservation equations need to be solved separately in Comsol, one corresponding to each domain. Conversely, the electrochemical reaction current and the SOC models are solved uniquely in the subdomain Ω_{ec}, delimited in a yellow pointed line in Figure 5.5, since both current collectors sandwich a single pair of active materials, and therefore a unique electrochemical reaction and SOC distribution solutions exist.

The governing energy balance equations (from *Electrical Currents* Comsol physics interface) that are applied to solve for electrical charge conservation in Ω_p and Ω_n

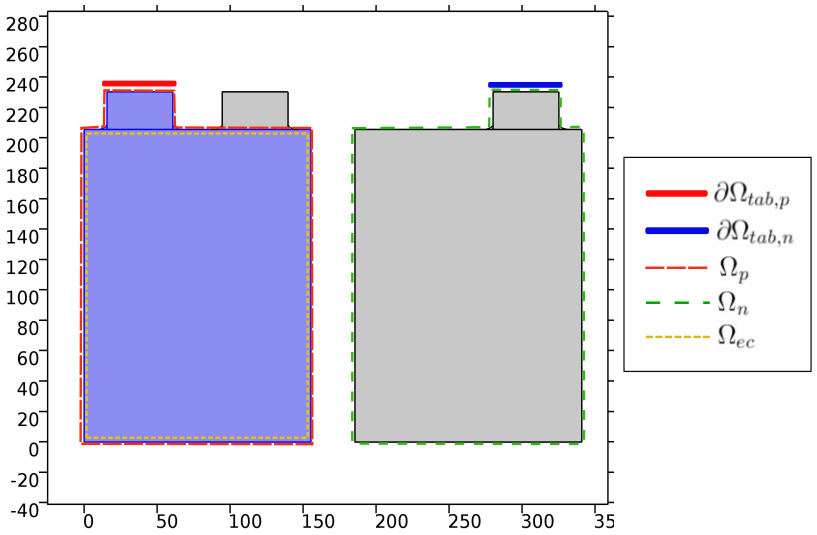

Figure 5.5: *Scheme of the 2D simulation domains for the cell model. Delimited in dashed lines: in yellow, Ω_{ec}, in red, Ω_p, and in green, Ω_n.*

are

$$\begin{cases} \nabla \cdot \mathbf{J} = Q_j \\ \mathbf{J} = \sigma \mathbf{E} + \frac{\partial \mathbf{D}}{\partial t} + \mathbf{J}_e \\ \mathbf{E} = -\nabla U \end{cases} \tag{5.4}$$

where, in the first equation, which stands for charge conservation, $\mathbf{J}$ is the current density, in [$\mathrm{A\,m^{-2}}$], and Q_j is an external volumetric current source, in [$\mathrm{A\,m^{-3}}$]. In the second equation –Ohm's law– σ is the electrical conductivity ($\mathrm{S\,m^{-1}}$), $\mathbf{E}$ is the electric field intensity [$\mathrm{V\,m^{-1}}$], $\mathbf{D}$ is the electric displacement or electric flux density, in [$\mathrm{C\,m^{-2}}$], and $\mathbf{J}_e$ is an externally generated current density, in [$\mathrm{A\,m^{-2}}$]. In the third equation, U is the scalar electric potential, in [V].

As explained above, the electrochemical ionic transport in the electrodes generates a current density on the current collectors surface in contact with the electrodes, and this current flows out (or in) through the current collector tabs to the external electrical circuit. This is modeled through the boundary conditions in the current collectors.

1. First, in the positive electrode, Ω_p, a volumetric body current source is applied to the subdomain corresponding to Ω_{ec}, accounting for the electrochemical activity:

$$\nabla \cdot \mathbf{J} = Q_{j,p} \ ; \quad \text{on } \Omega_{ec} \tag{5.5}$$

where the source term $Q_{j,p}$ is related to the value of the electrochemical ionic transport J that is determined from the empirically based EC model by the expression 5.2, by taking into account the appropriate volumetric factor (or specific length). Thus, $Q_{j,p} = a_p \cdot J$ in the positive current collector, where $a_{cc,p} = 1/z_{cc,p}$ is the specific area of the positive current collector, in $[\mathrm{m}^{-1}]$.

2. On the other side, a Newmann boundary condition is applied at the positive current tab extreme, $\partial\Omega_{tab,p}$ to specify the normal current density which is introduced/extracted (charge/discharge) to the battery from the external circuit:

$$\mathbf{n} \cdot \mathbf{J} = -J_n \ ; \quad \text{at } \partial\Omega_{tab,p} \tag{5.6}$$

where $\mathbf{n}$ is the unit outward normal vector, and the current density, $J_n = I_{cell}/A_{tab,p}$. Here, $A_{tab,p}$ is the transversal area of $\partial\Omega_{tab,p}$, and the cell current is $I_{cell} = I_{bat}/N$.

At the other boundaries, $(\partial\Omega_p - \partial\Omega_{tab,p})$, electric insulation is prescribed, since all the current flows inside/outside the current collector via the current tabs.

$$\mathbf{n} \cdot \mathbf{J} = 0 \ ; \quad \text{at } (\partial\Omega_p - \partial\Omega_{tab,p}) \tag{5.7}$$

The boundary conditions on the negative current collector domain, Ω_n, are similar to those described above. The only differences are: first, that the sign of the electrochemical current source is reversed ($Q_{j,n} = -Q_{j,p}$); and second, that the condition in the negative tab edge is set, in this case, to a Dirichlet boundary condition instead of a Newmann one. The voltage at the negative current tab is set to zero (ground)

$$U_n = 0 \ ; \quad \text{at } \partial\Omega_{tab,n} \tag{5.8}$$

Observe that a Dirichlet boundary condition is needed for preventing the *Electrical Current* physic interfaces of having infinite solutions, and is sufficient for both positive and negative current collector domains to have a single solution since they are coupled through the source term $Q_{j,i}; i = p, n$.

The initial conditions are $U_p = U(SOC(t_0), T_0)$, on Ω_p, and $U_n = 0$, on Ω_n,

where, again, $U(SOC(t_0), T_0)$ refers to the experimental values described in section 4.2.3.

Note that in order to evaluate Q_j it is necessary to define two linear extrusion mapping functions that can map the solution of the positive current collector voltage, U_p, to the negative current collector domain, and viceversa: φ_{pn} and φ_{np}. Thus, for example,

$$\varphi_{pn} : \Omega_p \rightarrow \Omega_n \tag{5.9}$$

Regarding the geometrical definition of the current collectors simulation model, the thickness of each of the current collector's domain is taken from the values z_p and z_n, presented in Table 5.1. However, the thickness of the domain corresponding to the current collector tabs, Ω_p and Ω_n, is taken as

$$z_{\Omega_{tab,j}} = \frac{z_{cc,j}}{N} \quad \text{for } j = p, n \tag{5.10}$$

as it has to be taken into account that the model solves for a single cell within the N cells inside a pouch battery.

In order not to cause singularities, the transition between both domain thicknesses has to be smooth. Therefore, the thickness of the current collectors domains is defined with a step function in Comsol, which ensures the thickness transition of the domains with C^2 continuity. Note that the definition of this thickness transition is completely arbitrary, and that this may affect considerably the amount of local ohmic losses in the thickness transition zones. In practice, this current collectors thickness transition may also be very difficult to characterize, as it may rely on the quality of the welding process between the different current collectors within the pouch battery.

Regarding the material properties of the electrical current collector domains, some known material properties are adopted, from the Comsol material library. The electrical conductivity of the positive current collector (aluminium) is of $2.326e7\,\mathrm{S\,m^{-1}}$, and of $5.998e7\,\mathrm{S\,m^{-1}}$ for the negative collector (copper).

SOC Model

The state of charge is determined in the model subject to the local through-plane lithium ion transport density J. The SOC is governed then, locally, with a first order ODE, defined in a *Coefficient Form PDE* Comsol physics interface, as

$$\frac{Q_{bat}}{A_{bat}}\frac{\partial(SOC)}{\partial t} = J \tag{5.11}$$

where A_{bat} is the surface area of the active materials of the battery, in m^2, and corresponds to the domain Ω_{ec}.

The boundary conditions for the SOC governing ODE model are set to zero flux at any boundary. The initial condition, or initial SOC of the simulation, is fixed by a user parameter which serves to specify $SOC(t_0)$.

Thermal Model

A 3D thermal model of the cell is coupled with the previously described models to solve for the temperature distribution of the battery. To this end, the electrochemical heat sources (that depend on the 2D cell models above) are applied to the 3D thermal domain as a distributed heating source power, and the external battery boundary conditions (including the pouch film and the external heat convection or conduction) are set to the model to estimate the temperature distribution of the battery of study under operation regimes.

The governing equations of the *Heat Transfer in Solids* physics interface in Comsol, which are applied to a simple cubic domain (whose volume corresponds to the battery volume, $w\mathrm{x}h\mathrm{x}z_{bat}$), read

$$\rho C_p \frac{\partial T}{\partial t} + \nabla \cdot \mathbf{q} = \dot{q} \tag{5.12}$$

where all the terms result into volumetric energy units, $[\mathrm{J\,m^{-3}}]$. By Fourier's law, the conductive heat flux within the cell domain is written

$$\mathbf{q} = -\kappa \nabla T \tag{5.13}$$

Recalling the thermodynamic balances that were described in section 3.2.1, the battery electrochemical heat generation is computed in the simulation by the adaption of equation 3.4. In this case, the volumetric irreversible heat contribution can be written as

$$\dot{q}_{irrev} = a_s J((U_p - U_n) - U_{oc}) \tag{5.14}$$

where $a_s = \frac{1}{z_p + z_n + z_s}$ is the specific area of the cell active materials, J corresponds to the electrochemical current density, in $\mathrm{A\,m^{-2}}$, U_p and U_n are the positive and negative voltages (corresponding to the solution, at every time step, of the electrical

current collector models), and U_{oc} is the empirical battery OCV.

Similarly, the volumetric reversible heat source is

$$\dot{q}_{rev} = a_s J \left(T \frac{\partial U_{oc}}{\partial T} \right) \tag{5.15}$$

where $\left(\frac{\partial U_{oc}}{\partial T}\right)$ is the empirical entropic factor.

Apart from the electrochemical heat sources, the ohmic losses which are generated in the current collectors (equation 5.16) are also mapped to the 3D thermal model as a volumetric heating source by the addition of the *Electromagneting Heating* coupling physics interface from Comsol.

$$\dot{q}_{ohm} = a_p \sigma_p \Delta U_p + a_n \sigma_n \Delta U_n \tag{5.16}$$

The mapping function that is used to project all the heat sources from the 2D mesh to the 3D battery domain, φ_{2d-3d}, projects any point from the cell surface to the battery volume independently of the z-coordinate:

$$\begin{aligned} \varphi_{2d-3d} \; : \quad & \Omega_{ec} \rightarrow \Omega_{bat} \\ & (x, y, 0) \rightarrow (x, y, z) \end{aligned} \tag{5.17}$$

Since in the conduction of this project no battery has been opened to examine the properties of each of the components, the material properties that have been adopted for the battery thermal model in this work are based on the properties which were recently reported for LFP cathode batteries by Lai et al., in [89], Vertiz et al., in [83], and in [90] by Saw et al.

Considering that the electrochemical cell is composed by a stack of different material layers, the density can be averaged by taking into account the volume, V_i, and the density, ρ_i of every layer conforming the cell, by

$$\rho = \frac{\sum_i \rho_i V_i}{\sum_i V_i} \tag{5.18}$$

The previous equation was used with the data provided in [89], [83], and [90] to estimate the total weight of the battery. Each layer volume V_i was computed as the product between the surface of the cell (measured) times the thickness of every layer provided in the previous papers. As compared to the measured weight, the lowest weight estimation error was obtained with the parameters from Vertiz et al. ([83]), whereas the highest divergence was obtained with the parameters provided by Saw et al. For that reason, the thickness z_i and the density ρ_i of every layer are

taken from [83], and correspond to the values gathered in Table 5.2. The final value of the lumped cell density in the model is, then

$$\rho_{cell} = 2045,38 kg.m^{-3} \tag{5.19}$$

Table 5.2: *Adopted thickness and density of every layer component of the electrochemical cell model. Data from [83].*

Component	Thickness ([μm])	Density ([$\mathrm{kg\,m^{-3}}$])
Graphite Anode	67	2660
Copper	13	8900
LFP Cathode	98	1500
Aluminum	20	2700
Separator	25	492
Pouch Binder	150	2038

For the heat capacity, a similar expression can be used

$$\rho C_p = \frac{\sum_i \rho_i V_i C_{p,i}}{\sum_i V_i} \tag{5.20}$$

and in this case an average of the reported heat capacities in the three previously mentioned papers are employed. Using the thickness of every layer already selected before, finally the heat capacity for the present model is

$$C_p = 1235,192 \ \ \mathrm{J\,kg^{-1}\,K^{-1}} \tag{5.21}$$

Moreover, our heat capacity measurements (section 4.3.3), confirm this battery property approximation.

Regarding the thermal conductivity, and considering the layered nature of the electrochemical cell, it is clear that this property is not isotropic, because when, i.e., two different elements in a layered structure with thermal conductivities κ_1 and κ_2 are in parallel (Figure 5.6 A), the resultant thermal conductivity must be computed by

$$\kappa = \frac{A_1}{A_1 + A_2}\kappa_1 + \frac{A_2}{A_1 + A_2}\kappa_2 \tag{5.22}$$

and, on the other side, when the elements are connected in series (Figure 5.6 B), the thermal conductivity is determined as

$$\kappa = \frac{L_1 + L_2}{(L_1/\kappa_1) + (L_2/\kappa_2)} \tag{5.23}$$

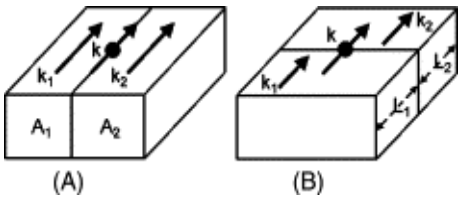

Figure 5.6: *Schematic of the effective thermal conductivity for a layered configuration of two materials, in parallel (A) or in series (B). Figure reprinted from [6].*

Using an average of the thermal conductivities presented in the above stated papers, and the selected thickness of every layer, the thermal conductivities $\kappa_x = \kappa_y$ and κ_z are obtained by equations 5.23 and 5.22, respectively. However, analysing the results, and as observed by Vertiz et al., who measured the through-plane thermal conductivity using a standard ASTM procedure, showed that the obtained value for κ_z, when using equation 5.22, is much bigger than what is reported in other studies in which the through-plane thermal conductivity has been measured. The explanation of such a difference must be that the contact resistance in between every cell layer might not be negligible. Thus, finally, the thermal conductivities for the model $\kappa_x = \kappa_y$ are computed by equation 5.23, whereas the value for κ_z is taken directly from the measurements in [83], instead of the value that can be computed from equation 5.22. Finally, the thermal conductivity values in the model are:

$$\kappa_x = \kappa_y = 193,185 \ \ \mathrm{W\,m^{-1}\,K^{-1}} \tag{5.24}$$

$$\kappa_z = 0,284 \ \ \mathrm{W\,m^{-1}\,K^{-1}} \tag{5.25}$$

Apart from the electrochemical cells sandwich, a pouch battery is packed within a pouch binder material. Since the definition of such a thin domain would require to refine drastically the mesh, the pouch material is introduced in the model as a *Thin Thermally Resistive Layer* boundary condition, in Comsol, which is characterized by a thickness $z_{pouch} = 150\mathrm{mm}$ (Table 5.2) and a thermal conductivity of $\kappa_{pouch} = 0.249\mathrm{W\,m^{-1}\,K^{-1}}$.

The flux across the pouch binder film can be written as:

$$\begin{cases} -\mathbf{n}_d \cdot (-\kappa_d \nabla T_d) = -\kappa_{pouch} \frac{T_u - T_d}{z_{pouch}} \\ -\mathbf{n}_u \cdot (-\kappa_u \nabla T_u) = -\kappa_{pouch} \frac{T_d - T_u}{z_{pouch}} \end{cases} \tag{5.26}$$

where the subscripts u and d respectively refer to the upside and the downside of the slit.

This boundary condition is applied to all the boundary surfaces of the 3D model, and other heat flux boundary conditions (like external heat conduction and convection) can be applied on top of the resistive film boundary condition depending on the desired case of study.

Chapter 6

Battery Model Results

6.1 General Features

6.1.1 Pouch Cells Phenomena

In Figure 6.1, which gathers different model plots at 15% SOC during a deep 1C charge process, can be observed that the model replies to the phenomena belonging to large pouch cells that has been also reported in [28, 29, 30].

In small cylindrical cells, the surface of the current collectors is relatively small, and due to their very high electrical conductivity properties, the potential drop among the surface of the current collectors can usually be neglected. However, in large pouch cells the non-ideal electrical conductivity of the current collectors generates a slight but non-negligible potential drop among its surface, especially near the current collector tabs, where the constriction/spreading of the current during charging and discharging generates higher voltage spatial gradients, ∇V.

As depicted in Figure 6.1, several consequences arise from this consideration:

1. Larger overpotential ($U_p - U_n$) near the positive and negative current tabs, generated by Ohm's law and electrical constriction, promotes faster electrochemical reaction rates. Equivalently, higher localized overpotential results in a higher electrochemical production near the tabs.

2. A higher electrochemical activity near the current tabs leads to a higher heat generation rate (equations 5.14 and 5.14) and, hence, to a higher localized temperature. As a consequence, since the electrochemical activity Y_{ec} (or ionic transport) rises with increasing temperature, a further and faster electrochemical reaction is promoted in these regions.

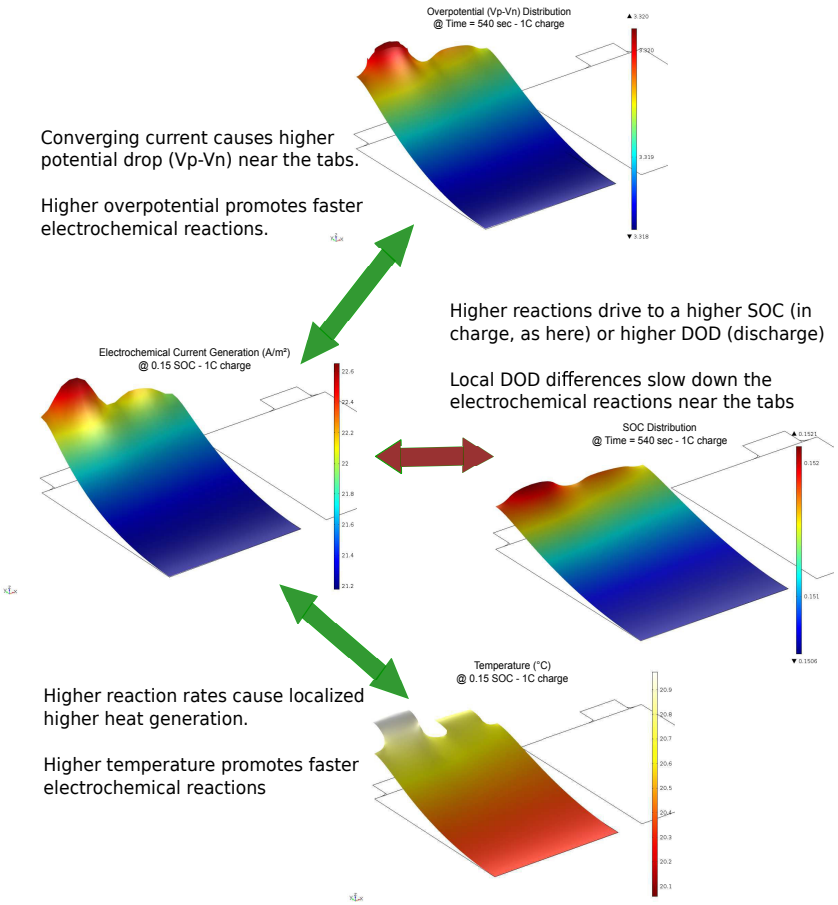

Figure 6.1: *Graphical explanation of the internal cell imbalance that reproduces the model. All the plots are obtained at 15% SOC during 1C charge (starting at 0% SOC) at 20°C.*

3. On the other side, higher electrochemical activity near the current collector tabs lead to a faster discharge (or charge) celerity, which translates into electrical imbalance within the battery. Normally, at a certain operation point (under continuous charging or discharging, but also for any other operational regime), the ionic conductivity of the region near the tabs decreases due to diffusion limitations, consequently counter-balancing the electrical imbalance.

6.1.2 Convergence and Accuracy

Solver and Time Stepping Methods

Two different time-stepping methods have been compared for the solution of the derived transient model: the *generalized alpha* and the *Backward Euler* (BDF) method.

Both methods are implicit and, hence, *unconditionally stable*. The use of an explicit time stepping method is discarded because the coupled model is a non-linear PDE system with convective terms and high non-linearities in time dependence within the look-up tables. Therefore, an explicit method would require impractical small time steps to keep the error bounded and the solution stable.

Comparing the solutions of both methods with the same mesh, it is observed that the BDF, as compared to the generalized alpha, tends to considerably damp any high frequency variations. Smoother gradients are shown, i.e., in the distribution of the electrochemical reaction rates or the reaction heat source rates near the current tabs. In the case of the generalized-alpha solution, different gradient instabilities appear near the current collector tabs. This is not related to any physical phenomena but seems to occur rather due to numerical instabilities that would require local mesh refinement. As a consequence of the sharp gradients, the generalized alpha method requires much more computational time, the ratio being approximately of 18:1, which would even be greater if the mesh for the generalized alpha was refined near the tabs.

For that reason, and as suggested in the documentation of Comsol [147] in the case of dealing with applications which require of extra numerical robustness, the time stepping method that is selected to solve the implemented model is the Backward Euler (BDF) method. The BDF implementation in Comsol is of variable order, and a maximum integration order of 2 is set. By default, a free time step selection is defined in this software, but different time step intervals can also be fixed, as it is investigated in the next section.

In the case of the solver selection from the pre-defined Comsol algorithms, it has been observed that both the *MUMPS* and the *PARDISO* solvers performed well, and much better than the *SPOOLES*, which might suggest that the system has proven some reliability.

Time Step Convergence

As explained above, an implicit time stepping method has been selected for the solution of the system of PDEs to allow for large time-step sizes. However, stability is one issue but accuracy is a different one. It has been observed that slight violations of the current conservation law appear when integrating the current density which has been generated in the surface of the current collectors (due to electrochemical transport) and comparing it to the input current through the current collector tabs.

This can be explained because of the high non-linear dependency of the electrochemical look-up tables with respect to the SOC or, what is equivalent (during

charging process), with respect to time. It has been observed that the charge conservation problems are localized in the SOC where the U_{oc} and Y_{ec} tables present non-linearities.

Figure 6.2 shows how the integration of the through-plane current generation due to the cell electrochemical activity begins to oscillate when the current regime starts ($t = 0$), and requires approximately 200 to 500 seconds to reach equilibrium (equation 6.1 is satisfied accurately).

$$I_{battery} = N \cdot \int_{\Omega_{ec}} \frac{1}{a_p} Q_{j,p} d\Omega = N \cdot \int_{\Omega_{ec}} J d\Omega \tag{6.1}$$

Running the simulation for different time step sizes, it can be observed (as depicted in Figure 6.3) that the surface integration of the through-plane current density, J, as well as the local maximum difference of it ($max(J) - min(J)$), converge linearly as the solver time step size is set to a smaller value. On the other side, smaller maximum step sizes carry obviously longer computational costs. Therefore, the maximum step size is optimized in the simulation model for the case of 1C-rate full charge (basic simulation target, as explained in 5.1). Consequently it becomes smaller in the SOC regions (or time, t) in which the current oscillations appear.

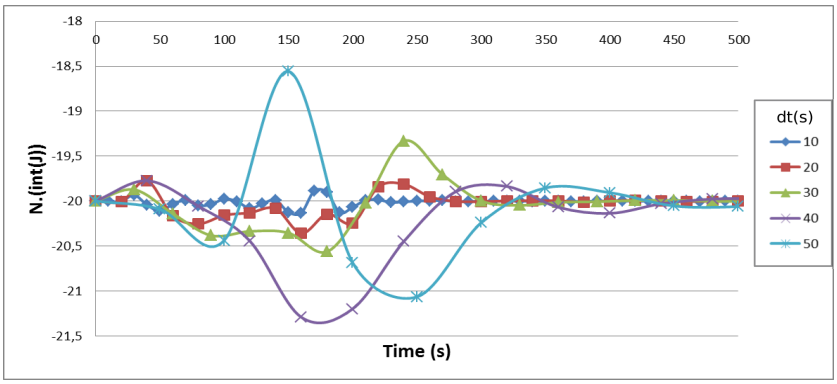

Figure 6.2: *Plot of the surface integration of the electrochemically generated current during a simulation where a current pulse of* $I_{battery} = 20\text{A}$ *was applied, beginning at* $t = 0s$.

Mesh Convergence

Different finite element meshes have been tested both for the 2D and the 3D simulation domains in order to observe and prove the accuracy and the convergence of the derived model. On the left graph of Figure 6.4, it can be observed that the solution of the temperature near the current collector tabs, which correspond to the

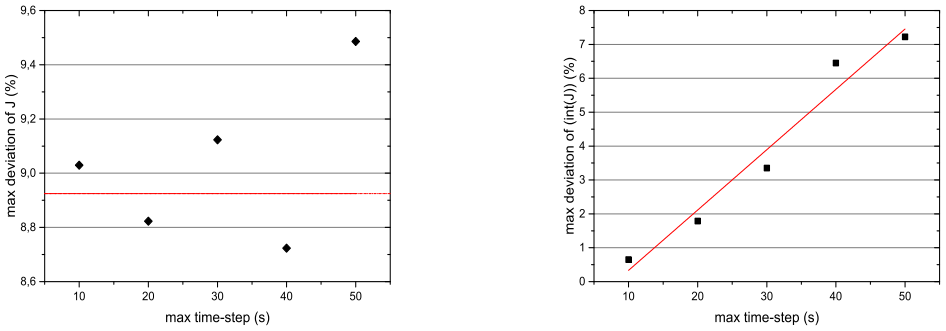

Figure 6.3: *On the left, the maximum relative deviation of the local J converges to a stable value of approximately 8,9%. On the right, the difference between the overall surface integrated current and the prescribed value of $I_{battery}$ tend to zero with decreasing time step sizes.*

domain regions where sharpest gradients appear, converges as the number of degrees of freedom (DOF) of the mesh increase. On the other side, the computational effort, or time, which is required to solve for the simulation model increases sharply, as it can be seen in the logarithmic plot on the right.

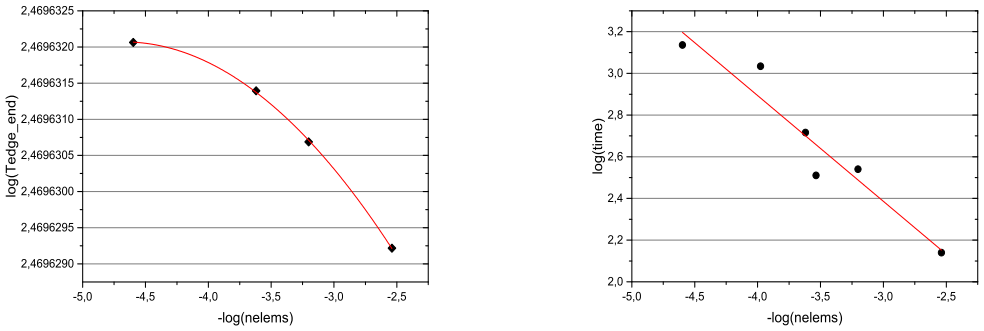

Figure 6.4: *Plot of the effects of the model mesh refinement. On the left, convergence logarithmic plot of the model local temperature solution with increasing number of DOF. At the right, effect of the mesh refinement on the computational cost (time).*

As observable, the local temperature solution (Figure 6.4) converges fasterthan the usual linear convergence that is obtained in logarithmic plots. This can be explained by the automatic mesh refinement that is implemented in Comsol, that updates and refines the mesh in the regions where sharper gradients appear within the solution.

Once convergence has been proved with a very fine mesh, the final selection of the

mesh is a compromise between the accuracy and its computational cost. Whereas in the 2D current collector domains, a triangular mesh has been chosen. A hexahedral mesh has been used in the 3D battery domain in order to optimize the computational cost. Since the battery's aspect ratio is big and sharper temperature gradients are expected within the z-axis, due to the very lower battery thermal conductivity in this direction. The use of this mesh permits decreasing the number of DOF without altering the accuracy of the model (recalling that the element quality is not as relevant in the case of a hexahedral mesh, as compared to a tetrahedral elements mesh).

6.2 Battery Simulation Results

6.2.1 Electrical Performance

In the following Figure 6.5, the potential difference between the potential distributions at Ω_p and Ω_n, which can be written as $U = U(\Omega_p) - U(\Omega_n)$, is shown for an arbitrarily selected SOC (or simulation time) during a 1C-rate charge simulation.

Note that the surface plot corresponds to the electrochemical cell domain, Ω_{ec}. Hence, this is the potential distribution that governs the electrochemical activity distribution (by equations 5.2 and 5.5).

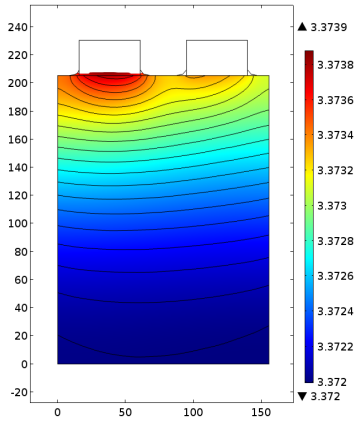

Figure 6.5: *Surface plot of the electrical potential difference between the two current collectors, $[U(\Omega_p) - U(\Omega_n)]$, at 30% SOC for a simulation of 1C-rate charge.*

It has been observed that the maximum surface voltage differences depend on the current rate of the simulation, as it can be expected by the acknowledgement of the underlying governing equations (Ohm's law). Moreover, and in agreement with the previous statement, it is observed that the dependency on SOC of the voltage

distribution of the positive and the negative current collectors is negligible. This means that the voltage distribution shown in Figure 6.5 is qualitatively constant among the whole charging progress.

The minor potential distribution differences, among the current collector surfaces, cause some local variations in the electrochemical reaction current density (recall equations 5.2 and 5.5). Thus, a higher electrochemical current rate generation near the current tabs is driven for almost the whole charge process because of the major electric potential difference.

However, at around 70-75% SOC (during charge processes), the electrochemical conductivity Y_{ec} decreases continuously, and substantially as compared to its variations among the range 0-70% SOC, shifting the maximum electrochemical current production zone to the regions that possess a slightly lower SOC. This regions correspond to the opposite regions of the current collectors position, as it can be seen Figure 6.6.

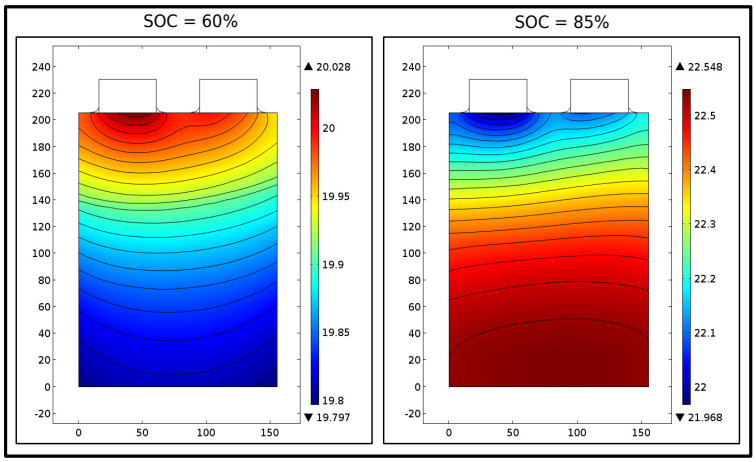

Figure 6.6: *Distribution of the reaction current density production, J, at different SOC during a 1C-rate charge simulation.*

Voltage Curves Validation

From the obtained numerical voltage distribution within the 2D current collector domains, the model battery voltage can be calculated by

$$U_{bat} = \bar{U}_{tab,p} - \bar{U}_{tab,n} \tag{6.2}$$

where $\bar{U}_{tab,j}$ is the average voltage of the current collector tab boundary, which can be written as:

$$\bar{V}_{tab,j} = \frac{1}{w_{tab}} \int_{\partial\Omega_{tab,p}} V dx \quad \text{for } j = p, n. \tag{6.3}$$

Here it is worth recalling that, even if the simulation corresponds to a single electrochemical cell, the voltage from equation 6.2 corresponds to the battery voltage as the N cells composing the pouch battery are assembled in parallel.

Hence, the obtained voltage response of the battery model U_{bat} under different C-rate constant current charge conditions is plotted in Figure 6.7 (scatter points) and compared to the experimental values (solid lines), showing a very good agreement for all the tested conditions.

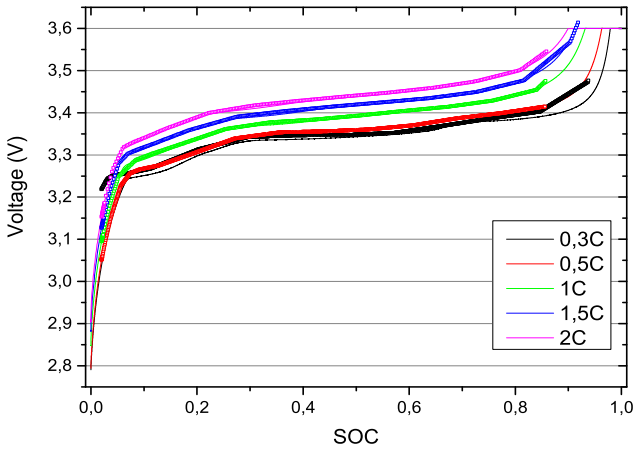

Figure 6.7: *Model voltage curve predictions for CC charging processes at 20° C and different current rates (scatter points) and comparison to the experimentally obtained values (solid thin lines).*

6.2.2 Thermal Performance

A surface plot of the model heat generation rate distribution is shown in Figure 6.8, where the left and the right plots refer to exactly the same numerical data and differ only on the colour label scale.

The volumetric ohmic heat generation due to current constriction, localized in the current tabs and its vicinities, proves to be of a much larger order of magnitude than the one of the electrochemical processes. In the case of the present model, it can be concluded, hence, that even if the thickness and volume of the current collector tabs is much lower than the cell volume, the localized ohmic heat dissipation might

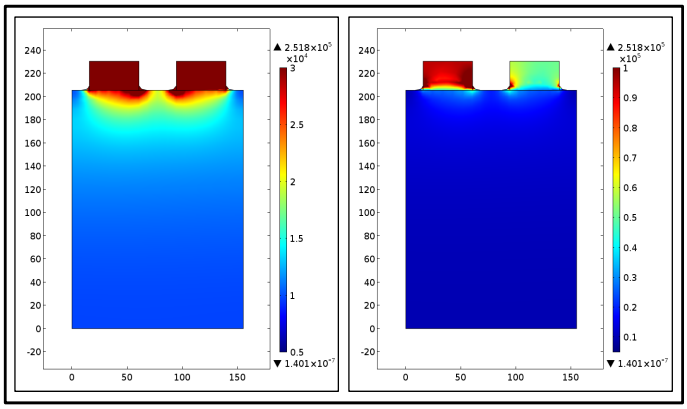

Figure 6.8: *Surface plot of the battery volumetric heat generation rate distribution, at 30% SOC, undergoing a 1C-rate charge simulation.*

be one of the most important factors causing temperature gradients across the cell, as it was also presented in other publications ([38, 30]).

The total battery heat generation can be obtained from the derived *single-cell* model by integrating all the volumetric sources (including electrochemical and electrical heating sources) along the cell domain volume and multiplying by the number of cells, N, that conform the battery.

$$\dot{q}_{battery} = N \cdot \left(\int_{\Omega_{ec}} (\dot{q}_{irrev} + \dot{q}_{rev}) d\Omega + \int_{\Omega_p} \dot{q}_{ohm} . d\Omega + \int_{\Omega_n} \dot{q}_{ohm} . d\Omega \right) \tag{6.4}$$

In Figure 6.9, the total battery heat generation predictions, in [W], are shown for different current rate runs (considering isothermal operation conditions).

As explained in the model formulation, the battery heat dissipation sources can be decomposed in: irreversible reaction heat, $\dot{q}_{irrev}$, reversible entropic heat, $\dot{q}_{rev}$, and ohmic heat, $\dot{q}_{ohm}$ (recall equations 5.14, 5.15, 5.16).

In order to obtain a comprehensive picture of the influence that has each of the heating sources in the total battery heat generation rate, a plot of the decomposed heat sources, for a 1C charge at 20°C, is included hereafter (Figure 6.10).

From the observation of the previous figure, it can be observed that, during a 1C-rate charge, the reversible and the ohmic heat sources have a big relevance in the overall battery heat dissipation. This demonstrates that, at least in the case of the battery of study, the computation of all the heat source terms is crucial for obtaining accurate heat generation predictions.

Besides, it can be observed that, since the adopted EC model consists of a

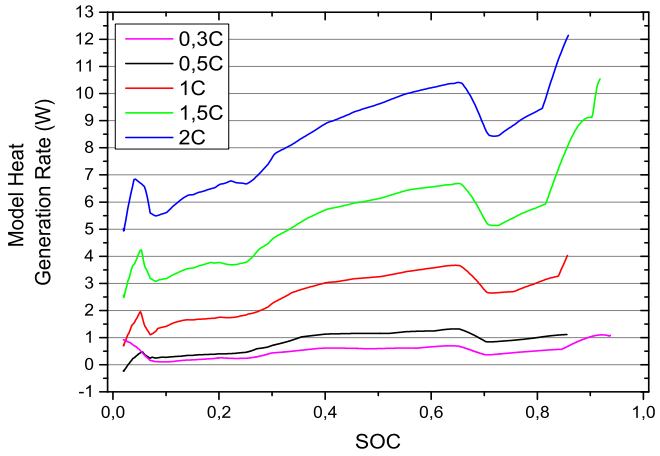

Figure 6.9: *Integrated model heat generation rate predictions for one battery, in* [W]*, for CC charging processes at different current rates and isothermal operating temperature of 20° C.*

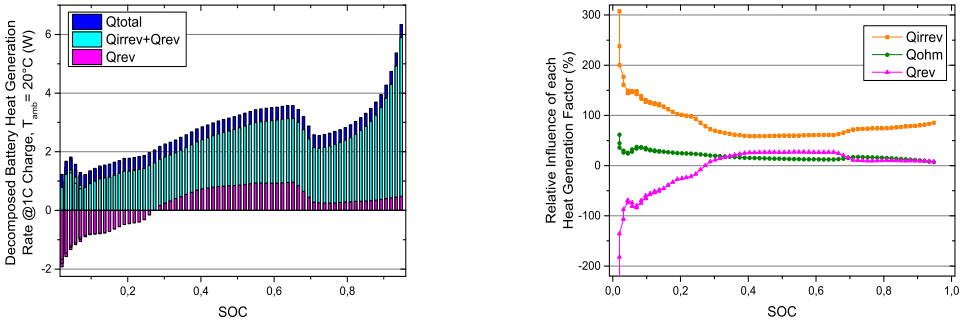

Figure 6.10: *On the left, plot of each decomposed source of the integrated battery heat generation, including the reaction heat and the ohmic dissipation. On the right, plot of the relative influence of each of the heat source terms on the overall battery thermal dissipation power.*

simple resistor and, thus, the transient evolution of the battery overpotentials is not properly accounted, the irreversible reaction heat source in the model is probably overestimated.

Ohmic Heat Analysis

The numerical information that is plotted in Figure 6.10, shows that the ohmic heat prediction from the model corresponds, in average, to the 20% of the total battery

heat dissipation during a 1C full charge process at an ambient temperature of 20°C.

However, note that the ohmic heat dissipation rate arises from the solution of the electrical model within the current collectors and is clearly dependent on the geometry definition of the aluminium and copper collectors. Since the internal configuration of the battery sample has not been examined in this project, the geometrical definition of the current collectors, which relies on some literature parameters and the definition of some arbitrary corner radius approximations, might drive to an inaccurate prediction of the real magnitude of the ohmic heating power.

The definition of the arbitrarily smoothed corners parameters is mandatory in order not to generate singular solutions, as it is well known that sharp corners will cause a singularity in the derivatives of the dependent variables for all elliptic partial differential equations [126]. This is here specifically mentioned because this consideration has been overlooked in other publications [109, 30], in which the convergence of the model is never discussed, and in which the domain and boundary conditions definition might lead to unbounded singular and mesh size dependent solutions.

In order to quantify the influence of different arbitrarily-defined model parameters, some parametric sweep simulations have run to observe the effect of the variation of the main influential factors. Figure 6.11 shows that the number of cells that conform a pouch battery, N, has a large impact on the total amount of ohmic dissipation power as compared to the influence that the *Smoothing* parameter[1] has.

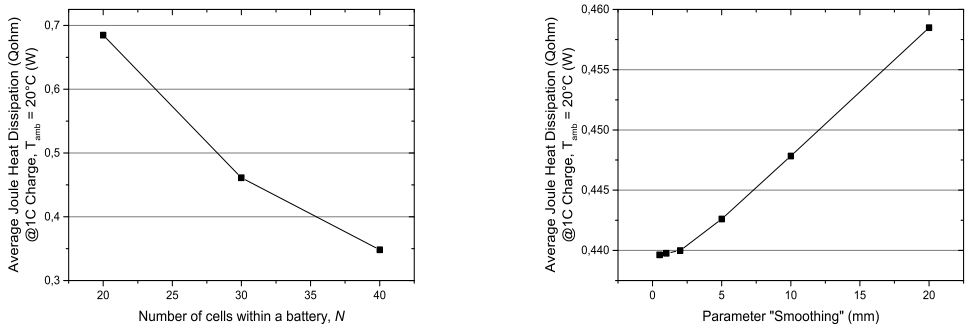

Figure 6.11: *Plot of the influence of the number of cells N (left) and the "Smoothing" parameter from Comsol on the amount of the (average) battery ohmic heat dissipation, in* W*, undergoing a 1C galvanostatic charge at 20° C.*

The number of cells N affects the ohmic heat generation because it directly

[1]The "*Smoothing*" parameter defines the amplitude of the thickness transition at $y = 155,6$mm (e.g., for the positive current collector domain, from $z_{cc,p}$ (see Table 5.1) to $z_{tab,p}$ (see equation 5.10)).

affects the electrical constriction/spreading due to the thickness reduction of the current collectors when they merge in the battery tabs (see equation 5.10). It has been proved to be, in the case of the present model, the most influential factor in the total amount of ohmic heat dissipation.

Whereas the number of cells N, as well as the radius could be analyzed by the internal examination of the battery, the real physical sources behind the ohmic dissipation might be of difficult analysis. For example, the manufacturing process of the battery core or, more precisely, the welding between the different current collectors of the cell which conform the parallel connection between the different cells conforming a pouch battery, may result in localized microscopic gaps between mating tabs in the stack. These gaps decrease the effective area for current flow, even if advanced welding techniques such as ultrasonic metal welding or laser beam welding are employed, and increase the ohmic losses [125].

However, an overall analysis through IR imaging or distributed temperature sensing, would suffice to properly estimate the concrete amount of ohmic heat dissipation without needing deeper insights on the microscopic level.

According to the argumentation presented by Zhao et al. in [7], from the left plot in 6.11 it can be clearly observed that thicker electrode batteries (with fewer number of cells within a pouch battery, N) promote higher ohmic dissipation. Therefore, thicker electrodes with higher energy density (due to larger ratio of active materials) are often compromised with a higher temperature homogeneity, which translates into higher capacity fade rates especially at high discharge rates. On the other side, thinner electrodes (with fewer energy density) are shown to hold better thermal response, and thus allow for better cyclability at high current rates. Hence, this plot illustrates one of the main differences between energy and power batteries.

Last but not least, and to conclude with this section, it is worthwhile mentioning that the ohmic heat source in the current tabs is predicted to be higher in any kind of application due to the contact resistance between the tabs and the rest of the batteries or the electric or electronic system, even if the battery connectors are properly welded.

The Effect of External Convection

As explained in detail in the introductory chapter, section 2.3, the temperature is with no doubt one of the most influencing factors on the battery performance. For that reason, the boundary conditions of the 3D battery model affect the battery temperature and, hence, the heat generation predictions, as well as any other magnitudes. To illustrate the effect of the battery heat dissipation, the model heat

generation rate results are shown in Figure 6.12 for different air convection coefficients, h.

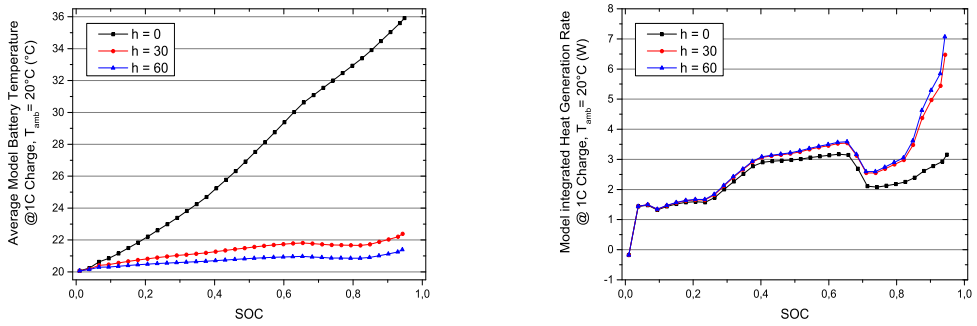

Figure 6.12: *Average temperature (left) and integrated model heat generation rate predictions (right) for a 1C charging process at an ambient temperature of 20° C and different external air convection coefficients, h.*

As it can be seen on the right, in Figure 6.12, whereas the influence on the heat generation rate (in W) is not excessive, the model battery temperature changes drastically, from isolated conditions ($h = 0$) to high forced air convection ($h = 60$).

Validation of the Heat Rates

The model average temperature predictions for 0,5C and 1C are qualitatively compared to the experimental data obtained from the electrical and the thermal characterization processes in Figure 6.13: the dashed lines correspond to the model results; the continuous lines, to the temperature sensor measurements within the climate chamber cycling measurements; and the scatter dot points refer to the temperature increase measured within the calorimeter chamber.

As explained above, the air convection coefficient that determines the heat dissipation of the battery model affects drastically the temperature predictions of the model. For that reason, a quantitative comparison of the model predictions to the measurements in the climate chamber and in the calorimetric chambers, where the convection coefficients are unknown and variable in time, is not feasible. However, the qualitative comparison of the different measurements, or predictions (Figure 6.13), shows a good agreement in terms of the shape of the temperature evolution in time.

By selecting a convection coefficient of $h = 15$, which shows a good agreement between the model predicted temperature and the temperatures measured in the

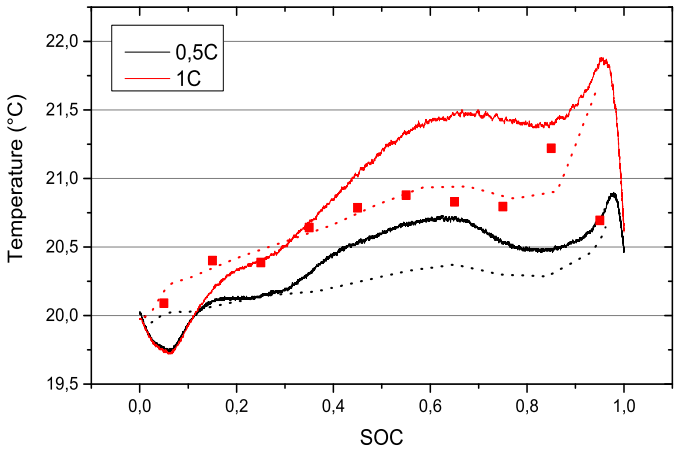

Figure 6.13: *Battery temperature under 0,5C and 1C at an ambient temperature of 20° C. Dashed lines: model results, using a convection coefficient of $h = 15$; continuous lines: temperature sensor measurements within climate chamber testing; scattered dot points: measured temperature increments within the calorimeter tests.*

calorimeter, the heat generation rate predictions and the calorimetric measurements for 1C charge processes are compared in Figure 6.14.

A very good agreement of the heat generation rates can be observed for the CC charge at 0°C and 20°C, whereas at 40°C, higher model imprecision can be attributed to the lack of experimental data at higher temperatures than 40°C.

6.3 Local Cooling for Battery Life-Enhancement

In this section, the effects of a local cooling action in the battery current tabs are studied through the execution of the derived simulation model and by the application of a localized constant cooling power in the 3D battery domain. The local cooling power is applied as a constant power, up to 0,5W, in the zone corresponding to the current tabs during the fast charge of the battery.

First, and as expected, the first effect of a local cooling power applied in the current collector tabs consists of a locally lower temperature in those regions, as shown in Figure 6.15.

However, this local temperature differences derive other effects on the electrochemical processes. As explained in section 6.1.1, in general, the regions that are near the current collector tabs tend to generate higher electrochemical current rates,

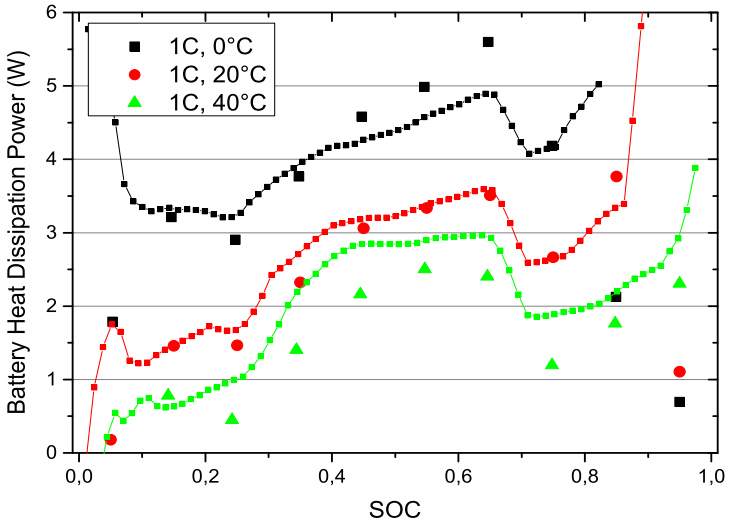

Figure 6.14: *Comparison of the battery model heat generation rate predictions (scatter and line) with the calorimetric experimental data (scatter points) for 1C-rate charging processes at different ambient temperatures.*

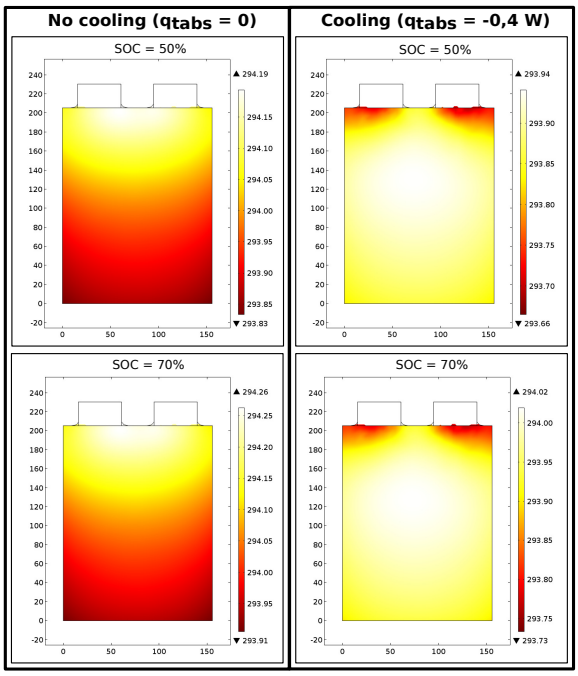

Figure 6.15: *Surface plot of the temperature distribution of the battery model and the effects of the application of a local cooling power at the battery current tabs.*

due to a higher electrical potential and a higher temperature because of concentrated ohmic losses. This effect is only counterbalanced when a sufficient SOC surface difference is achieved and the electrochemical conductivity, Y_{ec}, decreases monotonically.

However, and as it can be seen in Figure 6.16, the distribution of J is also highly dependent on the temperature. In this figure, it can be seen that the transition of the current density location from the regions next to the current tabs to the regions on the bottom of the battery, which appears at around 75% SOC (undergoing 1C charge simulations), is smoothed when a local cooling power is applied to the battery tabs, as a consequence of a lower temperature near the tabs.

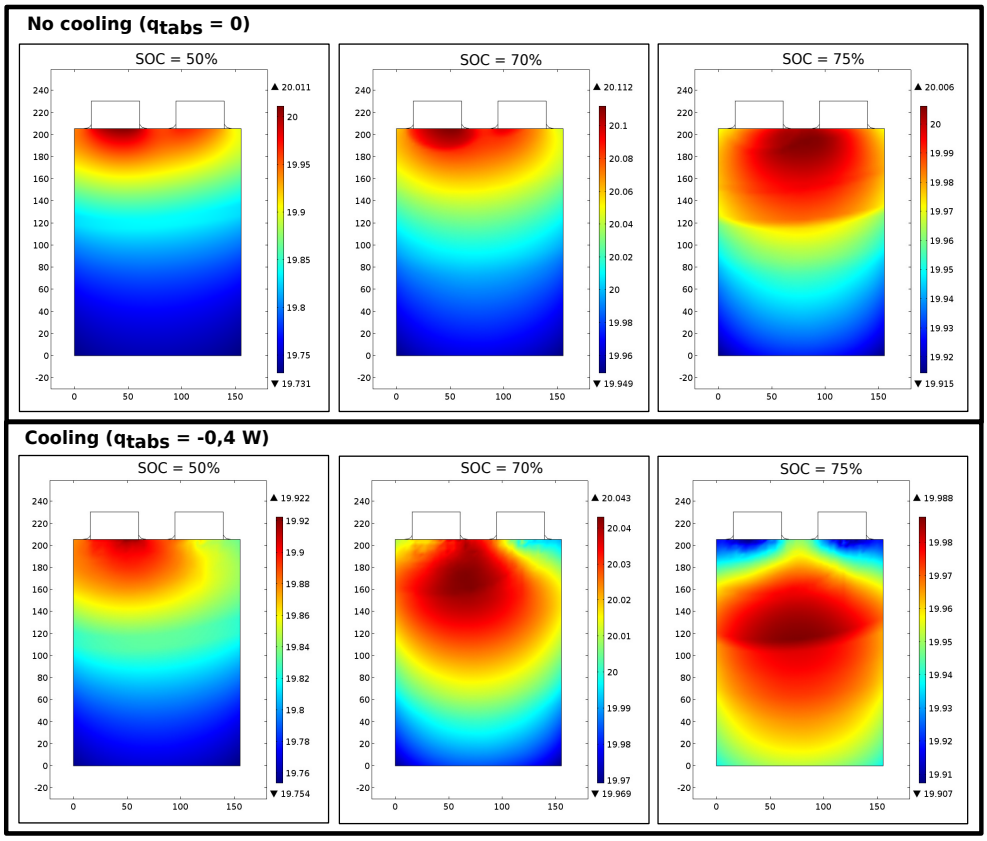

Figure 6.16: *Plot of the evolution of the model current density surface distribution, and effects of the local cooling power for a 1C-rate fast charging process.*

As a consequence, and recalling that the SOC model distribution (equation 5.11) is based on the distribution of the electrochemical current density, J, and its evolution in time, it arises the observation that the cell SOC distribution homogeneity can be improved by the introduction of some local cooling power near the current

collector tabs. This is demonstrated by the numerical results, and depicted in Figure 6.17, where the maximum and minimum SOC cell surface values are shown for different local cooling power values, under a 1C-rate fast charging process.

Hence, maximizing SOC homogeneity might imply the enforcement of some temperature inhomogeneities, which might counteract the inhomogeneity of the current collectors overpotential distribution. In this sense, the analysis of the local cooling on the effects of battery heat generation has also been experimentally investigated by Bazinski et al. in [125].

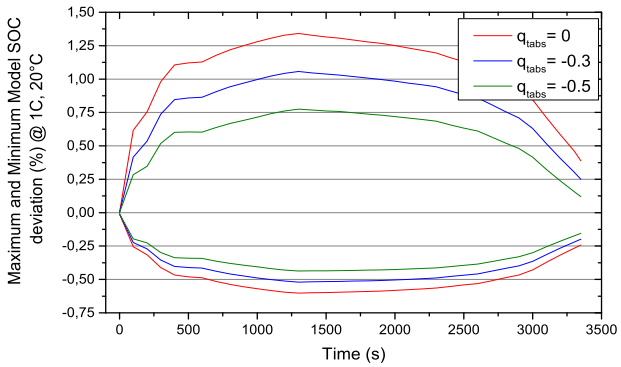

Figure 6.17: *Plot of the model maximum and minimum SOC cell surface values during a simulation of a 1C-rate fast charging process, subject to variable battery tab cooling magnitudes.*

Note that, as shown in Figure 6.18, the effect of a moderate local cooling near the current collector tabs region might as well imply an improvement in the overall battery temperature homogeneity, accounted as the difference between the maximum and the minimum cell surface temperatures.

By looking at the two previous figures, it can be seen that the SOC homogeneity improves from 0 to 0,5W of local cooling power, in an approximately linear fashion. On the other side, the best overall temperature homogeneity is observed at $q_{tabs} = 0,3\text{W}$, as compared to $q_{tabs} = 0\text{W}$ and $q_{tabs} = 0,5\text{W}$. This enlightens that increasing the local cooling action downgrades the homogeneity of the temperature, after a certain local cooling value.

Here it is worthwhile to explain that, even if in this work the effects of temperature on battery degradation have been explained and reviewed in much greater detail (section 2.3) than those of the operating current, in most of lithium-ion battery chemistries the influence of both factors can be of similar orders of magnitude

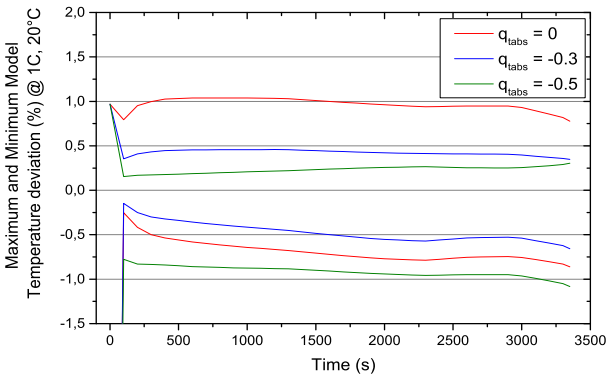

Figure 6.18: *Plot of the model maximum and minimum cell surface temperature deviations (from the average temperature) during a simulation of a 1C-rate fast charging process, subject to variable battery tab cooling magnitudes.*

[40, 33].

Therefore, and since the homogeneity of the SOC is clearly a sign of the uniformity of the electrochemical activity, the model results show that an equilibrium between temperature and SOC homogeneity might exist in order to optimize the battery performance and to minimize its degradation.

Regardless of more insights into the influence on the degradation, and as a conclusion for this section, it can be stated that the model results point out that the effect of a moderate local cooling power in the current tabs region can be beneficial for the homogeneity of both the electrochemical activity rates and the overall battery temperature. Last but not least, note that this conclusion differs slightly from the guidelines that are given in most of the literature related to the design of the BTMS for battery pack life-enhancement, where the battery temperature homogeneity is in most cases the only objective pursued [39, 33].

Chapter 7

BTMS Concept Design

The thermal issues are one of the main barriers of the mass deployment of lithium-ion power batteries. This problem is assessed from two different technical branches, from which several publications have appeared in the last few years:

1. The first seeks to reduce some of the thermal issues as a result of the modification of the internal materials. This includes the study of the effects of doping or coating the active materials through different techniques [127], the reduction of the electrodes particle size (which intends to reduce the diffusion distances of the lithium ions) [128], or the study of new anode materials with better thermal properties [129].

2. The second provided that lithium-ion batteries may be manufactured without considering the thermal performance and investigates the usage of different thermal conditioning strategies for the development of the most efficient, compact, cheap and secure battery thermal management system (BTMS) design.

The first of the above listed points being essential for the development of future and improved lithium-ion cells, the development and dimensioning of a customized BTMS is one of the most important steps in the development and design of large battery packs for applications such as BEVs, HEVs, or energy storage systems, where high electric power is used in relatively short periods.

In this regard, this chapter gathers, first, a brief review on existing technology, solutions and research directions for the development of lithium-ion BTMS (section 7.1). After this review, a novel BTMS design for the battery box of a BEV is presented and described in section 7.2.

7.1 State-of-the-Art of BTMS

The narrow desirable operating temperature range that lithium-ion batteries demand for an optimal performance, the high effect that the temperature has on its performance and the complex prediction of the battery heat generation rates pose a significant engineering challenge on the development of an appropriate and efficient BTMS.

As extensively justified by the literature review presented in section 2.3, the main objectives for the design of an optimal BTMS system can be stated to be: first, to maintain the battery temperature within the appropriate temperature range, which is usually between 20°C and 40°C; and second, to minimize the maximum temperature difference across the different batteries within the pack.

In this section, a brief review on the existing solutions and on the research directions and methodologies for the design of thermal management for high density power battery modules and packs for BEVs and HEVs is given. Different approaches can be found in the literature and a number of acclimatisation systems show interesting potential for its application in BTMS. In the short review presented hereafter, some interesting and promising cooling systems might have been overlooked. Only the most common systems are covered, including forced convection (both air and liquid cooling systems) and phase-change materials or devices (heat pipes and phase change materials).

7.1.1 Convective Cooling

Air Cooling

The use of air may be the simplest approach for the BTMS, and was the selected methodology adopted for the first HEVs in the market: the Insight (2000) and the Prius (2001). In most of the cases, in BEVs and HEVs, the high energy and power density of the battery pack forces the adoption of forced convection systems, since natural air convection does not provide sufficient thermal dissipation.

Usually, the conditioned air for the BTMS is supplied from the cabin and exhausted to the ambient [39]. The air flow is normally conducted through the stack of the battery pack, or module in a parallel fashion (see Figure 7.1). CFD simulation is used in several works to optimize both the geometrical arrangement of the batteries and the flow rate for a maximum energy efficiency [18, 19]. Besides, complex systems have been investigated, such as two-directional flow configurations or systems that involve variable flow paths by recursively reciprocating the air flow direction, such as the one presented by Yu et al. in [17].

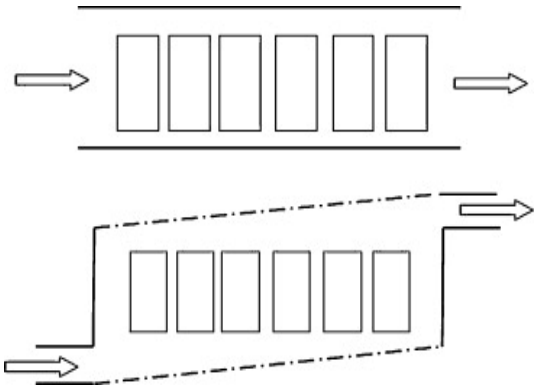

Figure 7.1: *Scheme of a typical configuration for air convective cooling over the battery pack. Figure reprinted from [39].*

However, air cooling is nowadays often discarded for the BTMS of large battery packs due to its limited dissipation capabilities, owing to the fear of the hazardous effects of a possible thermal runaway and to the acknowledgement of the importance of the temperature homogeneity on the life and performance of the battery pack.

Liquid Cooling

Compared to air, liquid cooling works both in a convective and conductive way, since the conditioning fluid (water, glycol, acetone, or other refrigerants) has a much higher heat capacity. On the other side, liquid cooling generally involves a much complex circulatory system with higher price and technical requirements. Besides, caution is crucial when using ionically conductive fluids, since they decompose when in contact with both electrodes of the battery forming hydrogen gas which, eventually, can lead to an explosion.

Therefore, the BTMS using liquid cooling is normally materialized by the design of a tubing system that circulates the refrigerant around the different battery modules, such as the design developed in [20], where the tubing design is optimized based on 3D numerical simulations. Nonetheless, similar parallel flow configurations as in the air cooled systems have also been investigated, i.e., in [21], who studied the effect of the channel's size and configuration for both pouch and cylindrical battery modules. When it comes to the actual application, Tesla, e.g., makes use of a liquid cooling system based on a ribbon shaped metallic cooling tube that stretches through the pack of cylindrical cells.

Besides, a lot of attention has lately been paid to the so-called cold plate concept, which consists of a plate with embedded mini-channels through which the

refrigerant circulates [7]. Systems including such elements have also been adopted in the industry, i.e., in the battery pack of the Volt (2011) plug-in hybrid electric, or the i3 BEV (2013), which uses the same coolant for the BTMS as for the cabin conditioning.

7.1.2 Phase Change Methods

Heat Pipes

Thanks to their extremely high thermal conductivity, which can reach up to 10^5 $\mathrm{W\,m^{-1}\,K^{-1}}$, these devices have been widely employed in electronic cooling systems, such as laptops, and have centered more attention in the recent years on their application in large battery packs. With even higher heat transfer capabilities than liquid cooled systems, heat pipes have the advantage of being a passive elements whereas its versatility is generally minor. Copper and aluminium being the most common materials for the manufacturing of the heat pipe envelope, and water and ammonia the usually employed fluids, one of the most important aspects in the design in such cooling systems relies on the thermal contact between the pipes themselves and the heating or cooling surfaces. Normally, thermally conductive plates are introduced on the hot side to enhance the contact between the heat sources and the heat pipe, and a liquid or air cooled heat sink is attached to the cold side of the heat pipes [130].

A lot of different heat pipe devices are available on the market and have been investigated for the application in BTMS. For example, a BTMS design based on pulsating heat pipes (PHP), which do not require a wick internal structure and, hence, are cheaper to built, have been presented in [131]. Besides, flat heat pipes (also known as vapor chambers) can also be manufactured, and due to their similar characteristics to the previously introduced cold plates with liquid mini-channels, their adoption for promoting temperature homogeneity has also been experimentally investigated for BTMS in [22, 132].

Most of the studies for BTMS which include heat pipes are experimental, because considering accurately the transient thermal characteristics of a heat pipe is challenging due to the complexity of appropriate modelling of the physic phenomena occurring inside the heat pipes and its thermal transfer characteristics [24, 22, 25].

PCM

A phase-change material (PCM) is a substance that has a high fusion heat coefficient, which when melting and solidification occurs (at a specific, selectable temperature),

is capable of storing and releasing large amounts of energy. The most common BTMS assembly consists in placing the battery module in a liquid/solid PCM, such as it can be observed in Figure 7.2, and the study of such assemblies is today an active area of research due to its promising characteristics: PCM cooling is a passive and compact method with proper cooling effects, can be used as thermal energy storage, and possess very good safety properties [26, 27].

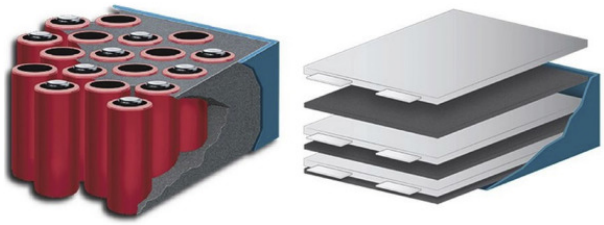

Figure 7.2: *Schematic of the most common PCM cooling system architectures for lithium-ion battery packs. Figure reprinted from [7].*

Nonetheless, some drawbacks have also been acknowledged, such as their bad thermal conductivity (which, i.e., would complicate the pack warming that is necessary in cold environments extremely) and the volume change and capillary forces that arise when the PCMs melt [7, 26].

The most commonly studied PCM for lithium-ion battery cooling is paraffin wax, in which composite metal matrices are normally introduced in order to enhance its bad thermal conductivity [27].

7.2 Concept Design

Once the most common BTMS systems and simulation studies have been reviewed, and recalling that one of the main objectives of the project under which this work is contextualized is the development of a novel and energy efficient climate system for electrical vehicles, an innovative acclimatization system concept is presented in this section. The presented system design arises from the project guidelines, which specify that the application and combination of Joule and thermoelectric elements has to be studied in order to redesign and to improve the existing thermal systems both for the car interior cabin and for the battery pack thermal conditioning.

The creative phase and the necessary discussion that came through the design process of the configuration of the battery thermal management system (BTMS) that is presented hereafter is kept out of the present work. Conversely, only the final design is presented and described here, explaining its working principles and

characteristics, and briefly comparing it to the existing technologies that have been previously reviewed.

7.2.1 Battery Box

The battery pack for the EV application that is studied in this project has a nominal energy of 34, 6kWh and a nominal voltage of 340V and, as it can be observed in Figure 7.3, it is divided into 7 battery modules. Each of the battery modules is conformed by 75 battery units connected in a 5P15S[1] array, which have an energy capacity of 100Ah and a nominal energy of 4, 8kWh at 48V. Every battery module is conformed by five sub-modules connected in series, each of which consists of a 5P3S battery array (100Ah, 9, 6V).

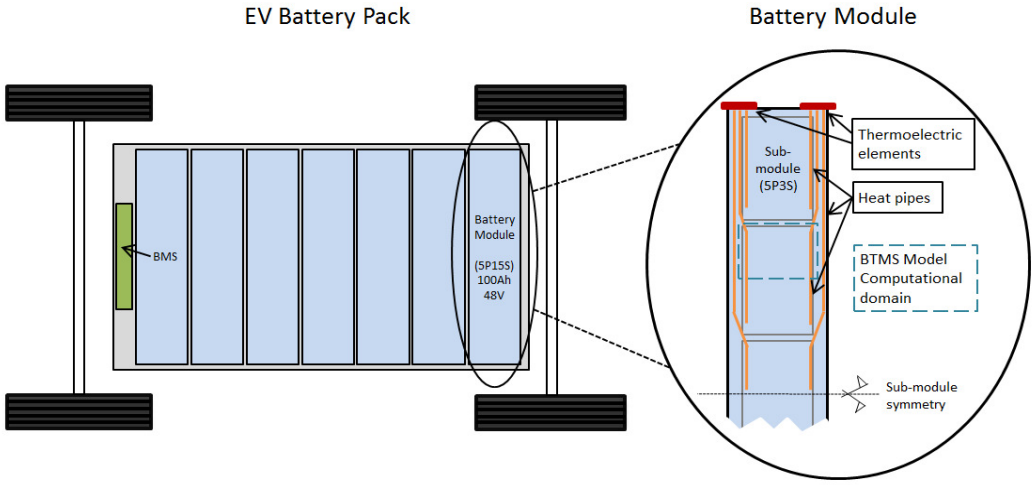

Figure 7.3: *Scheme of the battery pack box distribution and BTMS design.*

The 15 pouch batteries conforming every sub-module are placed one after another separated by a thin metallic fin, and are pressurized from both ends, where a thicker metallic fin is placed. A gauge pressure of 10psi is set by the manufacturer as the optimal working pressure. The pressure is applied by the use of some metallic stripes that enclose the battery sub-module and which are designed to maintain the pressure almost constant independent of the battery expansion (which can reach up to 5% of the original thickness during the whole operation life of the batteries).

[1]5P15S is the short form for referring to a 5 parallel - 15 series battery connection (consisting of a total of 5*15=75 batteries)

7.2.2 Thermal Management System

The metallic fins that are placed in between every battery unit conforming the battery sub-modules serve as a thermal conductor, in order to promote the temperature homogeneity among the batteries surface plane and to facilitate the rejection of the heat that each of the batteries generate during its operation. As it can be observed in Figure 7.4, the metallic fins are bended at the lateral part of the sub-module to improve the thermal contact with the lateral heat distribution plate and the heat pipes that transport the heat energy from the batteries to the exterior of the battery box, or vice versa. However, and as depicted in Figure 7.3, between the heat pipes and the exterior of the battery box (which is properly thermally-insulated from the exterior), a set of thermoelectric devices is placed in order to control the heat flux coming in (or going out) of the pack.

Thus, note that the system to control the temperature of the batteries and, hence, the heat fluxes from the inner to the outer part of the battery box, integrate a serial combination of heat pipes and thermoelectric devices.

The BTMS design proposal, a sketch of which is depicted in Figure 7.4, is similar to the novel cooling system design that is presented in [133], where Saengchandr et al. studied and simulated a system based on the combination of a heat pipe's array with thermoelectric modules. In that case, the cooling system objective was the thermal control of a computer microchip, and it was concluded that the proposed system was more efficient than a system based on any of its components on their own.

Cooling and Heating Modes

In order to cool down the battery pack, the Peltier thermoelectric devices (TED) are powered through a DC-DC controller to cool down the internal side (in contact with the heat pipe), while the heat that is generated by the TED operation is evacuated from the hot side throughout an external heat sink. Similarly, when the battery needs to be heated up, the TED are powered inversely, generating a hot temperature in the inner side (inside the battery box) that creates a heat flow rate that, conducted through the heat pipes and the aluminium fins, heats the batteries up to the desired operating temperature.

Sleeping Mode

The TED are known to have a bad cooling performance (or COP), and this is the major reason that has limited its application for BTMS [39]. Moreover, a bad

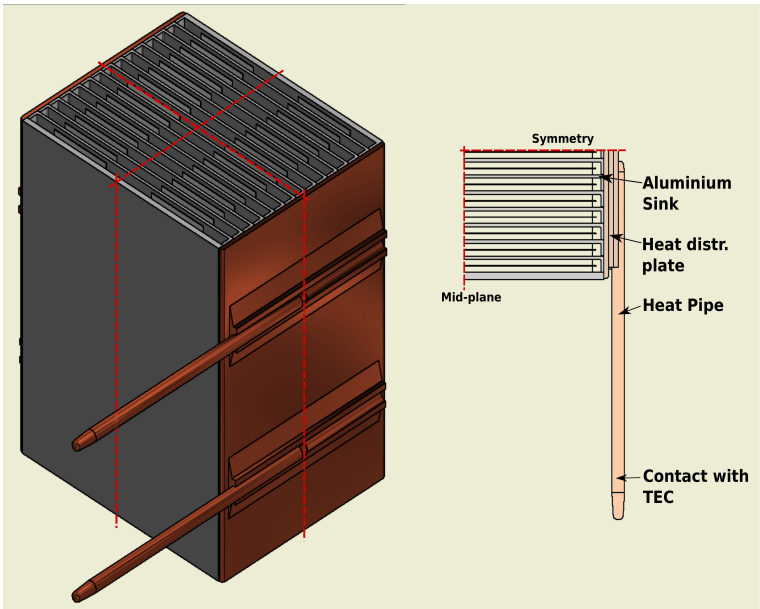

Figure 7.4: *Scheme of the thermal management design of one battery sub-module, including heat distribution plates between each pouch battery and the lateral area of the sub-module, and heat pipes for the heat transport to the exterior of the battery box.*

cooling efficiency translates into a rejection of a big amount of heat on the hot side, when power is supplied in order to absorb a heat flux power on the cold side.

One of the major reasons for this fact is that the effective heat conductivity through the TED is very poor, due to the low thermal conductivity of the semiconductors that conform its body (such as bismuth telluride, Bi_2Te_3) [134].

However, in the presented BTMS design, the bad thermal conductivity of the TED serves as an insulation mechanism for the resting mode, which is extremely important when the BEV is eventually parked in cold ambient. Besides, since the TED are placed on the walls of the insulated battery box, the actual design ensures that the heat production of the TED during operation cooling mode is directly rejected outside of the battery box and, thus, does not sum up to the heat generation of the batteries.

Chapter 8

BTMS Optimization

In order to optimize the geometrical configuration of the battery stack, regarding thermal aspects, a framework for linking an external optimizer to Comsol parametric models is developed here. The development of this framework permits, furthermore, the usage of any kind of optimizer which is programmed in Python or any other programming language to optimize any parametric model implemented in Comsol, and can be used for a wide variety of different applications.

8.1 BTMS Model Implementation

Making use of the experimental-based electrochemical thermal model for the pouch battery under study, described and implemented in chapter 5, a parametrized 3D configuration of the BTMS design is drawn in Comsol to simulate the performance of the system, and to evaluate the influence of each of the design parameters.

In the following sections, the simplifications that have been adopted in order to simplify the BTMS model will be presented first (section 8.1.1). Then, the thermoelectric devices (TEDs) and the heat pipe models implementation, caused through the imposition of some boundary conditions, are explained in section 8.1.2. Finally, the concrete targets of the optimal design of the BTMS are explained in section 8.1.3.

8.1.1 Domain Definition

Simplifications and Assumptions

Since all the walls of the battery box depicted in Figure 7.3 are properly insulated, and since all the batteries always operate under the same load and thermal condi-

tions, a negligible heat flux can be expected to flow in between the different battery sub-modules. This allows for the simplification of the simulation domain, from the whole battery box to a single battery sub-module. Besides, and as shown in Figure 7.4, every battery sub-module conformed of 15 batteries is symmetric along the z-axis (the axis across the pouch cells). This permits a further simplification of the computational domain to just the half of the battery sub-module.

Due to these simplifications, the boundary conditions of the model are set to thermal insulation on all the boundaries, with the only exception of the surface boundary that is in contact with the TEDs.

Since the temperature differences across the simulated battery sub-module are not expected to be very big, and because of the necessity of simplification due to the high computational cost that requires every 2D electrochemical-thermal cell sub-model, all the batteries in this model are considered to be operating under the same conditions (temperature, current and SOC).

This is done by the use of the same simple mapping function that was used in the battery model, φ_{2d-3d} (recall expression 5.17).

Model Parameters

The definition of the BTMS model geometry, presented in the previous section 7.2.2, relies in its implementation in Comsol on the parameters that are gathered in Figure 8.1.

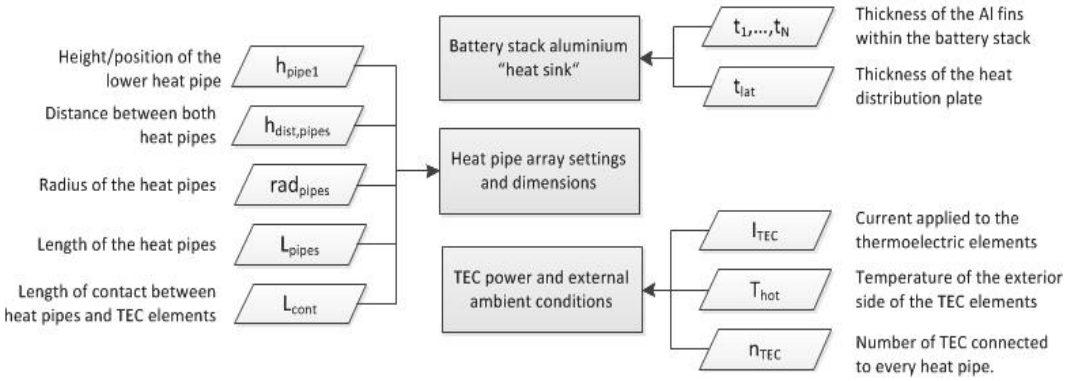

Figure 8.1: *Sketch of the BTMS model parameters.*

By varying these parameters, the optimal design for the presented BTMS design configuration is sought as the final objective.

8.1.2 Thermal Management Elements

Thermoelectric Devices

A thermoelectric device (TED) is an element that makes use of the thermoelectric effects, namely the Peltier, Thomson, and Seebeck effects, which govern the temperature gradients that are caused due to electrical potential difference between dissimilar metals, or vice versa. For that reason, TED can typically be used for both, heating and cooling purposes, as well as for power generation (from thermal to electrical power).

A typical cutaway of a TED is presented in Figure 8.2.

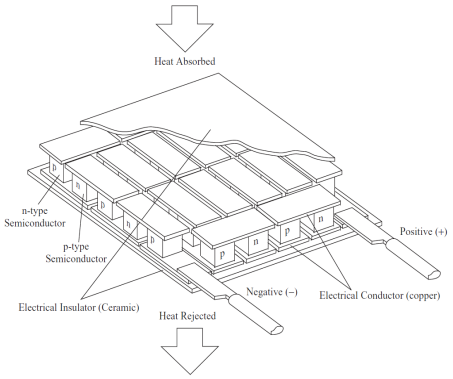

Figure 8.2: *Typical cutaway of a Peltier Module. Figure reprinted from [135].*

Modeling the TED in Finite Elements from the governing equations of the thermoelectric effects (the derivation of which can be found, i.e., in [136]) shows the main inconvenience that is to be solved for the 2D or 3D solution within a complicated internal geometry (and its associated complicated mesh), as depicted in Figure 8.2.

Due to that, and given that the concrete TED sample that is going to be adopted for the current BTMS design is provided by a project partner, the TED is replaced in the numerical simulation model by a surface boundary condition. This condition, applied to the outer end of the heat pipes, governs the heat flux that the Peltier element rejects from the system (see the left plot in Figure 8.3).

The surface of the chosen TED measures 30×42mm, and the thickness of the devices 3mm. As we can see in Figure 8.3, the cooling capacity $Q_{c,TED}$ and the operating voltage U_{TED} of the TED sample have been tested by the manufacturer at different hot side temperatures, T_h, and are linearly dependent on the temperature differences between the cold and the hot sides of the TED, $T_h - T_c$.

Thus, given the data shown in Figure 8.3, a Neumann boundary condition is applied to the surface of the heat pipes which are in contact with the TEDs. On

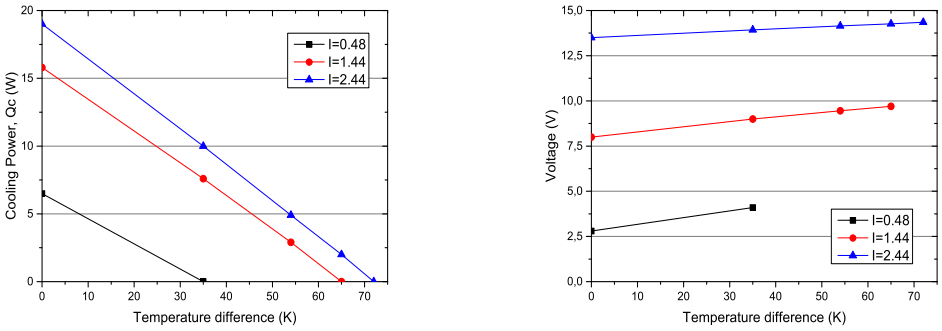

Figure 8.3: *Plot of the main empirical characteristics of the thermoelectric element sample, adopted for the BTMS.*

the other side, the heat rejection on the hot side of the TED is computed as

$$Q_h = Q_{c,TED}(I_{TED}, T_c, T_h) + I_{TED}U_{TED}(I_{TED}, T_c, T_h) \tag{8.1}$$

where the TED current and the hot side temperatures, I_{TED} and T_h, are model parameters, and the cold side temperature of the TED, T_c, is governed by the thermal energy conservation equations that are solved along all the batteries, aluminum case and heat pipes array.

Heat Pipe

Using a lumped thermal resistance network model,which is a common engineering strategy for characterizing the different heat transfer phenomena ocurring within a heat pipe, the overall thermal resistance of the heat pipe can be written as [130]

$$\kappa_{eq} = -\mathbf{q}\frac{L_{eq}}{\Delta T} = \frac{L_{eq}}{R_{eq}A_{eq}} \tag{8.2}$$

where $A_{eq} = \pi \varnothing_{pipe}/4$ is the cross sectional area, and L_{eq} is the effective length of the heat pipe, corresponding to

$$L_{eq} = \frac{L_{evap}}{2} + L_{ad} + \frac{L_{cond}}{2} \tag{8.3}$$

and being L_{evap} the length of the evaporation section, L_{ad} the length of the adiabatic section, and L_{cond} the condensation section length.

The overall resistance of the heat pipe, R_{eq}, is normally presented in the literature as a combination of serial and parallel thermal resistances [137, 138], as shown in Figure 8.4, which can in general be modeled as

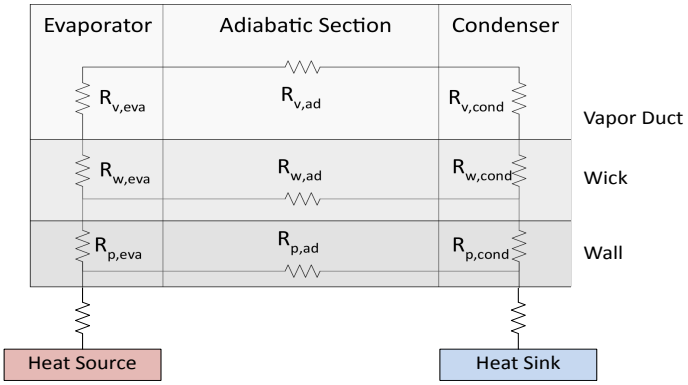

Figure 8.4: *Thermal network scheme of the heat pipe equivalent thermal characteristics.*

$$R_{radial} = \frac{\ln\left(r_{ext}/r_{int}\right)}{2\pi\kappa L}; \qquad R_{axial} = \frac{L}{\kappa A} \tag{8.4}$$

where r_{ext} and r_{int} are the external radius, and L and A are the length and cross-sectional area of every zone.

Most of the thermal resistances depicted in Figure 8.4 can be computed by the use of the equations in 8.4 and the use of tabulated material properties of the wall (copper or aluminum) and the working fluid (water or ammonia). In the case of the wick structure, different expressions appear in the literature for computing its effective thermal conductivity due to the existence of different wick structure types. E.g., in [139], Ferrandi et al. present different correlations for wrapped screen and sintered wick heat pipes; in [140] further models are presented. The most common expression for the effective thermal conductivity of the liquid-wick structure is the expression, derived by Zuo and Faghri [141], which can be written as:

$$\kappa_{eq,wick} = \frac{\kappa_l\left((\kappa_l + \kappa_w) - (1-\varepsilon)(\kappa_l - \kappa_w)\right)}{\left((\kappa_l + \kappa_w) + (1-\varepsilon)(\kappa_l - \kappa_w)\right)} \tag{8.5}$$

where κ_l and κ_w are the thermal conductivity of the working fluid and the envelope metallic material, and ε is the porosity of the wick structure.

The thermal resistance of the vapor flow is determined by

$$R_v = \frac{T_v(P_{v,eva} - P_{v,cond})}{\rho_v h_{fg}\mathbf{q}} \tag{8.6}$$

where $P_{v,eva}$ and $P_{v,cond}$ are the saturation vapor pressures at a corresponding vapor temperature at the evaporator and condenser, respectively, and whose values are introduced to the model within a look-up table.

Thus, at the end, the heat pipe is modeled in the BTMS model in Comsol as a solid. It has a variable thermal conductivity, κ_{eq}, which is computed from equation 8.2 and the results of the thermal resistances given in equations 8.4, 8.5 and 8.6. The material properties that are needed for computing each of the thermal resistances are adopted from [137], which are invoked as a function of the model temperature solution at every time step. In this regard, it has been observed that the thermal conductivity of the heat pipe has to be defined as a *variable* instead of a *parameter*, since Comsol permits the *variables* definition to depend on time and on the existing dependent variables that the governing equations are solving for [147].

External Heat Dissipation

The presented BTMS concept design might release a considerable amount of thermal energy to the outer part of the battery box when the TED are powered in cooling mode. The heat dissipation on the hot (external) side of the TED results as the sum of the sum of the battery heat dissipation power plus the thermal energy released because of the TED operation. The appropriate temperature control and, thus, the heat rejection of the outer surface of the TEDs is very important for the performance of the cooling mode: if the outer surface of the TED gets hot, its cooling performance decreases considerably, and linearly (see Figure 8.3).

However, the thermal treatment of the external side of the battery box can be very complex in itself, since it may involve different solutions and strategies for permitting, i.e., the option of using the dissipated thermal energy to warm the car cabin, if it is required.

Therefore, the treatment of the external side of the BTMS is simplified at this stage, and a further development of the model is kept open for this side. Finally, the simplest approach possible is adopted in the model, setting the external temperature to a fixed ambient value. This is done through the application of a Dirichlet boundary condition, assuming an infinite thermal dissipation on the external side of the Peltier elements.

8.1.3 BTMS Targets

The key question regarding *optimal design* is the right measure of what makes a design good and desirable. Before looking for optimal designs it is important to identify characteristics that contribute the most to the overall value of the design. Therefore, this section focuses on the description of the objectives and load cases that have been set for evaluating the design of the BTMS.

Multiple Objectives

One of the most complex tasks within the present optimization process is the correct definition of the objective that the optimal BTMS design ought to accomplish, because different objectives and a variety of load cases have to be involved. Nonetheless, a clear definition of the multiple objectives that the BTMS has to fulfill, or meet, is possible:

1. First of all, and as stated as the first priority in all the works that discuss the design of BTMS, the battery temperature has to be maintained within the appropriate temperature range. This translates into different objectives. Basically, $T_{batt,max}$ has to be minimized during operation at hot ambient conditions, and the heating mode has to increase $T_{batt,avg}$ as fast as possible in the case of battery pre-heating after parking in cold ambient.

2. Besides, the battery temperature and SOC homogeneity have to be maximized, by minimizing $(T_{batt,max} - T_{batt,min})$ and $(SOC_{batt,max} - SOC_{batt,min})$, as the temperature and the cycling DOD have shown to affect the degradation of the electrochemical cells, and non-uniform degradation causes electrical imbalance and bad battery performance.

Apart from the two major objectives presented above, the energy efficiency ought to be maximized, both in cooling and heating modes. In this concern, the energy efficiency can be quantitatively evaluated by computing the coefficient of performance (COP), which can be written during cooling phases as

$$COP_{cooling} = \frac{Q_{cold}}{Q_{hot} - Q_{cold}} \tag{8.7}$$

where, for the given system, Q_{cold} is the rejected heat from the batteries and Q_{hot} is the heat that is rejected outside the battery box from the external (hot) side of the TEDs. In the case of heating conditions, which can become necessary if the car is parked or operated in cold ambient, the COP can alternatively be computed by

$$COP_{heating} = \frac{Q_{hot}}{Q_{cold} - Q_{hot}} \tag{8.8}$$

Last but not least, the weight and the cost of the BTMS components and manufacturing process have to be minimized. In the case of weight, this is rather easy to evaluate, since it is clearly the aluminium case holding the batteries which is responsible for their heavy weight. The manufacturing costs, however, are more

difficult to evaluate. Thus, this objective is kept out of the optimization routine at this preliminary stage of the BTMS development.

Load Cases

The most important load case corresponds to the fast charge process, as it was already introduced in the section on the objectives of the battery electrochemical model (section 5.1.1). Nevertheless, the BTMS heating mode, by the inverse power supply on the TED, also represents a relevant load case for the evaluation of the system, since this practise might be highly necessary in countries with cold ambient temperatures.

The evaluation of the BTMS design objectives for the "pre-heating" load case would clearly differ from the objectives of the fast charging case (i.e., the average battery temperature has to be maximized in this case). However, the same evaluation data sets can be used, while only the objective function expression has to be modified.

Last but not least, studying the "sleeping" mode is necessary for evaluating the overall performance and characteristics of the BTMS, and would give information on the insulation efficiency of the BTMS. However, and as mentioned, the success of the sleeping mode relies mostly on the thermal insulation of the battery box walls, rather than on the parameters that govern the battery stack geometry. Therefore, this load case cannot be studied together with the two stated above.

8.2 BTMS Model Results

In order to explore the effects that the different model parameters generate in the different objective functions, defined in the previous section, several parametric sweep simulations have been executed.

Whereas simulations for the pre-heating case have also been run, the result of such is not included in this work due to the lack of time for the proper analysis of the results. Instead, only the simulations for galvanostatic fast charge are presented.

In order to study the 1C charge current in a computationally more efficient way, the simulation has been restricted to the interval 40% to 70% SOC, which corresponds to the SOC region in which the battery is expected to generate the highest heat rates (recall Figures 6.9 and 6.14).

8.2.1 Computational Cost

After more than 300 runs for the study of 1C charge in the interval 40%-70% SOC, the first conclusion that we can extract, analyzing the computational cost of the simulations, is that the adopted model strategy is adequate for the dimensioning and design of the BTMS.

The average computational cost for all the simulations is 196s (with a standard deviation of 0,185), while the computational time or the time of the physical process that is being simulated,which lasts the same, have a duration of 1000s.

The mesh that has been used for solving the numerical model in this chapter consists of around 26.000 elements, and is presented in Figure 8.5. Here, analogously to what was discussed in the implementation of the battery model, an hexahedral mesh is generated along the batteries and aluminium fins, whereas a tetrahedral mesh is generated for the rest of domains, which are geometrically more complex.

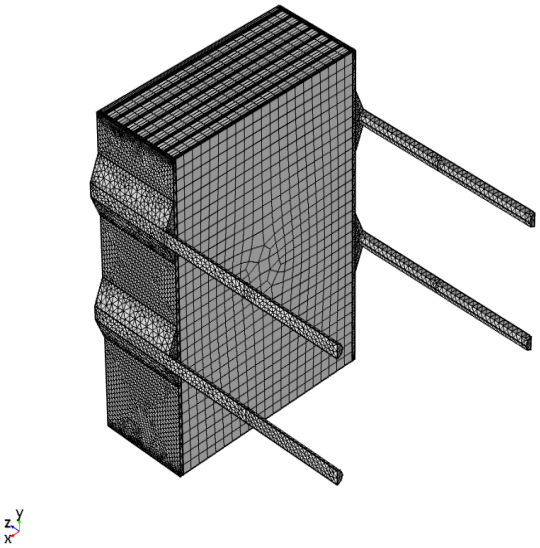

Figure 8.5: *Computational mesh and domain of the BTMS numerical model.*

8.2.2 Cooling Capabilities

The model results show that, as expected, when power is supplied at the external end of the heat pipes, a temperature difference between the two heat pipe ends of around 3-10°C develops. This temperature difference (ΔT_{pipe}) activates the phase-change transport in the heat pipes, and a heat flux along the pipes is established quickly (see Figure 8.6).

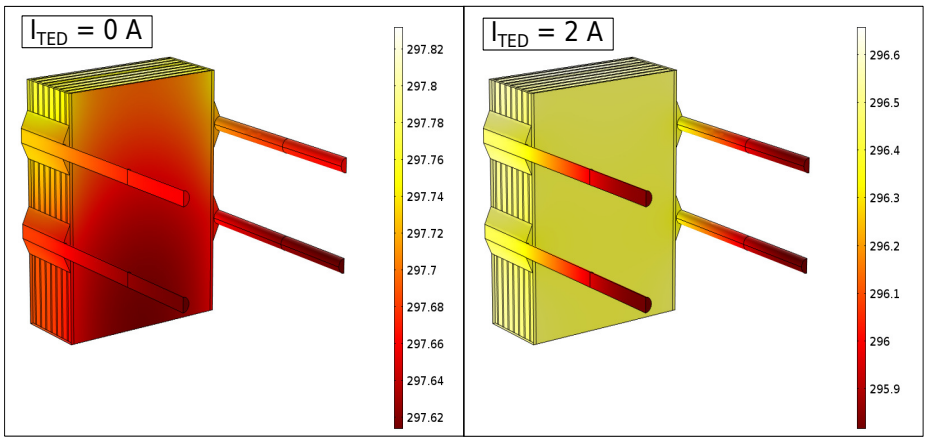

Figure 8.6: *Surface plot of the temperature at $t = 1000s$ undergoing a 1C charge at an ambient temperature of 20° C and under different TED current supply conditions.*

Besides, in the surface plots shown in Figure 8.7, the effects of the cooling power on the surface temperature distribution can be more clearly observed under the same conditions that are shown in Figure 8.6.

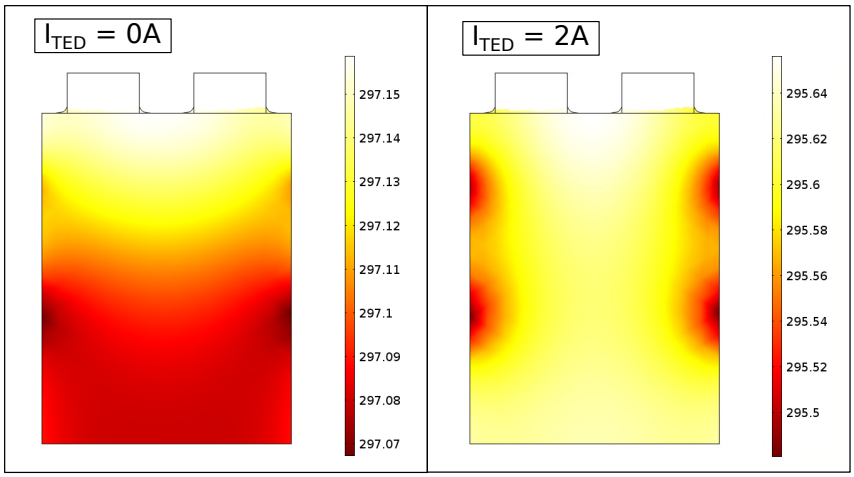

Figure 8.7: *Surface plot of the temperature at which the representative electrochemical cell is working, at $t = 1000s$ and undergoing a 1C charge at an ambient temperature of 20° C.*

As we can see in the left plot of Figure 8.8, when the 4 TEDs that are placed at every heat pipe end are powered with a current of 2A, the maximum battery temperature undergoing a 1C charge from 40% to 70% SOC (at an ambient temperature of 20°C) gets reduced from 23,6°C to 21,7°C. On the right plot, in which

the TED current is maintained at a level of 1A, it can also be observed that the effect of a higher external ambient temperature is also reflected in a lower battery temperature decrease, or a lower effective cooling power.

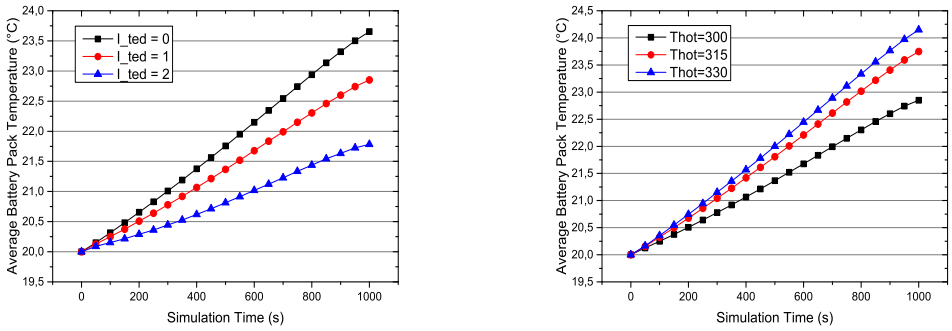

Figure 8.8: *Plot of the average temperature within the battery sub-module, subject to different cooling rates and external ambient temperature conditions.*

In the next Figure 8.9, the effects of the TED current and the external ambient temperature on the electrical power consumption of the cooling system are shown, being the electrical power consumption computed as

$$P_{elec} = 2.\left(N_{TED}.(U_{TED}.I_{TED})\right) \tag{8.9}$$

where n_{TED} is the number of TEDs that are needed for the computational domain battery module. The electrical power P_{elec} is, then, multiplied by 2 because the computational domain consists only of one half of a battery sub-module.

Note that a power supply of 2A at the four TEDs supposes a cooling power of approximately 180W. From the obtained model results, it is interesting to compare the power demand of the cooling system to the power demand that the battery charge requires. Being the battery box composed of 35 battery sub-modules, a cooling rate of 2A per TED and 180W per sub-module implies a total cooling power demand of the battery box of approximately 6kW. On the other hand, charging the battery box (of 100Ah and 345V) at a current of 1C, translates into a power demand of 34kW.

Thus, supposing that the cooling rate of 2A at every TED is powered directly from the power supply station, it would suppose an increase of about 18% of the power to the power consumption. Besides, and as it can be seen in the right plot of Figure 8.9, if the temperature of the ambient gets increased to an extreme hot temperature of 330K, the cooling power demand gets increased by 15% as compared

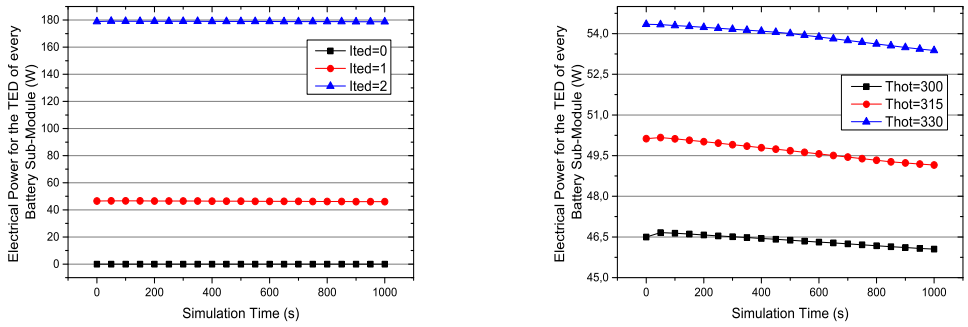

Figure 8.9: *Electrical power consumption of the TEDs of the BTMS under different cooling rates and external ambient temperature conditions.*

to the power demand at an ambient temperature of 300K.

Related to the electrical power demand from the BTMS system, in Figure 8.10 it can be observed that the cooling coefficient of performance (COP), determined in equation 8.7, is bigger when lower cooling power is administrated. On the right plot, the effect that the thickness of the lateral heat distribution plate, t_{lat}, is shown. This parameter is selected here, instead of the external temperature T_{hot}, since the effect that this thickness has on the COP value of the overall system is clearly (and interestingly) non linear, showing better results for $t_{lat} = 4,5$mm than for $t_{lat} = 3$mm or $t_{lat} = 6$mm.

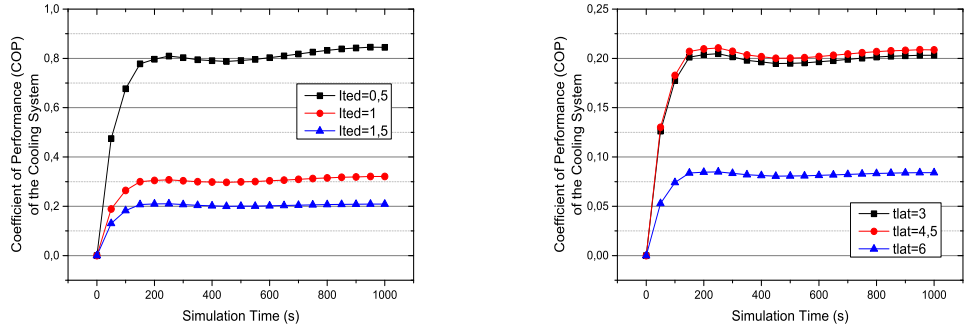

Figure 8.10: *Transient establishment of the BTMS cooling COP, under a 1C charging current rate at an ambient temperature of 20° C, plotted against different TED supply rates (left) and different values of the thickness of the lateral plate (right).*

A possible reason for the appearance of the bad COP when the lateral aluminum plate is too thick, might be the heat accumulation of the aluminum. Thus, the COP

may decrease due to the higher volume of the aluminum. A similar phenomenon can be witnessed in the case of the thickness of the aluminum plates that are placed between every battery, determined by $t_1, \ldots, t_N$.

8.2.3 Effect of the Model Parameters

Some representative graphs are selected in this section to show the influence of some design parameters in the evaluation of the objective functions corresponding to the temperature and SOC homogeneity.

First, and qualitatively, in the isothermal contour plots presented in Figure 8.11 it can be observed that the temperature homogeneity of the battery pack is improved when the lateral heat distribution plate thickness gets increased.

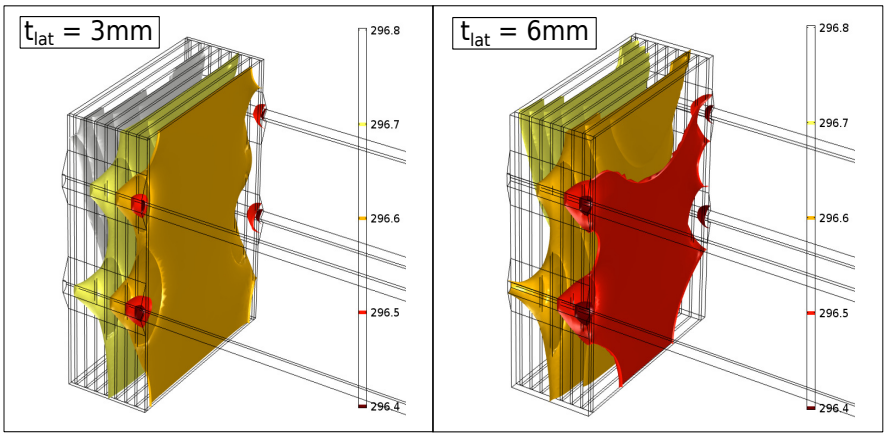

Figure 8.11: *Isothermal contour plot of the BTMS undergoing a 1C charging current rate at an ambient temperature of 20° C, and with a current supply to the TED of 1,5s*A

Besides, Figure 8.12 shows that the heat pipe distance has only a faint repercussion on the temperature and temperature distribution of the sub-module battery stack. However, as the heat pipe length increases, the temperature drop along the heat pipe, ΔT_{pipe}, increases rapidly, as well.

Note that a too high temperature drop along the heat pipe length can compromise the effective operation of the heat pipe, as it is discussed in [88], because the heat pipe might reach the so-called *capillary limit*, which results as a consequence of a too high pressure drop between the evaporator and the condenser sections [137]. Although, this issue can be easily solved by increasing the radius or the number of heat pipes.

In a quantitative manner, in the next Figures 8.13, 8.14 and 8.15, the influences of

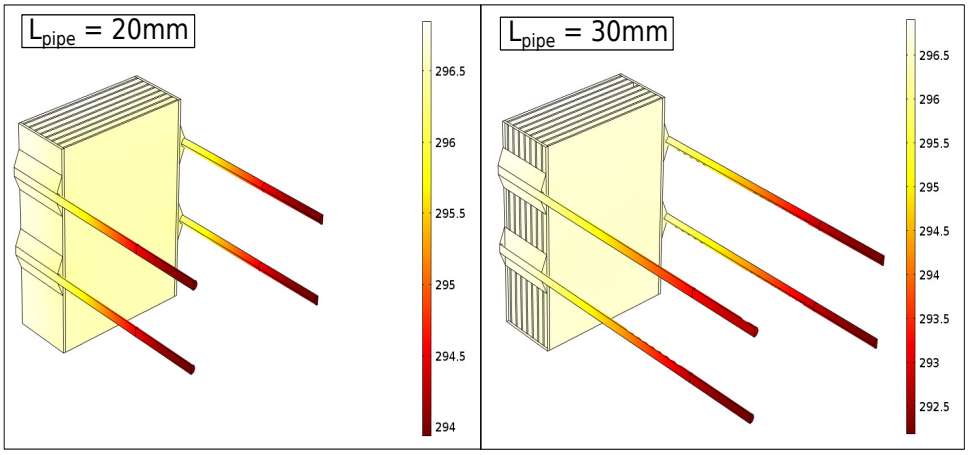

Figure 8.12: *Surface plot of the temperature at $t = 1000s$ undergoing a 1C charge at an ambient temperature of 20° C and with different heat pipe length model values.*

some design parameters on the maximum temperature and SOC differences across the battery module are reflected. More precisely, the heat pipe length and their radius, L_{pipe} and r_{pipe}, are the parameters whose influence is shown, as well as the external ambient temperature. The selection of showing the graphs for these design parameters, instead of any others, is completely arbitrary.

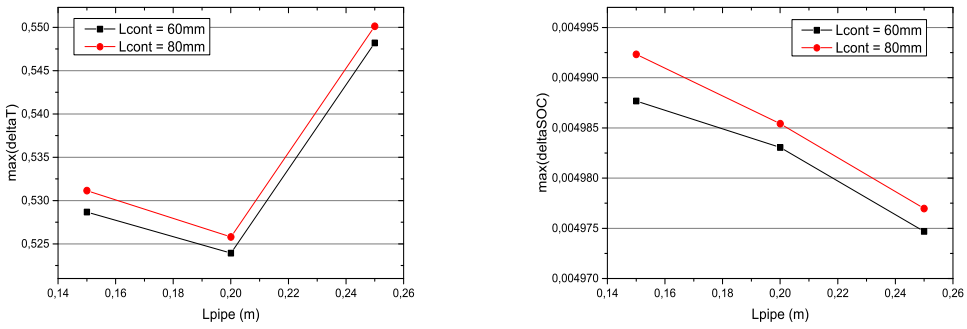

Figure 8.13: *Influence of the heat pipe length, L_{pipe}, on the maximum temperature (left) and SOC (right) gradients across the battery sub-module for the presented BTMS concept design.*

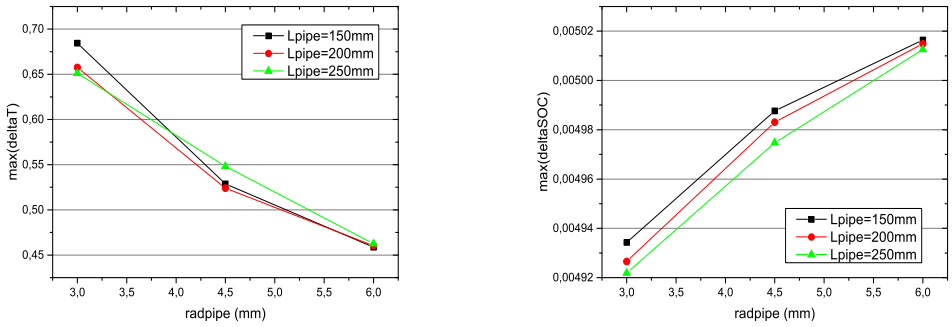

Figure 8.14: *Influence of the heat pipe radius, r_{pipe}, on the maximum temperature (left) and SOC (right) gradients across the battery sub-module for the presented BTMS concept design.*

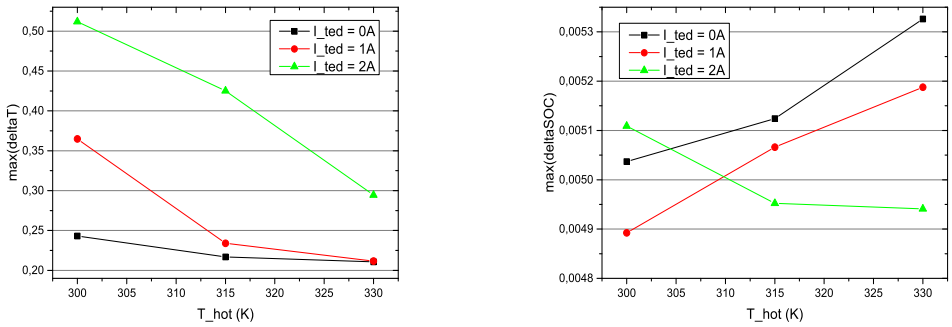

Figure 8.15: *Influence of the external ambient temperature, T_{hot}, on the maximum temperature (left) and SOC (right) gradients across the battery sub-module for the presented BTMS concept design.*

8.3 Optimization Framework

Given that the optimization of several design parameters under different load cases is pursued, and since the evaluation of the influence of the different BTMS design parameters has shown (previous section) to be complex, in terms of the "fitness function", it has been concluded that an optimization framework has to be defined for the optimal dimensioning of the BTMS design.

8.3.1 Comsol Settings

Evaluation of Fitness Function

The available Comsol pre-defined post-processing tools make it very easy to evaluate all the previously defined objectives from a solved Comsol model, by the creation of some *Data Sets* and/or *Derived Values*, under the *Results* node in the Comsol model tree. Besides, the definition of some surface or body selections and the so-called *Component Couplings* under the *Definitions* node (which can include volume or surface integrals and maximum or minimum body or surface values), also facilitate the evaluation process of the simulation considerably.

The available Comsol pre-defined post-processing graphs, tables and other tools make it very easy to evaluate the temperature and SOC homogeneity of the model, because the volume (or surface) maximum and minimum values of any solution can be easily evaluated at all the simulation time steps after the transient solution of the model has been computed. Hence, e.g., a table can be obtained after the simulation finishes, containing the following columns: simulation time, maximum and minimum temperature (from all the batteries within the module), and maximum and minimum SOC (from the 2D cell model). In the case of the energy efficiency and the weight, and similarly to what was explained above related to the Comsol export features, the COP and the weight values can be obtained for every time step and exported as a table or graph.

Settings for Batch Execution

In the previous section, the procedure to create the tables or data sets containing the main terms that permit to evaluate quantitatively the objective function of the BTMS design has been explained. Afterwards, when a parametric geometrical model has been implemented in Comsol and such export data sets have been incorporated, an optimization algorithm can recursively run through the Comsol model to automatically optimize the parameters that the model relies on.

With regard to this process, it is sought to link an external optimizer (which could be coded in Matlab, Python, or any other adequate programing language) to the multiphysics model that is solved in Comsol. With this objective, two requirements are set:

i. On one hand, the simulation job must be launched from an external program in batch mode, and its execution call has to be susceptible to model parameter modifications.

ii. On the other hand, the results of the simulation that are needed to quantitatively evaluate the objective function must be automatically exported after the simulation job has finished.

In order to meet those requirements, once a Comsol model has been generated from the general user interface (GUI), several steps have to be sequentially followed. The first steps have to be executed from the GUI:

1. A *Batch Node* has to be added in the model *Study* sequence, specifying the desired path and file name of the batch job model [1].

2. Then, the batch solution has to be executed from the GUI. When finished, the recently created batch model file should be automatically opened.

3. Once the simulation job has been completed and the batch model file containing the solution opens, the desired results to export (which comprise all the data sets that are needed for the evaluation of the optimization objective function, described in section 8.1.3), must be exported manually a first time. This can include the generation of the desired data set tables or any kind of figures or plots that can be generated and exported from the Comsol GUI.

Once this steps have been completed, the batch execution of the model is readily set and can be performed from the command line by the use of the command:

```
$ sh comsol batch -inputfile ModelFile.mph
```

However, it is not possible to enable or set for the automatic export of any defined data sets of a model run Comsol GUI. For that reason, it is necessary to access and modify the Comsol's *model object*.

The *model object* is a script file which makes use of a large number of Java methods, specifically defined for Comsol interpretation, that include methods for setting up a model creating geometries or meshes. Furthermore, it sets up the type of studies or solvers for any model. A basic understanding of Java programing language is required to fully appreciate how to work with the model object. In general, though, the *model object* is easily comprehensible, since the methods are structured in a tree-like way quite similar to the structure that is presented in the Comsol GUI Model Tree [147].

[1] This step, although it might seem unnecessary, is required to allow the admission of parameter inputs within the command line *batch* execution. In order to specify the batch process file name, we have to activate *Show-Advanced Study Options*.

After completing the three steps described above, and in order to access the *model object*, the final batch model (in which the export data sets have already been created) has to be saved with `.java` extension[2]. Then, the code that has been generated when the model results have been generated from the GUI (step 3) has to be localized in the Java code. E.g., the method that creates a table is:

```
model.result().table().create("tbl1", "Table");
```

Finally, when the desired output data sets have been localized and identified, a code line that contains a method for the automatic export of the data has to be manually added. E.g., for the table `"tbl1"`:

```
model.result().export("tbl1").run()
```

Once this last step has been completed, the external batch execution of the modified `.java` file can be performed after compiling the Java code by

```
$ sh comsol compile ModelFile.java -jdkroot /path-to-jdk-compiler
```

The compiled file (with extension `.class`) run can be started by the command

```
$ sh comsol batch -inputfile ModelFile.class
```

where, from the different flags that can be added. Most important for the work are the flags `-pname ParamNames` and `-pvalue ParamValues`, with which the parameters `ParamNames` that are defined within the Comsol *Parameters* node can be set to the values `ParamValues` for the present batch execution of the model.

Other flags can be added, such as `-batchlog LogFile.log`[3], which is interesting for tracking the batch execution of the Comsol model, or the tag `-outputfile`, that serves to specify a name to store the executed model once the batch simulation solution has been completed. Other interesting flags are `-nn` and `-np`, with which the number of computational nodes and processors can be specified, in case, i.e., the numerical simulation is launched to a cluster or a High Performance Computer (HPC). For the sake of completion, all the flags that are available can be seen by typing:

```
$ sh comsol -h
```

[2]It is highly recommended to, before saving in `.java` extension, execute *File-Compact History*, which will sort and compact the Java code of the *model object*

[3]This will create a text file with the information of the batch running process, and any error that might arise would be reported in this logging file.

This work aimed to cover all the information regarding the manipulation of the Java-based Comsol *model object*. However, all the information can be found in the reference guide [148].

8.3.2 Optimization Algorithm

Once the settings for the batch parametric execution and for the automatic results export of the Comsol simulations are set (blue dialog boxes in Figure 8.16), the numerical PDE model implemented in Comsol can be integrated to any external optimization algorithm (green dialog boxes, Figure 8.16) for the optimization of the design parameters.

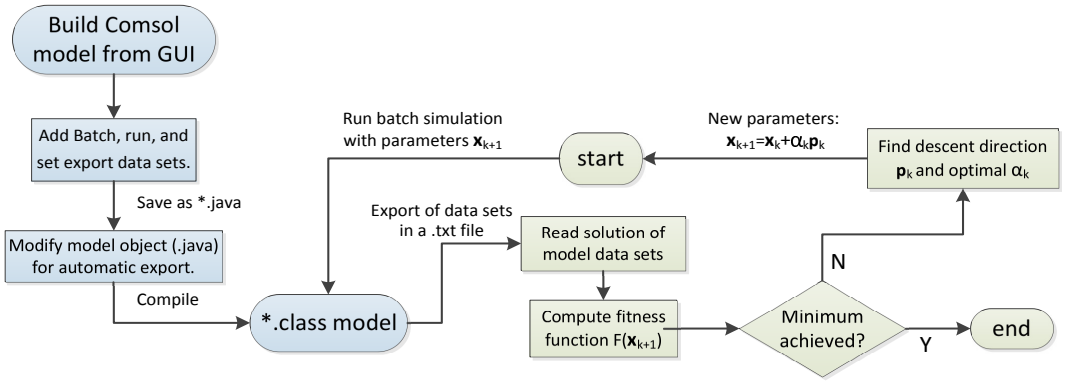

Figure 8.16: *Scheme of procedure for linking an external optimizer to a Comsol model.*

In the present work, the optimization algorithm, described in the next section, has been decided to be implemented in Python, because of its versatility, high-level language, and its high execution speed.

Scalarized Problem

As there usually exist multiple Pareto optimal solutions in multi-objective optimization problems, such as the one that is faced in this work, a solution for such problems is definitely not straightforward. In order to reduce the complexity of the optimization procedure, several methods convert the original problem with multiple objectives into the so-called *scalarized problem*, which is then a single-objective optimization problem.

As a first approach to test the optimization framework created in this work, which links Comsol models to any external optimization algorithm (see following section 8.3.1), a simple optimization routine is desired to be tested. For that reason,

and given the multiple objectives and load cases that are desired to be included, it has been decided to convert the multi-objective optimization problem into a single objective fitness by the use of the Weighted Sum Method (WSM).

This method is the simplest approach and probably the most widely used classical method for multi-objective problems [142], and consists of adding the set of objectives up into a single objective, by multiplying, or weighting, each objective with a user supplied weight.

Through this method, the multi-objective optimization problem, which is generally posed as

$$\underset{\mathbf{x}\in\mathbb{R}^n}{\text{minimize}} \quad F(\mathbf{x}) = [F_1(\mathbf{x}), \ldots, F_m(\mathbf{x})] \tag{8.10}$$

is simplified to

$$\underset{\mathbf{x}\in\mathbb{R}^n}{\text{minimize}} \quad Q(\mathbf{x}) = \sum_{k=1}^{m} w_k F_k^0(\mathbf{x}) \tag{8.11}$$

where the weights w_k, corresponding to the different objective functions, satisfy the following conditions,

$$\sum_{k=1}^{m} w_k = 1; \quad w_k \geq 0, \text{for } k = 1, \ldots, m. \tag{8.12}$$

and $F_k^0(\mathbf{x})$ being the normalized objective functions. Obviously, the original objective functions $F_1(\mathbf{x}), \ldots, F_m(\mathbf{x})$ might be represented in different scales and measure units. E.g., corresponding to the objectives defined above, the temperature is given in [K] and the SOC in %. Therefore, the normalization of the objective functions is required, by

$$F_k^0(\mathbf{x}) = \frac{F_k(\mathbf{x})}{S_k} \tag{8.13}$$

Theorem 8.3.1 *if* $\mathbf{x}^*$ *is a Pareto-optimal solution of a convex multi-objective optimization problem (8.10), then there exists a non-zero positive weight vector* $\mathbf{w}$ *s.t.* $\mathbf{x}^*$ *is a solution of problem (8.11)*

As suggested by theorem 8.3.1, any of the solutions pertaining to the optimal Pareto front solution of problem 8.10 can be found using the adopted weighted sum method [143]. However, it is clear that the optimum which can be found from problem 8.11 is dependent on the selected weight coefficients, w_k.

Gradient Descent Algorithm

Since we have a quite big number of design parameters (at the moment there are between 10 and 20 parameters, but with the projection of incorporating more parameters to the analysis) and the objective function computation is quite expensive in terms of computational time (solution of the transient FEM simulation in Comsol), a *stochastic* optimization approach, such as the evolutionary approach presented in [144], might be prohibitive for this concrete case. Instead, and since the design parameters that have to be optimized pertain to continuous geometrical values and not to a discrete series of values, a gradient-based algorithm might be the most appropriate strategy.

As a preliminary development of this BTMS design tool, a simple and classical gradient descent optimization approach has been implemented in Python. The implemented algorithm, starting from an initial parameter point, $\mathbf{x_0}$, search first for a descent direction, $\mathbf{p}_k$, along which the objective function $F(\mathbf{x})$ gets reduced near $\mathbf{x_0}$. Then, a *line search* approach is adopted to determine the step size, α_k, that determines how far $\mathbf{x}$ should move along the given descent direction [145]. The iterative procedure to update the parameter vector $\mathbf{x}$ can, hence, be written as

$$\mathbf{x}^{k+1} = \mathbf{x}^k + \alpha^k \mathbf{p}^k \tag{8.14}$$

where the superscript k refers to the iteration number.

Since the objective function depends, in this case, on the transient solution of a complex PDE system, implemented in Comsol, the descent directions cannot be computed explicitly. Instead, $\mathbf{p}_k$ is approximated by a finite differences approach of the jacobian of the objective function, $\mathbf{J}_F(\mathbf{x}_k) = (\partial F/\partial x_1, \ldots, \partial F/\partial x_m)$.

Once the descent direction has been found, the Armijo rule condition is used as an inexact line search stipulation. The inequality that determine, thus, the step size of each iteration to ensure that the objective function $F(\mathbf{x})$ decreases "sufficiently" is written as:

$$F(\mathbf{x} + \alpha^k \mathbf{p}^k) \leq F(\mathbf{x}) + \xi \alpha^k (\mathbf{p}^k)^T \cdot \mathbf{p}^k \tag{8.15}$$

where the free parameters $0 \leq \xi \leq 1$ are fixed to a small value (e.g., $\xi_1 = 10^{-3}$). Whenever this condition is not fulfilled, the stepping parameter α gets reduced by a given ratio (which is also manually tuned).

The implemented algorithm has been tested with a very simple linear regression given 20 random points. The results (Figures 8.17 and 8.18) show that the algorithm behaves as expected and converges very fast. Besides, it can be observed that the

Armijo condition forces the decrease of the parameter α at the iteration $k = 10$

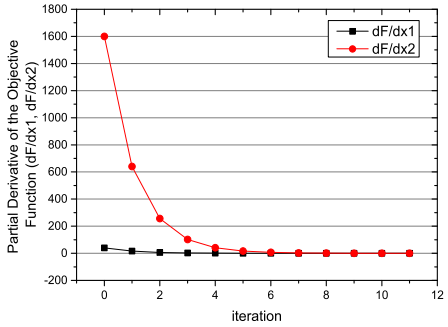

Figure 8.17: *Evolution of the finite differences approximation of the objective function partial derivatives with respect to the parameters x_1 and x_2.*

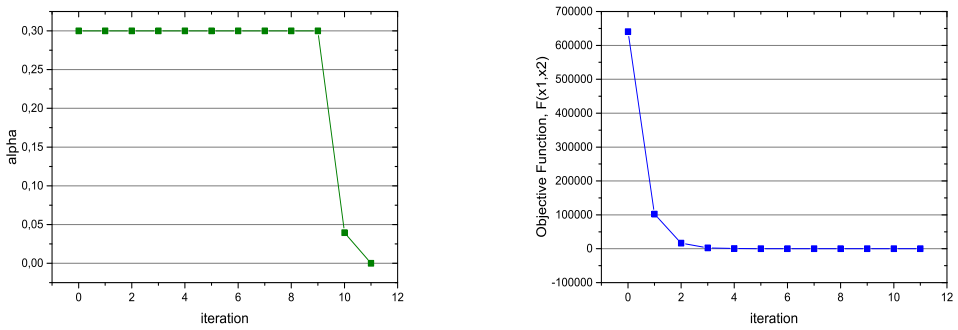

Figure 8.18: *Evolution of the stepping parameter, α, and of the objective function, $F(x_1, x_2)$.*

However, the tested example is clearly a convex function and is much simpler than the objective function from the BTMS design.

Current Work Status

The optimization framework settings that have been described in the previous sections work at present without any problem, including the recursive external batch execution and automatic data export of the simulation model. However, unfortunately, no proper results for the optimization algorithm are available yet due to different problem sources that keep arising to this end. For that reason, this task is kept as an open problem in this thesis, and is set as the first priority for the author's future work.

Nevertheless, several possible sources have already been investigated and solved. For example, a number of run trials have been launched with no success by tuning the arbitrary parameters of the algorithm, such as ξ, the initial parameters $\mathbf{x}^0$, or the stepping value α^0. Conversely, one of the main problems that have been detected was related to the meshing algorithm in Comsol, which was unable to generate the mesh when the model was called with some parameter variations. Once this has been solved by fixing thinner intervals for each parameter space, other problems persist.

Actually, the main problem source is believed to be either the optimization algorithm itself (or its implementation in Python) or the bad definition of the objective function $F(\mathbf{x})$. In any case, this error is visible because in some of the run trials the algorithm got stuck in a local minimum very near to the initial configuration, and known not to be the optimal because of the data set that is already available from the parametric sweep data.

Thus, the future development will focus on, and sequentially:

1. The validation of the implemented gradient descent algorithm and a precise exploration of the objective function concavity, within a moderate parametric space region, by the execution of several parametric sweep simulations.

2. In case it is necessary, afterwards, the implementation of more adequate optimization algorithms will be investigated (such as the ϵ-constraint method [143] or the multi-objective).

Chapter 9

Conclusions and Future Work

In this thesis, an empirically-based numerical model for the electrochemical-thermal behavior of a pouch lithium-ion battery has been implemented with the purpose of studying the design of the battery thermal management system (BTMS) for an electric vehicle.

After studying the physical phenomena that are related to lithium-ion thermal issues and after reviewing the modeling strategies that appear in the literature, the implemented model strategy has been selected based on the concrete purposes of this work. As a result, the final model implemented in finite elements method (FEM) couples a simple equivalent-circuit representation for the electrochemical phenomena, in a 2D spatially-distributed fashion, with a 3D thermal model of the pouch battery with lumped material properties.

The focus for the thermal study has been set to the fast charge process that is required to fully-charge the battery pack in one hour since, after analysing a driving profile, is considered as the most demanding load case. Based on the study objectives and the available media, the tests for characterizing the relevant electrical performance of the battery have been designed and conducted. This included the characterization of the open-circuit voltage of the battery, where a new fitting procedure has been suggested due to hysteresis, as well as the obtaining of the battery overpotential under different galvanostatic regimes and operating conditions.

Executing the electrical tests, reversible reaction thermal effects have been observed to be considerable in the thermal behavior of the battery sample, and determine the S-shaped temperature evolution of the battery, especially at low current rates. The internal resistance associated to the battery overpotential decreases with increasing current rates and operating temperatures, and shows diffusion limitations both for full charge and discharge processes.

Aside, and as a validation strategy for the developed numerical model, calorimetry measurements have also been carried out to characterize the heat generation rate in a discrete number of SOC intervals. Other inputs for the model have also been adopted from this testing tool, namely the heat capacity of the battery sample and the entropic coefficient. The obtained heat capacity results are in good agreement with the data presented in the literature. The estimation of the entropic coefficient is obtained by a common analysis methodology from the calorimetric data, and promisingly shows good agreement with the precise potentiometric measurements (which are much more time costly).

The results of the model show good accordance with the averaged heat generation rates measured in the calorimeter. However, the validation of the transient temperature evolution has been found to be more complex than expected, as it depends on the operating temperature and the external conditions, including thermal convection and conduction, which are unknown for both, the climate chambers and for the calorimeter chamber experiments.

Besides, the present model allows for the consideration of the ohmic heat dissipation, apart from the reaction heat generated in the cell active materials, which characterizes some of the specific phenomena of large size pouch batteries. The ohmic heat generation is observed to be dependent on the electrode's thickness. The amount of ohmic heat dissipation, which depends on the material parameters that are adopted from the literature, is observed to account for up to 15% of the total heat dissipation in a 1C constant current charge. A better approximation of the magnitude of this heat source would require further investigation, either directly, by the internal structure of the battery cells, or indirectly, by high quality thermal imaging.

From the model results, a battery cooling strategy is suggested for enhancing battery life and performance, consisting of the application of a reduced cooling power in the region of current collector tabs. By this strategy, the surface temperature of the battery and the cell's electrical imbalance get reduced, which would lead to a more uniform and slower degradation of the cell.

The implemented battery model still leaves room for improvement. One way to enhance it would be a better representation of the transient behavior of the battery, with the addition of a more complex equivalent-circuit formulation. Aside, a suggestion for the future development of such a model would be to add an aging model to the empirically-based electrochemical model. This would allow for the study of surface distributed degradation which, to the best of author's knowledge, has not been presented in the literature yet.

In the final part of the thesis, a novel BTMS design based on the combination of heat pipes and thermoelectric elements has been presented. Making use of the developed electrochemical-thermal battery model, a model for the battery sub-module pack has been implemented to assess the design of this BTMS, including simple models of the thermoelectric and the heat pipe elements. From the solution of this model, it can be seen that the temperature increase during fast charge (in the interval from 40% to 70% SOC) can be reduced by more than 50% by the application of a 180W cooling power to the thermoelectrics of each sub-module.

After defining a number of concrete objectives for an optimal design of the BTMS, the analysis of the results of the thermal model of the battery sub-module by the variation of some of the design parameters has brought to light the complexity of the optimal design process. The improvement of one of the objectives for battery life enhancement due to a parameter variation, (i.e., the reduction of the maximum temperature) often turns into the deterioration of another battery "health" indicator (i.e., the temperature homogeneity).

For that reason, a framework for the automatic optimization of the BTMS model has been designed and developed. Once the framework has been set, the recursive batch execution of the thermal model from the command line is allowed, which permits the usage of any optimization algorithm, from any external software, for the solution of the optimal BTMS design problem.

Finally, a scalarized formulation of the original multi-objectives optimization problem is presented, and has been attempted to be solved by a simple gradient descent algorithm, implemented in Python. Until today, the execution of the optimization has not been successfully achieved. The main problem sources have been identified as: the complexity of the meshing process, the lack of availability of memory and computational sources, and the inabilty of the proposed algorithm to tread such a non-convex problem. This task, thus, and because of time constraints, is left as an open problem. However, and still having a lot of place for improvement, the development of the optimizer architecture can be useful for many other applications in the future.

As a final conclusion, the implemented model has shown, overall, good appropriateness for the purposes of this work since it maintains a still affordable computational cost but at the same time permits to reflect or study some peculiarities of the pouch cells in a better way than from a 0D or 1D system perspective.

Bibliography

[1] International Energy Agency (IEA), Online source, *Global EV Outlook 2016,* https://www.iea.org/publications/freepublications/publication/Global_EV_Outlook_2016.pdf (accessed November 2016).

[2] S. Li, L. Tong, J. Xing, Y. Zhou, *The Market for Electric Vehicles: Indirect Network Effects and Policy Design,* http://dx.doi.org/10.2139/ssrn.2515037 (accessed September 2016).

[3] Energy Storage Upddate, online source, *Lithium-ion costs to fall by up to 50% within five years* http://analysis.energystorageupdate.com/lithium-ion-costs-fall-50-within-five-years (accessed May 2016).

[4] Online source, *Modified Daihatsu Mira EV Breaking Record With 627 Miles on a Single Battery Charge,* https://www.greenoptimistic.com/daihatsu-mira-ev-1000-km-20100525/#.WIqhR1PhDIU (accessed December 2016).

[5] Avicenne Energy, online source *Battery Market Development for Consumer Electronics, Automotive, and Industrial: Materials Requirements and Trends,* http://www.avem.fr/docs/pdf/AvicenneDiapoXining.pdf (accessed June 2016).

[6] S.C. Chen, C.C. Wan, Y.Y. Wang *Thermal Analysis of Lithium-Ion Batteries,* J. Power Sources, 140 (2005) 111-124.

[7] R. Zhao, S. Zhang, J. Liu, J. Gu, *A Review of Thermal Performance Improving Methods of Lithium-Ion Battery: Electrode Modification and Thermal Management System,* J. Power Sources, 299 (2015) 557-577.

[8] S.R. Alavi-Soltani, T.S. Raviguruajan, M. Rezac, *Thermal Issues in Lithium-Ion Batteries,* Proceedings of IMECE, American Society of Mechanical Engineers, (2006) 383-393.

[9] O. Egbue, S. Long, *Barriers to Widespread Adoption of Electric Vehicles: An Analysis of Consumer Attitudes and Perceptions,* Energy Policy, 48 (2012) 717-729.

[10] Online source, *The Surprising Culprit behind a recent Chevrolet Volt Fire,* http://www.torquenews.com/2250/surprising-culprit-behind-recent-chevrolet-volt-fire (accessed April 2016).

[11] Online source, *BYD e6 Electric Taxi Burns After 112-MPH Drunk Supercar Driver Crash,* http://www.greencarreports.com/news/1076517 _byd-e6-electric-taxi-burns-after-112-mph- drunk-supercar-driver-crash (accessed January 2017).

[12] H. Yang, S. Amiruddin, H.J. Bang, Y.K. Sun, J. Prakash, *A Review of Li-Ion Cell Chemistries and their Potential use in Hybrid Electric Vehicles,* J. of Industrial and Engineering Chemistry, 12 (2006) 12-38.

[13] D.P. Finegan, M. Scheel, J.B. Robinson, B. Tjaden, M. Di Michiel, G. Hinds, D.J.L. Brett, P.R. Shearing, *Investigating Lithium-Ion Battery Materials During Overcharge-Induced Thermal Runaway: an Operando and Multi-Scale X-Ray CT Study,* Royal Society of Chemistry, Phys. Chem. Chem. Phys., (2016) Advance Article DOI: 10.1039/c6cp04251a

[14] S. Al Hallaj, H. Maleki, J.S. Hong, J.R. Selman, *Thermal Modeling and Design Considerations of Lithium-Ion Batteries,* J. Power Sources, 83 (1999) 1-8.

[15] G.H. Kim, A. Pesaran, R. Spotnitz, *A Three-Dimensional Thermal Abuse Model for Lithium-ion Cells,* J. Power Sources, 170 (2007) 476-489.

[16] P.G. Balakrishnan, R. Ramesh, T.P. Kumar, *Safety Mechanisms in Lithium-Ion Batteries,* J. Power Sources, 155 (2006) 401-414.

[17] K. Yu, X. Yang, Y. Cheng, C. Li, *Thermal analysis and two-directional air flow thermal management for lithium-ion battery pack* J. Power Sources, 270 (2014) 193-200.

[18] L. Fan, J.M. Khodadadi, A.A. Pesaran, *A Parametric Study on Thermal Management of an Air-Cooled Lithium-Ion Battery Module for Plug-in Hybrid Electric Vehicles,* J. Power Sources, 238 (2013) 301-312.

[19] Y.S. Choi, D.M. Kang, *Prediction of Thermal Behaviors of an Air-Cooled Lithium-Ion Battery System for Hybrid Electric Vehicles,* J. Power Sources, 270 (2014) 273-280.

[20] H. Sun, R. Dixon, *Development of a Liquid Cooled Battery Module,* J. Electrochem. Soc., 163 (2016) E313-E321.

[21] J. Xun, R. Liu, K. Jiao, *Numerical and Analytical Modeling of Lithium Ion Battery Thermal Behaviors with Different Cooling Designs,* J. Power Sources, 233 (2013) 47-61.

[22] T.H. Tran, S. Harmand, B. Sahut, *Experimental Investigation on Heat Pipe Cooling for Hybrid Electric Vehicle and Electric Vehicle Lithium-Ion Battery,* J. Power Sources, 265 (2014) 262-272.

[23] Y. Dutil, D.R. Rousse, N.B. Salah, S. Lassue, L. Zalewski, *A Review on Phase-Change Materials: Mathematical Modeling and Simulations,* Renewable and Sustainable Energy Reviews, 15 (2011) 112-130.

[24] M.S. Wu, K.H. Liu, Y.Y. Wang, C.C. Wan, *Heat Dissipation Design for Lithium-Ion Batteries,* J. Power Sources, 109 (2002) 160-166.

[25] Q. Wang, B. Jiang, Q.F. Xue, H.L. Sun, B. Li, H.M. Zou, Y.Y Yan, *Experimental Investigation of EV Battery Cooling and Heating by Heat Pipes,* Applied Therm. Eng., 88 (2015) 54-60.

[26] S.A. Khateeb, S. Amiruddin, M. Farid, J.R. Selman, S. Al-Hallaj, *Thermal Management of Li-ion Battery with Phase Change Material for Electric Scooters: Experimental Validation,* J. Power Sources, 142 (2005) 345-353.

[27] T.M. Bandhauer, S. Garimella, T.F. Fuller, *A Critical Review of Thermal Issues in Lithium-Ion Batteries,* J. Electrochem. Soc., 158 (2011) R1-R25.

[28] M. Yazdanpour, *Electro-Thermal Modeling of Lithium-Ion Batteries,* Master Thesis, Iran University of Science and Technology (2011).

[29] U.S. Kim, C.B. Shin, C.S. Kim, *Effect of Electrode Configuration on the Thermal Behavior of a Lithium-Ion Battery,* J. Power Sources, 180 (2008) 909-916.

[30] P. Taheri, A. Mansouri, B. Schweitzer, M. Yazdanpour, M. Bahrami, *Electrical Constriction Resistance in Current Collectors of Large-Scale Lithium-Ion Batteries,* J. Electrochem. Soc., 160 (2013) A1731-A1740.

[31] P. Arora, R.E. White, M. Doyle, *Capacity Fade Mechanisms and Side Reactions in Lithium-Ion Batteries,* J. Electrochem. Soc., 145 (1998) 3647-3667.

[32] K. Jalkanen, J. Karppinen, L. Skogström, T. Laurila, M. Nisula, K. Vuorilehto, *Cycle Aging of Commercial NMC/Graphite Pouch Cells at Different Temperatures,* Applied Energy, 154 (2015) 160-172.

[33] S. Paul, C. Diegelmann, H. Kabza, W. Tillmetz, *Analysis of Ageing Inhomogeneities in Lithium-Ion Battery Systems,* J. Power Sources, 239 (2013) 642-650.

[34] J. Schmitt, *Modeling of Aging Effects and Extended Kalman Filter Based State of Charge Estimation of Lithium-Ion Batteries,* Master Thesis, Albert-Ludwigs-Universitat (2016).

[35] J. Vetter, P. Novák, M. Wagner, C. Veit, K.C. Möller, J. Besenhard, M. Winter, M. Wohlfahrt-Mehrens, C. Vogler, and A. Hammouche, *Ageing Mechanisms in Lithium-Ion Batteries,* J. Power Sources, 147 (2005) 269-281.

[36] V. Ramadesigan, P.W.C. Northrop, S. De, S. Santhanagopalan, R.D. Braatz, V.R. Subramanian, *Modeling and Simulation of Lithium-Ion Batteries from a Systems Engineering Perspective,* J. Electrochem. Soc., 159 (2012) R31-R45.

[37] A. Barré, B. Deguilhem, S. Grolleau, M. Gérard, F. Suard, D. Riu, *A Review on Lithium-Ion Battery Ageing Mechanisms and Estimations for Automotive Applications,* J. Power Sources, 241 (2013) 680-689.

[38] A. Pesaran, S. Santhanagopalan, G.H. Kim, *Addressing the Impact of Temperature Extremes of Large Format Li-Ion Batteries for Vehicle Applications,* NREL/PR-5400-58145, 30th International Battery Seminar (2013).

[39] Z. Rao, S. Wang, *A Review of Power Battery Thermal Energy Management,* Renewable and Sustainable Energy Reviews, 15 (2011) 4554-4571.

[40] S.S. Zhang, K. Xu, T.R. Jow, *The Low Temperature Performance of Li-ion Batteries,* J. Power Sources, 115 (2003) 137-140.

[41] G. Nagasubramanian, *Electrical Characteristics of 18650 Li-ion Cells at Low Temperatures,* J. Applied Electrochemistry, 31 (2001) 99-104.

[42] D. Andre, M. Meiler, K. Steiner, Ch. Wimmer, T. Soczka-Guth, D.U. Sauer, *Characterization of High-Power Lithium-Ion Batteries by Electrochemical Impedance Spectroscopy. I. Experimental Investigation,* J. Power Sources, 196 (2011) 5334-5341.

[43] A.J. Bard, L.R. Faulkner, *Electrochemical Methods: Fundamentals and Applications* John Wiley & Sons, Inc., London (2001)

[44] M.C. Smart, B.V. Ratnakumar, S. Surampudi *Electrolytes for LowTemperature Lithium Batteries Based on Ternary Mixtures of Aliphatic Carbonates,* J. Electrochem. Soc., 146 (1999) 486-492.

[45] B.V. Ratnakumar, M.C. Smart, S. Surampudi, *Effects of SEI on the Kinetics of Lithium Intercalation,* J. Power Sources, 9798 (2001) 137-139.

[46] C. Daniel, J.O. Besenhard, *Handbook of Battery Materials, Second Edition* Wiley-VCH Verlag GmbH & Co., KGaA (2008)

[47] E. Peled, *The Electrochemical Behavior of Alkali and Alkain Earth Metals in Non-Aqueous Battery Systems - the Solid Electrolyte Interphase Model,* J. Electrochem. Soc., 126 (1979) 2047-2051.

[48] C.K. Huang, J.S. Sakamoto, J. Wolfenstine, S. Surampudi, *The Limits of LowTemperature Performance of LiIon Cells,* J. Electrochem. Soc., 147 (2000) 2893-2896.

[49] M. Winter, J. O. Besenhard, M. E. Spahr, and P. Novák, *Insertion Electrode Materials for Rechargeable Lithium Batteries,* Adbanced Materials, 10 (1998) 725-763.

[50] J. Fan, S. Tan, *Studies on Charging Lithium-Ion Cells at Low Temperatures,* J. Electrochem. Soc., 153 (2006) A1081-A1092.

[51] T. Waldmann, G. Bisle, B.I. Hogg, S. Stumpp, M.A. Danzer, M. Kasper, P. Axmann, M. Wohlfahrt-Mehrens, *Influence of Cell Design on Temperatures and Temperature Gradients in Lithium-Ion Cells: An In Operando Study* J. Electrochem. Soc., 162 (2015) A921-A927.

[52] Y. Ji, Y. Zhang, C.Y. Wang, *Li-Ion Cell Operation at Low Temperatures,* J. Electrochem. Soc., 160 (2013) A636-A649.

[53] T.A. Stuart, A. Hande, *HEV Battery Heating using AC Currents,* J. Power Sources, 129 (2004) 368-378.

[54] P. Ramadass, B. Haran, R. White, B.N. Popov, *Capacity Fade of Sony 18650 Cells Cycled at Elevated Temperatures: Part I. Cycling Performance.* J. Power Sources, 112 (2002) 606-613.

[55] Axeon (Company), Online resource, *Our Guide To Batteries,* http://www.jmbatterysystems.com/JMBS/media/JMBS/Technology/ Axeon-Guide-to-Batteries-2nd-edition.pdf (accessed July 2016)

[56] Visual Science (Company), Online source, *Lithium Ion Batteries, $LiFePO_4$,* http://visual-science.com/projects/rusnano/lithium-ion-batteries/ (accessed August 2016)

[57] P. Ramadass, B. Haran, R. White, B.N. Popov, *Capacity Fade of Sony 18650 Cells Cycled at Elevated Temperatures: Part II. Capacity Fade Analysis.* J. Power Sources, 112 (2002) 614-620.

[58] G.M. Ehrlich, *Handbook of Batteries,* McGraw-Hill, New York, 3rd Edition (2002).

[59] S.S. Choi, H.S. Lim *Factors that Affect Cycle-Life and Possible Degradation Mechanisms of a Li-ion Cell Based on LiCoO2,* J. Power Sources, 111 (2002) 130-136.

[60] J.R. Belt, C.D. Ho, Chester G. Motloch, T.J. Miller, Tien Q. Duong, *A Capacity and Power Fade Study of Li-ion Cells During Life Cycle Testing,* J. Power Sources, 123 (2003) 241-246.

[61] L. Bodenes, R. Naturel, H. Martinez, R. Dedryvère, M. Menetrier, L. Coguennec, J.P.Perès, C. Tessier, F. Fischer, *Lithium Secondary Batteries Working at Very High Temperature: Capacity Fade and Understanding of Aging Mechanisms,* J. Power Sources, 236 (2013) 265-275.

[62] F. Leng, C.M. Tan, M. Pecht, *Effect of Temperature on the Aging rate of Li-Ion Battery Operating above Room Temperature,* Scientific Reports, Nature, 10.1038/srep12967 (2015)

[63] K. Amine, J. Liu, I. Belharouak, *High-Temperature Storage and Cycling of C-$LiFePO_4$/Graphite Li-ion Cells,* Electrochemistry Communications, 7 (2005) 669-673.

[64] X. Hu, *Battery Thermal Management in Electric Vehicles,* ANSYS Inc., White Paper (2011).

[65] R. Spotnitz, J. Franklin, *Abuse Behavior of High-Power, Lithium-Ion Cells,* J. Power Sources, 113 (2003) 81-100.

[66] E.V. Thomas, H.L. Case, D.H. Doughty, R.G. Jungst, G. Nagasubramanian, E.P. Roth, *Accelerated Power Degradation of Li-Ion Cells,* J. Power Sources, 124 (2003) 254-260.

[67] M.C. Smart, B.V. Ratnakumar, J. Whitacre, L. Whitcanack, K. Chin, M. Rodriguez, S. Surampudi, *The Effect of High Temperature Exposure upon the Performance of Lithium Ion Cells,* Battery Conf. on Applications and Advances, (2002) 53-58.

[68] B.T. Kuhn, G.E. Pitel, P.T. Krein, *Electrical Properties and Equalization of Lithium-Ion Cells in Automotive Applications,* IEE Conference, Vehicle Power and Propulsion (2005) 55-59.

[69] K.E. Thomas, J. Newmann, *Heats of Mixing and of Entropy in Porous Insertion Electrodes,* J. Power Sources, 119-121 (2003) 844-849.

[70] Y.F. Reynier, R.Yazami, B. Fultz, *Thermodynamics of Lithium Intercalation into Graphites and Disordered Carbons,* J. Electrochem. Soc., 151 (2004) A422-A426.

[71] S.J. Bazinski, X. Wang, *The Influence of Cell Temperature on the Entropic Coefficient of a Lithium Iron Phosphate (LFP) Pouch Cell,* J. Electrochem. Soc., 161 (2014) A168-A175.

[72] International Energy Agency, Online source, *Global EV Outlook 2016,* https://www.iea.org/publications/freepublications/publication/Global_EV_Outlook_2016.pdf (accessed on September 2016).

[73] A. Barai, W.D. Widanage, J. Marco, A. McGordon, P. Jennings, *A Study of the Open Circuit Voltage Characterization Technique and Hysteresis Assessment of Lithium-Ion Cells,* J. Power Sources, 295 (2015) 99-107.

[74] J. Schmalstieg, S. Kbitz, M. Ecker, D.U. Sauer, *A Holistic Aging Model for Li(NiMnCo)O_2 Based 18650 Lithium-Ion Batteries,* J. Power Sources, 257 (2014) 325-334.

[75] Y.S. Lee, M.W. Cheng, *Intelligent control battery equalization for series connected lithium-ion battery strings,* IEEE Trans. Ind. Electron., 52 (2005) 12971307.

[76] M. Chen and G. A. Rincn-Mora, *Accurate electrical battery model capable of predicting runtime and IV performance,* IEEE Trans. Energy Conversion, 21 (2006) 504511.

[77] B.T. Kuhn, G.E. Pitel, P.T. Krein, *Electrical Properties and Equalization of Lithium-Ion Cells in Automotive Applications,* Vehicle Power and Propulsion, VPCC (2005) IEEE conference.

[78] J. Dambrowski, *Review on Methods of State-of-Charge Estimation with Viewpoint to the Modern $LiFePO_4/Li_4Ti_5O_{12}$ Lithium-Ion Systems,* Int. Telecom. Energy Conference, Intelec (2013).

[79] N.A. Chaturvedi, R. Klein, J. Christensen, J. Ahmed, A. Kojic, *Algorithms for Advanced Battery-Management Systems: Modeling, Estimation, and Control Challenges for Lithium-Ion Batteries,* IEEE Control Syst. Mag., 30 (2010) 49-68.

[80] J. R. MacDonald, *Impedance Spectroscopy: Emphasizing Solid Materials and Systems,* Wiley, New York (1987).

[81] H.G. Shweiger, O. Obeidi, O. Komesker, A. Raschke, M. Schiemann, C. Zehner, M. Gehnen, M. Keller, P. Birke, *Comparison of Several Methods for Determining the Internal Resistance of Lithium Ion Cells,* Sensors, 10 (2010) 5604-5625.

[82] P. Ramadass, B. Haran, R. White, B.N. Popov, *Mathematical Modeling of the Capacity Fade of Li-ion Cells,* J. Power Sources, 123 (2003) 230-240.

[83] G. Vertiz, M. Oyarbide, H. Macicior, O. Miguel, I. Cantero, P. Fernandez de Arroiabe, I. Ulacia, *Thermal Characterization of Large Size Lithium-ion Pouch Cell Based on 1D Electro-Thermal Model,* J. Power Sources, 272 (2014) 476-484.

[84] C.M. Doyle, *Design and Simulation of Lithium Rechargeable Batteries,* Ph.D. Thesis, Lawrence Berkeley Laboratory, University of California (1995).

[85] L. Rao, J. Newmann, *Heat-Generation Rate and General Energy Balance for Insertion Battery Systems,* J. Electrochem. Soc., 144 (1997) 2697-2704.

[86] D. Bernardi, E. Pawlikowski, J. Newman, *A General Energy Balance for Battery Systems,* Meeting of the Society, Vol. 132, University of California - Berkeley (1985).

[87] C. Edouard, M. Petit, C. Forgez, J. Bernard, R. Revel, *Parameter Sensitivity Analysis of a Simplified Electrochemical and Thermal Model for Li-ion Batteries Aging,* J. Power Sources, 325 (2016) 482-494.

[88] A. Greco, X. Jiang, *A Coupled Thermal and Electrochemical Study of Lithium-ion Battery Cooled by Paraffin/Porous-Graphite-Matrix Composite* J. Power Sources, 315 (2016) 127-139.

[89] Y. Lai, S. Du, L. Ai, L. Ai, Y. Cheng, Y. Tang, M. Jia, *Insight into Heat Generation of Lithium Ion Batteries Based on the Electrochemical-Thermal Model at High Discharge Rates,* Int. J. of Hydrogen Energy, 40 (2015) 13039-13049.

[90] L.H. Saw, Y. Ye, A.A.O. Tay, *Electrochemicalthermal Analysis of 18650 Lithium Iron Phosphate cell,* Energy Conversion and Management, 75 (2013) 162-174.

[91] C. Walchshofer, T. Hutzenlaub, S. Thiele, B. Kaludercic, R. Spotnitz, *Three-Dimensionally Resolved Simulations of a $LiCoO_2$ Electrode Structure Obtained via FIB/SEM,* www.cd-adapco.com/sites/default/files/technical_document/pdf/3D %20Microstructure%20Electrochemistry%20Model.pdf (accessed August 2016).

[92] M. Neumann, V. Schmidt, *Stochastic 3D Modeling of Amorphous Microstructures - A Powerful Tool for Virtual Materials Testing,* ECCOMAS Congress, VII European Congress on Computational Methods in Applied Sciences and Engineering (2016).

[93] G.H. Kim, K. Smith, K.J Lee, S. Santhanagopalan, A. Pesaran, *Multi-Domain Modeling of Lithium-Ion Batteries Encompassing Multi-Physics in Varied Length Scales,* J. Electrochem. Soc. 158 (2011) A955-A969.

[94] K.J. Lee, K. Smith, A. Pesaran,G.H. Kim, *Three Dimensional Thermal-, Electrical-, and Electrochemical-Coupled Model for Cylindrical Wound Large Format Lithium-Ion Batteries,* J. Power Sources, 241 (2013) 20-32.

[95] Kostetzer L. *Efficient Lithium-Ion Battery Pack Electro-Thermal Simulation,* Sustainable Automotive Technologies 2013. Lecture Notes in Mobility. Springer (2014).

[96] S. Santhanagopalan, Q. Guo, P. Ramadass, R.E. White, *Review of Models for Predicting the Cycling Performance of Lithium-Ion Batteries,* J. Power Sources, 156 (2006) 620-628.

[97] M. Guo, G. Sikha, R.E. White, *Single-Particle Model for a Lithium-Ion Cell: Thermal Behavior,* J. Electrochem. Soc., 158 (2011) A122-A132.

[98] J. Newmann, *Optimization of Porosity and Thickness of a Battery Electrode by Means of a ReactionZone Model,* J. Electrochem. Soc., 142 (1995) 97-101.

[99] P.M. Gomadam, J.W. Weidner, R.A. Dougal, R.E. White, *Mathematical Modeling of Lithium-ion and Nickel Battery Systems,* J. Power Sources, 110 (2002) 267-284.

[100] Comsol (Company), Online source, *Batteries & Fuel Cells Module,* https://www.comsol.de/batteries-and-fuel-cells-module (accessed on March 2016).

[101] CD-Adapco (Company), Online source, *Thermal-Electrochemistry Simulations Improve on Overall Battery Performance, Safety and Life,* http://www.cd-adapco.com/industries/batteries (accessed on August 2016).

[102] K.A. Smith, C.D. Rahn, C.Y. Wang, *Control Oriented 1D Electrochemical Model of Lithium Ion Battery,* Energy Convers. and Management, 48 (2007) 2565-2578.

[103] V.R. Subramanian, V. Boovaragavan, V. Ramadesigan, M. Arabandi, *Mathematical Model Reformulation for Lithium-Ion Battery Simulations: Galvanostatic Boundary Conditions,* J. Electrochem. Soc., 156 (2009) A260-A271.

[104] S.K. Rahimian, S.C. Rayman, R.E. White, *Maximizing the Life of a Lithium-Ion Cell by Optimization of Charging Rates,* J. Electrochem. Soc., 157 (2010) A1302-A1308.

[105] S. Chacko, Y.M. Chung, *Thermal Modelling of Li-Ion Polymer Battery for Electric Vehicle Drive Cycles,* J. Power Sources, 213 (2012) 296-303.

[106] K. Uddin, A. Picarelli, *Phenomenological Li Ion Battery Modelling in Dymola,* Linköping University Electronic Press, http://www.ep.liu.se/ecp/096/034/ecp14096034.pdf (accessed March 2016).

[107] K. Chen, G. Unsworth, X. Li *Measurements of Heat Generation in Prismatic Li-Ion Batteries,* J. Power Sources, 261 (2014) 28-37.

[108] A. Latz, J. Zausch, *Multiscale Modeling of Lithium Ion Batteries: Thermal Aspects,* Beilstein J. Nanotechnol., 6 (2015) 9871007.

[109] K.H. Kwon, C.B. Shin, T.H. Kang, C.S. Kim, *A Two-Dimensional Modeling of a Lithium-polymer Battery,* J. Power Sources, 163 (2006) 151-157.

[110] J. Christensen, D. Cook, P. Albertus, *An Efficient Parallelizable 3D Thermoelectrochemical Model of a Li-Ion Cell,* J. Electrochem. Soc., 160 (2013) A2258-A2267.

[111] W. Gu, C.Y. Wang, *Thermal-Electrochemical Modeling of Battery Systems,* J. Electrochem. Soc., 147 (2000) 2910-2922.

[112] L. Ritter, *Requirements for Lithium-Ion Cells for Use in Electric Vehicles / "Anforderungen an Lithium-Ionen-Zellen fr den Einsatz in Elektrofahrzeugen",* Master Thesis, Hochschule Mannheim (2016).

[113] T. Huria, G. Ludovici, G. Lutzemberger, *State of Charge Estimation of High Power Lithium Iron Phosphate Cells,* J. Power Sources, 249 (2014) 92-102.

[114] V. Srinivasan, J.W. Weidner, J. Newman, *Hysteresis during Cycling of Nickel Hydroxide Active Material,* J. Electrochem. Soc., 148 (2001) A969-A980.

[115] M. Petzl, M.A. Danzer, *Nondestructive Detection, Characterization, and Quantification of Lithium Plating in Commercial Lithium-ion Batteries,* J. Power Sources, 254 (2014) 80-87.

[116] H. Bang, H. Yang, Y.K. Sun, J. Prakash, *In Situ Studies of $Li_xMn_2O_4$ and $Li_xAl_{0.17}O_{1.83}O_{3.97}S_{0.03}$ Cathode by IMC,* J. Electrochem. Soc., 152 (2005) A421-A428.

[117] W. Lu, I. Belharouak, D. Vissers, K. Amine, *In Situ Thermal Study of $Li_{1+x}[Ni_{1/3}Co_{1/3}Mn_{1/3}]_{1-x}O_2$ Using Isothermal Micro-clorimetric Techniques,* J. Electrochem. Soc., 153 (2006) A2147-A2151.

[118] M. Hukan, *High Precision Multi-Use Lithium-Ion Batteries Test-Bench for Measurement of Coulombic Efficiency and Entropic Coefficient,* Master Thesis, Technische Universität München (2016).

[119] S. Allu, S. Kalnaus, W. Elwasif, S. Simunovic, J.A. Turner, S. Pannala, *A New Open Computational Framework for Highly-Resolved Coupled Three-Dimensional Multiphysics Simulations of Li-ion Cells,* J. Power Sources, 246 (2014) 876-886.

[120] W.B. Gu, C.Y. Wang, *Thermal-Electrochemical Modeling of Battery Systems,* J. Electrochem. Soc., 147 (2000) 2910-2922.

[121] U.S. Kim, J. Yi, C.B. Shin, T. Han, S. Park, *Modelling the Thermal Behaviour of a Lithium-ion Battery During Charge,* J. Power Sources, 196 (2011) 5115-5121.

[122] J. Newman, W. Tiedemann, *Potential and Current Distribution in Electrochemical Cells: Interpretation of the HalfCell Voltage Measurements as a Function of ReferenceElectrode Location,* J. Electrochem. Soc., 140 (1993) 1961-1968.

[123] H. Gu, *Mathematical Analysis of a Zn/NiOOH Cell,* J. Electrochem. Soc., 130 (1983) 1459-1464.

[124] H. Culcu, B. Vebrugge, N. Omer, P. Van Den Bossche, J. Van Mierlo, *Internal Resistance of Cells of Lithium Battery Modules with FreedomCAR Model,* World Electric Vehicle Journal, Vol.3 (2009) 702-710.

[125] S.J. Bazinski, X. Wang, *Thermal Effect of Cooling the Cathode Grid Tabs of a Lithium-Ion Pouch Cell,* J. Electrochem. Soc., 161 (2014) A2168-A2174.

[126] K.F. Warnick, *Numerical Analysis for Electromagnetic Integral Equations,* Artech House, Norwood (2008) pp.69.

[127] Q. Cao, H.P. Zhang, G.J. Wang, Q. Xia, Y.P. Wu, , H.Q. Wu, *A Novel Carbon-Coated $LiCoO_2$ as Cathode Material for Lithium Ion Battery,* Electrochem. Communications, 9 (2007) 1228-1232.

[128] Y. Nishi, Sony Corporation, *Lithium-Ion Secondary Batteries; Past 10 Years and the Future,* J. Power Sources, 100 (2001) 101-106

[129] H. Wu, Q. Liu, S. Guo, *Composites of Graphene and $LiFePO_4$ as Cathode Materials for Lithium-Ion Battery: A Mini-review,* Nano-Micro Letters, 6 (2014) 316-326.

[130] F. Liu, F. Lan, J. Chen, *Dynamic Thermal Characteristics of Heat Pipe via Segmented Thermal Resistance Model for Electric Vehicle Battery Cooling,*

[131] G. Swanepoel, *Thermal Management of Hybrid Electrical Vehicles using Heat Pipes,* Master Thesis, University of Stellenbosch (2001).

[132] R. Zhao, J. Gu, J. Liu, *An Experimental Study of Heat Pipe Thermal Management System with Wet Cooling Method for Lithium Ion Batteries,* J. Power Sources, 273 (2015) 1089-1097.

[133] B. Saengchadr, N.V. Afzulpurkar, *A Novel Approach for Cooling Electronics Using a Combined Heat Pipe and Thermoelectric Module,* American J. of Eng. and Applied Sciences, 2 (2009) 603-610.

[134] M. Saleemi, M.S. Toprak, S. Li, M. Johnsson, M. Muhammed, *Synthesis, Processing, and Thermoelectric Properties of Bulk Nanostructured Bismuth Telluride (Bi_2Te_3),* J. Mater. Chem., 22 (2012) 725-730.

[135] H. Lee, *Thermal Design: Heat Sinks, Thermoelectrics, Heat Pipes, Compact Heat Exchangers, and Solar Cells,* John Wiley & Sons, Inc. (2011).

[136] C. Goupil, H. Ouerdane, K. Zabrocki, W. Seifert, N.F. Hinsche, and E. Muller, *Continuum Theory and Modelling of Thermoelectric Elements,* Wiley-VCH Verlag GmbH & Co, First Edition (2016).

[137] A.B. Solomon, M. Sekar, S.H. Yang, *Analytical Expression for Thermal Conductivity of Heat Pipe,* Applied Therm. Eng., 100 (2016) 462-467.

[138] E. Firat, G. Bandlamudi, P. Beckhaus, A. Heinzel, *Heat Pipe Assisted Thermal Management of a HT PEMFC Stack,* Excerpt of the Proceedings of the 2012 COMSOL Conference in Milan.

[139] C. Ferrandi, F. Iorizzo, M. Mameli, S. Zinna, M. Marengo, *Lumped Parameter Model of Sintered Heat Pipe: Transient Numerical Analysis and Validation,* Applied Thermal Engineering, 50 (2013) 1280-1290.

[140] M. Khalili, M.B. Shafii, *Experimental and Numerical Investigation of the Thermal Performance of a Novel Sintered-Wick Heat Pipe,* Applied Therm. Eng., 94 (2016) 59-75.

[141] Z.J. Zuo, A. Faghri, *A Network Thermodynamic Analysis of the Heat Pipe,* Int. J. Heat Mass Transfer, 41 (1998) 1473-1484.

[142] I.P. Stanimirović, M.L. Zlatanović, M.D. Petković, *On the Linear Weighted Sum Method for Multi-Objective Optimization,* Ser. Math. Inform., 26 (2011) 49-63.

[143] G. Narzisi, *Classic Methods for Multi-Objective Optimization,* http://cims.nyu.edu/ gn387/glp/lec2.pdf (accessed September 2016).

[144] C.L. Xiao, H.X. Huang, *Optimal Design of Heating System for Rapid Thermal Cycling Mold using Particle Swarm Optimization and Finite Element Method,* App. Therm. Eng., 64 (2014) 462-470.

[145] J. Snyman, *Practical Mathematical Optimization,* Springer (2005).

[146] S. Kulkarni-Thaker, Online source, *Line Search Methods,* http://www.cas.mcmaster.ca/∼cs4te3/notes/LineSearchMethods.pdf (accessed September 2016)

[147] Comsol (Company), software documentation, *Comsol Reference Guide (version 4.3a),* accessible at https://www.comsol.com (edition of 2012)

[148] Comsol (Company), software documentation, *Comsol API for use with Java, Reference Manual,* accessible at https://www.comsol.com, v 4.3b (edition of 2013)